Alpha clustering in the ground state of neutron rich light nuclei

by

Matthew Roland Barr

A thesis submitted to the
University of Birmingham
for the Degree of
Doctor of Philosophy

School of Physics & Astronomy
University of Birmingham
September 2013

UNIVERSITY OF
BIRMINGHAM

University of Birmingham Research Archive

e-theses repository

This unpublished thesis/dissertation is copyright of the author and/or third parties. The intellectual property rights of the author or third parties in respect of this work are as defined by The Copyright Designs and Patents Act 1988 or as modified by any successor legislation.

Any use made of information contained in this thesis/dissertation must be in accordance with that legislation and must be properly acknowledged. Further distribution or reproduction in any format is prohibited without the permission of the copyright holder.

Abstract

An experiment was conducted at the GSI Helmholtz Centre for Heavy Ion Research in Darmstadt, Germany, using the R^{3}B experimental setup. This included an array of double sided silicon strip detectors and a 4π array of NaI scintillator detectors surrounding the target, a bending magnet and downstream fragment detectors consisting of scintillating fibre detectors and a plastic scintillator time of flight wall. Cross sections have been measured for the breakup of $^{7,9-12}$Be and $^{8,10-15}$B on proton and ^{12}C targets at beam energies between 260 and 540 MeV per nucleon. These cross sections have been analysed with a focus on comparison to cluster model theory. In the context of a large collaboration and an experiment with diverse physics objectives, it is worth clarifying the author's contribution to the work presented. The author participated in running the experiment, calibrated the Silicon Strip Detectors and performed all the analysis discussed in this thesis.

Acknowledgements

In working towards my PhD, I have been helped by many people. For the most part they know who they are and what they have done to help me, but I would be remiss in not mentioning a few names in particular.

Firstly I am indebted to my supervisor Martin Freer, a man of awe-inspiring energy, for his tireless efforts in explaining and re-explaining everything to me. I must also thank the other members of the research group, especially Nick Ashwood and Neil Curtis, for sharing their great wisdom and experience.

Within R^{3}B, I owe thanks to the many people who have shared their calibrations and methods with the collaboration, but I must especially thank Jon Taylor for helping me get started with land02, Dominic Rossi for his extremely time-saving scripts, Matthias Holl and Valerii Panin for helping me get to grips with the SSD calibrations, and of course Ralf Plag for all his work developing the tracker then patiently helping me to misuse it.

Finally, thanks to the crowd from the office for a productive work environment and lunchtimes of intrigue & betrayal.

For my parents.

Contents

1 Introduction 1

1.1 Clustering 1

1.2 Experimental examples of Clustering 6

1.2.1 ^{16}O 6

1.2.2 ^{20}Ne 8

1.3 Neutron Rich Clustering 9

1.4 Experimental examples of Neutron Rich Clustering 12

1.4.1 ^{10}Be 12

1.4.2 ^{14}Be 14

2 Theory 16

2.1 Deformed Harmonic Oscillator (DHO) 16

2.2 Two Centre Harmonic Oscillator (TCHO) 20

2.3 Comparison of DHO and TCHO 23

2.4 Brink-Bloch Alpha Cluster Model (ACM) 24

2.5 Anti-symmetrised Molecular Dynamics (AMD) 27

2.6 Green's Function Monte Carlo (GFMC) 32

2.7 Inverse Kinematics 33

2.8 Quasi-Free Scattering (QFS) 34

2.9 Accessing the ground state - Wave-function Overlap 35

2.10 Accessing the ground state - QFS 36

3 Experimental Details 37

3.1 Beam Production 38

3.1.1 Ion Source 39

3.1.2 Universal Linear Accelerator (UNILAC) 39

3.1.3 Heavy Ion Synchrotron (SIS18) 40
3.1.4 Fragment Recoil Separator (FRS) 41
3.1.5 Storage Ring 43
3.1.6 Final Beam 43
3.2 Detector Theory 45
3.3 Incoming-beam Detectors 49
3.3.1 Position Detector (POS) 49
3.3.2 Position Sensitive silicon Pin diode Detector (PSP) 50
3.3.3 Rechts Oben Links Unten Detector (ROLU) 51
3.4 Target Area Detectors 52
3.4.1 Crystal Ball 53
3.4.2 Silicon Strip Detectors (SSDs) 54
3.5 ALADIN (A LArge DIpole magNet) 55
3.6 Outgoing-fragment Detectors 56
3.6.1 Grosser FIber detektors (GFIs) 56
3.6.2 Time of Flight Wall (TFW) 57
3.6.3 Other Detectors 60

4 Calibrations **61**

4.1 Time Calibration 61
4.2 SSDs 61
4.2.1 Pixel Runs 62
4.2.2 Pedestal Correction 62
4.2.3 VA Chip Gain Synchronisation 64
4.2.4 Dead Strip Identification 64
4.2.5 Eta Correction 66
4.2.6 Gain Matching 69

4.2.7 Eta Dependent Position Correction 70
4.3 PSP Detector 71
4.3.1 Position Calibration 71
4.3.2 Energy Calibration 73
4.3.3 Position Dependent Energy Calibration 73
4.4 Crystal Ball 73
4.4.1 Gamma-ray Calibration 73
4.4.2 Charged Particle Calibration 74
4.5 GFIs 74
4.6 TFW 76

5 Analysis **77**

5.1 Tracking 77
5.2 Problems with Tracking 81
5.3 Efficiency Calculations 88
5.4 Cross Section Calculation 89
5.5 TFW Peak Widths 94

6 Results & Discussion **96**

6.1 Breakup cross sections on proton target 96
6.2 Breakup cross sections on ^{12}C target 98
6.3 Energy Dependence 99
6.4 Change with Neutron Number 111
6.4.1 Single neutron knockout 111
6.4.2 Single proton knockout 112
6.4.3 α cluster knockout 114
6.4.4 ^{6}He knockout 118

6.4.5 Total reaction Cross Sections 118
6.5 TFW Peak Widths 119

7 Summary & Future Work 121

Appendices 127

A Deformed Harmonic Oscillator & Two Centre Harmonic Oscillator code 128

B Deformed Harmonic Oscillator Plots for beryllium isotopes 132

C Two Centre Harmonic Oscillator Plots for beryllium isotopes 139

D Efficiency values 142

E Breakup cross sections on proton target 144

F Data tables for breakup cross sections on proton target 149

G Breakup cross sections on ^{12}C target 156

H Data tables for breakup cross sections on ^{12}C target 161

List of Figures

1.1 Examples of crystalline structures for various isotopes 3

1.2 Relationship between number of alpha particle bonds and binding energy 4

1.3 An Ikeda diagram 5

1.4 Rotational bands for ^{16}O 7

1.5 An energy level diagram of the rotational bands of ^{20}Ne 9

1.6 An Ikeda diagram for neutron rich isotopes 11

1.7 Centre-of-mass distributions for ^{6}He+^{4}He scattering 13

1.8 A plot of the natural log of cross section against Q-value 15

2.1 The energy levels of the DHO 18

2.2 The DHO density distribution of ^{9}Be with (010)n 19

2.3 π and σ molecular bonds 22

2.4 Alternate configurations for molecular bonds 22

2.5 The Hückel density distribution of ^{9}Be with 1 πn 23

2.6 ACM configurations for ^{24}Mg 26

2.7 The development of clustering with mass in beryllium 28

2.8 AMD density distributions for beryllium 29

2.9 AMD non-normal-parity density distributions for beryllium 30

2.10 AMD cluster separation distance with mass for beryllium 31

2.11 Cluster breakup cross sections for beryllium 32

2.12 GFMC density of ^{8}Be 33

2.13 A simplified schematic of the excited states in a nucleus 35

2.14 A schematic of the QFS knockout reaction 37

3.1 The setup for the S393 experiment 38

3.2 A schematic of the beam production at GSI 39

3.3 A schematic of a linear accelerator 40

3.4 A schematic of the GSI FRS 42
3.5 A graph showing the available counts of each isotope 44
3.6 Energy dependence of gamma-ray interaction processes 46
3.7 A schematic diagram of gamma-rays interacting in a detector 46
3.8 Energy loss of a heavy charged particle in matter 47
3.9 The POS detector 50
3.10 Particle identification from online analysis of the S393 experiment . . . 51
3.11 The ROLU detector 52
3.12 The target wheel and target chamber detectors 53
3.13 The crystal ball detector 54
3.14 Arrangement of the silicon detectors 55
3.15 ALADIN 56
3.16 A schematic diagram of the GFI detectors 57
3.17 The Time of Flight Wall 58
3.18 A schematic of event reconstruction for the TFW 58
4.1 Pedestal values for SSD 3 63
4.2 A comparison of the pedestals found for an SSD 64
4.3 A schematic explanation of the importance of dead strip identification . 65
4.4 A plot of the SSDs, used to identify dead strips 66
4.5 SSD energy dependence on proximity to readout strip 67
4.6 The eta dependence of the measured energy of the s-side of an SSD . . 67
4.7 The eta dependence profile of the measured energy of the s-side of an SSD 68
4.8 A graph of eta corrected energy for the s-side of an SSD 68
4.9 Gain matching of strips on an SSD 69
4.10 Measured energy against known energy in the in-beam SSDs 70
4.11 The eta dependent position effect on an SSD 71

4.12 Distorted position data on the PSP detector 72
4.13 Corrected position data on the PSP detector 72
4.14 A GFI detector's fibres on the PMT 75
5.1 A spectrum showing charge selection during the tracking process 78
5.2 Comparison between tracker path and recorded hits 79
5.3 A well tracked fragment mass spectrum 80
5.4 A poorly tracked fragment mass spectrum 81
5.5 Losses in tracking due to detector efficiencies 82
5.6 Tracking resolution with and without GFIs 83
5.7 Horizontal displacement on the downstream SSDs 84
5.8 Outgoing angle against TFW horizontal position for charge 2 fragments 85
5.9 Outgoing angle against TFW horizontal position for charge 4 fragments 86
5.10 A plot of TFW horizontal position against mass to charge ratio 87
5.11 The finite horizontal acceptance of the TFW 88
5.12 Peak widths on the TFW for empty target runs 95
5.13 Corrected TFW peak widths for all targets 95
6.1 Cross sections for reaction fragments of ^{10}Be+p at 4987 MeV 97
6.2 Cross sections for reaction fragments of ^{12}B+p at 6400 MeV 97
6.3 Cross sections for reaction fragments of ^{11}Be+^{12}C at 4679 MeV 98
6.4 Cross sections for reaction fragments of ^{13}B+^{12}C at 6541 MeV 99
6.5 A comparison of cross sections for ^{10}Be+p at 4987 and 5366 MeV . . . 100
6.6 A comparison of cross sections for ^{11}Be+p at 4679 and 5043 MeV . . . 101
6.7 A comparison of cross sections for ^{12}Be+p at 4402 and 4751 MeV . . . 101
6.8 A comparison of cross sections for ^{10}B+p at 2910 and 4616 MeV 102
6.9 A comparison of cross sections for ^{13}B+p at 6075 and 6541 MeV 103
6.10 A comparison of cross sections for ^{14}B+p at 5777 and 6228 MeV 103

6.11 A comparison of cross sections for ^{15}B+p at 5502 and 5938 MeV 104
6.12 A comparison of cross sections for ^{10}Be+^{12}C at 3152, 4987 and 5366 MeV 105
6.13 A comparison of cross sections for ^{11}Be+^{12}C at 2931, 4679 and 5042 MeV 106
6.14 A comparison of cross sections for ^{12}Be+^{12}C at 4401 and 4750 MeV . . 107
6.15 A comparison of cross sections for ^{10}B+^{12}C at 2909 and 4615 MeV . . . 107
6.16 A comparison of cross sections for ^{13}B+^{12}C at 6074 and 6541 MeV . . . 108
6.17 A comparison of cross sections for ^{14}B+^{12}C at 5776 and 6227 MeV . . . 109
6.18 A comparison of cross sections for ^{15}B+^{12}C at 5502 and 5938 MeV . . . 110
6.19 Cross sections and Q-values for single neutron knockout for $^{10-12}$Be+p 111
6.20 Cross sections and Q-values for single neutron knockout for $^{8,10-15}$B+p 112
6.21 Cross sections and Q-values for single proton knockout for ^{7,9,10,12}Be+p 112
6.22 Cross sections and Q-values for single proton knockout for ^{8,10,11,13}B+p 113
6.23 Cross sections for single proton knockout from ^{8}B on ^{12}C 114
6.24 Cross sections and Q-values for α cluster knockout for $^{7,9-12}$Be+p . . . 114
6.25 Cross sections and Q-values for α cluster knockout for $^{8,10-15}$B+p . . . 115
6.26 Cross sections and Q-values for fragments from $^{7,9-12}$Be+p 116
6.27 Cross sections and Q-values for fragments from $^{8,10,11,13-15}$B+p 116
6.28 Clusterisation in beryllium: AMD cluster separation vs. cross sections . 117
6.29 Cross sections for knockout of ^{6}He from $^{9-12}$Be+p and $^{8,13-15}$B+p . . . 118
6.30 Total reaction cross sections for boron and beryllium beams 118
6.31 TFW peak widths for single neutron knockout 119
6.32 TFW peak widths for single proton knockout 119
6.33 TFW peak widths for alpha cluster knockout 120
7.1 Existing and proposed acceleration setup for FAIR at GSI 123
7.2 Proposed R^{3}B setup at FAIR 123
7.3 The barrel section of CALIFA 124

7.4 A schematic of the Silicon Tracker 125

7.5 A schematic of the Silicon tracker in with CALIFA 125

B.1 The DHO density distribution of a (000) neutron 132

B.2 The DHO density distribution of a (001) neutron 132

B.3 The DHO density distribution of a (002) neutron 132

B.4 The DHO density distribution of a (010) neutron 133

B.5 The DHO density distribution of ^{7}Be 133

B.6 The DHO density distribution of ^{8}Be 133

B.7 The DHO density distribution of ^{9}Be with (002)n 134

B.8 The DHO density distribution of ^{10}Be with 2 (002)n 134

B.9 The DHO density distribution of ^{10}Be with 2 (010)n 134

B.10 The DHO density distribution of ^{10}Be with (010)n & (002)n 135

B.11 The DHO density distribution of ^{11}Be with 2 (002)n & (001)n 135

B.12 The DHO density distribution of ^{11}Be with 3 (002)n 135

B.13 The DHO density distribution of ^{11}Be with 3 (010)n 136

B.14 The DHO density distribution of ^{11}Be with (002)n & 2 (010)n 136

B.15 The DHO density distribution of ^{12}Be with 2 (010)n & 2 (002)n 136

B.16 The DHO density distribution of ^{12}Be with 3 (010)n & (002)n 137

B.17 The DHO density distribution of ^{12}Be with 4 (002)n 137

B.18 The DHO density distribution of ^{12}Be with 4 (010)n 137

B.19 The DHO density distribution of ^{12}Be with (010)n & 3 (002)n 138

C.1 The Hückel density distribution of a neutron in the σ-type configuration 139

C.2 The Hückel density distribution of a neutron in the π-type configuration 139

C.3 The Hückel density distribution of ^{9}Be with 1 σn 140

C.4 The Hückel density distribution of ^{10}Be with 2 σn 140

C.5 The Hückel density distribution of ^{10}Be with 2 πn 140

C.6 The Hückel density distribution of ^{10}Be with 1 πn & 1 σn 141
C.7 The Hückel density distribution of ^{11}Be with 2 πn & 1 σn 141
C.8 The Hückel density distribution of ^{12}Be with 2 πn & 2 σn 141
E.1 Cross sections for reaction fragments of ^{7}Be+p at 2569 MeV 144
E.2 Cross sections for reaction fragments of ^{9}Be+p at 3404 MeV 144
E.3 Cross sections for reaction fragments of ^{10}Be+p at 5366 MeV 144
E.4 Cross sections for reaction fragments of ^{11}Be+p at 4679 MeV 144
E.5 Cross sections for reaction fragments of ^{11}Be+p at 5043 MeV 145
E.6 Cross sections for reaction fragments of ^{12}Be+p at 4402 MeV 145
E.7 Cross sections for reaction fragments of ^{12}Be+p at 4751 MeV 145
E.8 Cross sections for reaction fragments of ^{8}B+p at 3420 MeV 145
E.9 Cross sections for reaction fragments of ^{10}B+p at 2910 MeV 146
E.10 Cross sections for reaction fragments of ^{10}B+p at 4616 MeV 146
E.11 Cross sections for reaction fragments of ^{11}B+p at 4324 MeV 146
E.12 Cross sections for reaction fragments of ^{13}B+p at 6075 MeV 146
E.13 Cross sections for reaction fragments of ^{13}B+p at 6541 MeV 147
E.14 Cross sections for reaction fragments of ^{14}B+p at 5777 MeV 147
E.15 Cross sections for reaction fragments of ^{14}B+p at 6228 MeV 148
E.16 Cross sections for reaction fragments of ^{15}B+p at 5502 MeV 148
E.17 Cross sections for reaction fragments of ^{15}B+p at 5938 MeV 148
G.1 Cross sections for reaction fragments of ^{7}Be+^{12}C at 2569 MeV 156
G.2 Cross sections for reaction fragments of ^{9}Be+^{12}C at 3404 MeV 156
G.3 Cross sections for reaction fragments of ^{10}Be+^{12}C at 3153 MeV 156
G.4 Cross sections for reaction fragments of ^{10}Be+^{12}C at 4987 MeV 156
G.5 Cross sections for reaction fragments of ^{10}Be+^{12}C at 5366 MeV 157
G.6 Cross sections for reaction fragments of ^{11}Be+^{12}C at 2932 MeV 157

G.7 Cross sections for reaction fragments of ^{11}Be+^{12}C at 5043 MeV 157

G.8 Cross sections for reaction fragments of ^{12}Be+^{12}C at 4402 MeV 157

G.9 Cross sections for reaction fragments of ^{12}Be+^{12}C at 4751 MeV 158

G.10 Cross sections for reaction fragments of ^{8}B+^{12}C at 3420 MeV 158

G.11 Cross sections for reaction fragments of ^{10}B+^{12}C at 2910 MeV 158

G.12 Cross sections for reaction fragments of ^{10}B+^{12}C at 4616 MeV 158

G.13 Cross sections for reaction fragments of ^{11}B+^{12}C at 4324 MeV 159

G.14 Cross sections for reaction fragments of ^{12}B+^{12}C at 6400 MeV 159

G.15 Cross sections for reaction fragments of ^{13}B+^{12}C at 6075 MeV 159

G.16 Cross sections for reaction fragments of ^{14}B+^{12}C at 5777 MeV 159

G.17 Cross sections for reaction fragments of ^{14}B+^{12}C at 6228 MeV 160

G.18 Cross sections for reaction fragments of ^{15}B+^{12}C at 5502 MeV 160

G.19 Cross sections for reaction fragments of ^{15}B+^{12}C at 5938 MeV 160

List of Tables

2.1 A comparison of the density distributions of the DHO and TCHO . . . 24

5.1 Half-lifes of isotopes of helium 85

5.2 Cross section calculations for reaction fragments of ^{10}Be at 5366 MeV. . 93

6.1 Cross sections for single proton knockout from ^{8}B and ^{10}B on ^{12}C target 113

D.1 Efficiency values for beryllium beams 142

D.2 Efficiency values for boron beams 143

F.1 Cross sections for reaction fragments of ^{10}Be+p at 4987 MeV 149

F.2 Cross sections for reaction fragments of ^{10}Be+p at 5366 MeV 149

F.3 Cross sections for reaction fragments of ^{11}Be+p at 4679 MeV 149

F.4 Cross sections for reaction fragments of ^{11}Be+p at 5043 MeV 150

F.5 Cross sections for reaction fragments of ^{12}Be+p at 4402 MeV 150

F.6 Cross sections for reaction fragments of ^{12}Be+p at 4751 MeV 150

F.7 Cross sections for reaction fragments of ^{7}Be+p at 2569 MeV 151

F.8 Cross sections for reaction fragments of ^{9}Be+p at 3404 MeV 151

F.9 Cross sections for reaction fragments of ^{10}B+p at 2910 MeV 151

F.10 Cross sections for reaction fragments of ^{10}B+p at 4616 MeV 151

F.11 Cross sections for reaction fragments of ^{11}B+p at 4324 MeV 152

F.12 Cross sections for reaction fragments of ^{12}B+p at 6400 MeV 152

F.13 Cross sections for reaction fragments of ^{13}B+p at 6075 MeV 152

F.14 Cross sections for reaction fragments of ^{13}B+p at 6541 MeV 153

F.15 Cross sections for reaction fragments of ^{14}B+p at 5777 MeV 153

F.16 Cross sections for reaction fragments of ^{14}B+p at 6228 MeV 154

F.17 Cross sections for reaction fragments of ^{15}B+p at 5502 MeV 154

F.18 Cross sections for reaction fragments of ^{15}B+p at 5938 MeV 155

F.19 Cross sections for reaction fragments of ^{8}B+p at 3420 MeV 155

H.1 Cross sections for reaction fragments of ^{10}Be+^{12}C at 3153 MeV 161
H.2 Cross sections for reaction fragments of ^{10}Be+^{12}C at 4987 MeV 161
H.3 Cross sections for reaction fragments of ^{10}Be+^{12}C at 5366 MeV 161
H.4 Cross sections for reaction fragments of ^{11}Be+^{12}C at 2932 MeV 162
H.5 Cross sections for reaction fragments of ^{11}Be+^{12}C at 4679 MeV 162
H.6 Cross sections for reaction fragments of ^{11}Be+^{12}C at 5043 MeV 162
H.7 Cross sections for reaction fragments of ^{12}Be+^{12}C at 4402 MeV 163
H.8 Cross sections for reaction fragments of ^{12}Be+^{12}C at 4751 MeV 163
H.9 Cross sections for reaction fragments of ^{7}Be+^{12}C at 2569 MeV 163
H.10 Cross sections for reaction fragments of ^{9}Be+^{12}C at 3404 MeV 164
H.11 Cross sections for reaction fragments of ^{10}B+^{12}C at 2910 MeV 164
H.12 Cross sections for reaction fragments of ^{10}B+^{12}C at 4616 MeV 164
H.13 Cross sections for reaction fragments of ^{11}B+^{12}C at 4324 MeV 165
H.14 Cross sections for reaction fragments of ^{12}B+^{12}C at 6400 MeV 165
H.15 Cross sections for reaction fragments of ^{13}B+^{12}C at 6075 MeV 165
H.16 Cross sections for reaction fragments of ^{13}B+^{12}C at 6541 MeV 166
H.17 Cross sections for reaction fragments of ^{14}B+^{12}C at 5777 MeV 166
H.18 Cross sections for reaction fragments of ^{14}B+^{12}C at 6228 MeV 167
H.19 Cross sections for reaction fragments of ^{15}B+^{12}C at 5502 MeV 167
H.20 Cross sections for reaction fragments of ^{15}B+^{12}C at 5938 MeV 168
H.21 Cross sections for reaction fragments of ^{8}B+^{12}C at 3420 MeV 168

1 Introduction

This thesis presents an analysis of data taken by the R^3B (Reactions with Relativistic Radioactive Beams) collaboration at the GSI Helmholtz Centre for Heavy Ion Research in Darmstadt, Germany in 2010. The analysis focuses on breakup cross-sections and alpha particle knockout reactions of the form $p(^{10}Be, p\alpha)^6He$, at beam energies between 260 and 540 MeV per nucleon, investigating the possibility of alpha clustering in the ground state of neutron rich light nuclei. This chapter gives a brief history of the theory of cluster structures accompanied by selected experimental evidence.

1.1 Clustering

A coarse view of a nucleus may describe it as approximately spherical and homogeneous in its composition of nucleons. However, this is overly simplistic; a more accurate description must include deviations such as axial deformations which can lead to collective behaviour, for example rotations. In light nuclear systems deviations from such spherical structures are found not only in the form of axial deformation, but also clustering; for some nuclei it can be energetically favourable for the nucleons to be arranged as smaller clusters or subunits within the parent nucleus. For example, a ^{28}Si nucleus can consist of a ^{24}Mg and an alpha particle, or a ^8Be nucleus can consist of two alpha particles. Alpha particles have a high binding energy per nucleon compared with other light nuclei [1], meaning that it is energetically favourable for the nucleus to coalesce into alpha particles. The idea of alpha clustering dates back to 1911 with the experiments performed by Rutherford and co-workers demonstrating spontaneous emission of alpha particles. Rutherford suggested that the alpha particles could be preformed within the parent nucleus [1]. In part this led to the initial assumption that nuclei were formed

---

[1] The binding energy of an alpha particle is just over 7 MeV per nucleon.

from alpha particles. However, following the discovery of the neutron by Chadwick in 1932, this idea was largely dropped in favour of independent particle models. Independent particle models attempt to describe the nucleus in terms of the average interaction between the constituent nucleons via a mean-field which can be described by an associated potential. More complex models such as the ab initio Green's Function Monte Carlo method, treat the interaction of every nucleon with its co-constituents using realistic nucleon-nucleon interactions. These calculations are extremely challenging and none have reached beyond A=12. One of the principle attractions of cluster models is their simplicity.

One of the earliest significant contributions came in 1938 when Hafstad and Teller proposed a model for clustering in N=Z and A=4n (n = 2, 3, 4...) nuclei (i.e. "alpha-conjugate" nuclei: nuclei whose constituents can form an integer number of alpha particles), though the model was extended to allow a single additional or missing proton or neutron [8]. The model developed used a parametrised $\alpha-\alpha$ interaction to calculate the binding energies of $n\alpha$ systems. The principle assumption regarding the binding energy was in an analogy between the alpha particles and closed shell atoms, that is to say that the interaction forces would be additive in nature and the addition of a third alpha particle would not change the interaction between the first two. This analogy was continued in the extension to allow an additional nucleon or nucleon hole: the additional nucleon was treated like an electron compared to the nucleus, i.e. of negligible mass compared to the core and covalently exchanged between the alpha particles (and hence had an associated exchange energy). The number of bonds for a given number of alpha particles was calculated by drawing the various crystalline structures that the particles could take, some examples of such structures are shown in Figure 1.1, taken from [20] (there adapted from [11]).

Amongst the many conclusions of Hafstad and Teller's work was the idea that bind-

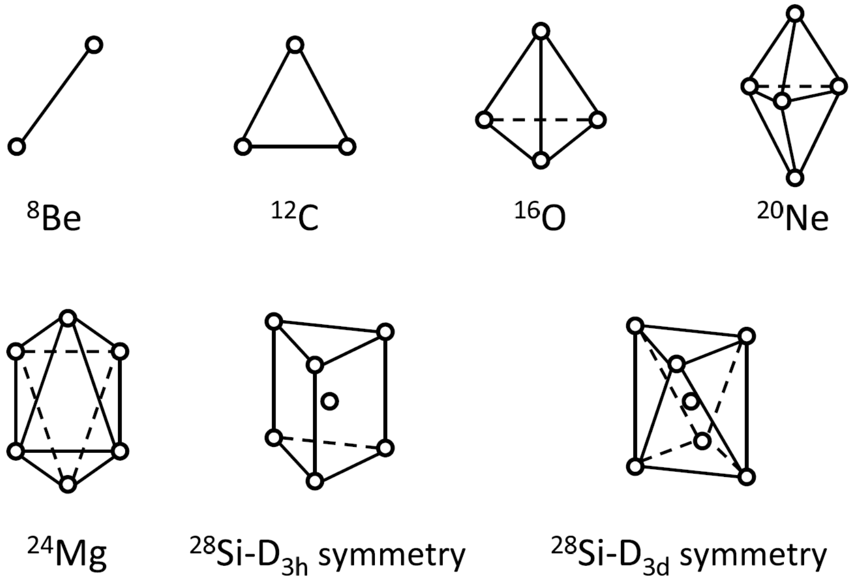

Figure 1.1: Some examples of crystalline structures for various isotopes, as described in 1967 by Brink whose ideas closely followed Hafstad and Teller. Image from [20] (there adapted from [11]).

ing energy was directly proportional to the number of bonds between the alpha particles, as shown by Figure 1.2. While Hafstad and Teller acknowledged the limitations of this approach both in theory and the results (for example the binding energy predicted for ^{8}Be was approximately 2.5 MeV too high), they also highlighted the comparatively greater discrepancies in the independent particle models of the time.

Cluster models, on the other hand, simplify this complexity by treating the clusters as inert objects and dealing with the interaction between the clusters only. They tend to use phenomenological interactions adjusted to reproduce known properties.

Hafstad and Teller's picture indicates clustering might appear in the ground state of such nuclei. However, 30 years later there was a further contribution which refined this thinking. In 1968 Ikeda suggested that for all nuclei with N=Z and A=4n, clustering would occur with a prominence related to the proximity to the decay threshold for that channel [2]. This is shown in the Figure 1.3, in what is known as the "Ikeda diagram".

The premise of the Ikeda diagram is that as the threshold for cluster decay is ap-

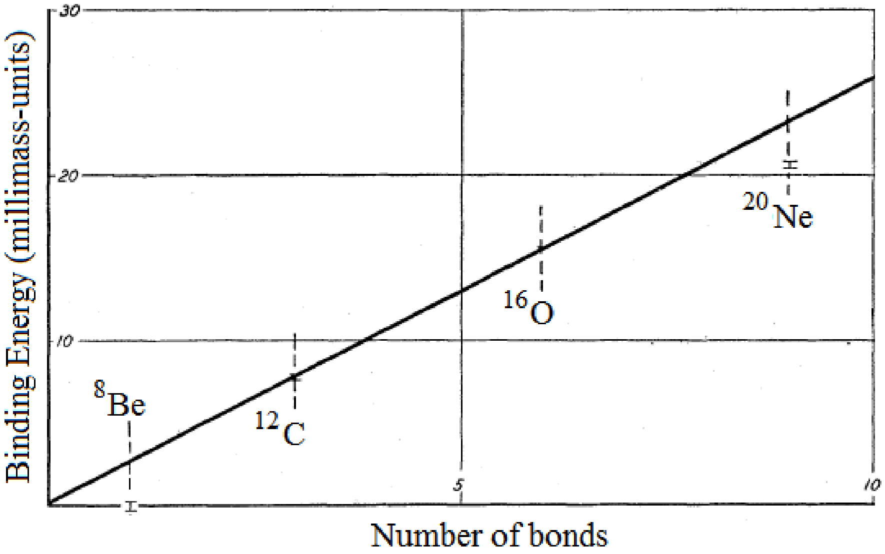

Figure 1.2: The relationship between number of alpha particle bonds and binding energy proposed by Hafstad and Teller, adapted from [8].

proached, the nucleus can take on a structure which will need minimal reconfiguration to decay by emitting the cluster fragment. In other words the nucleus can convert the internal excitation energy into the binding energy of the clusters. An analogy can be drawn to fission - a heavy nucleus does not simply split in two, but goes through several stages (e.g. necking) during which it changes from its original shape to a shape requiring less reconfiguration after the fission. Figure 1.3 also shows that as excitation energy increases clustering increases in prominence, moving from a core with an alpha particle, to a smaller core with several alpha particles, and ending with a structure composed only of alpha particles.

A further development occurred in the 1970s. Calculations for systems which have the form of a core plus an alpha particle (or just two larger clusters e.g. ^{28}Si in the form of ^{16}O+^{12}C), were solved using a two body Schrödinger equation. This solution is useful, in that it allows a comparison between the theory and experimentally measurable quantities such as decay lifetimes and nuclear charge radii. Good agreement for this

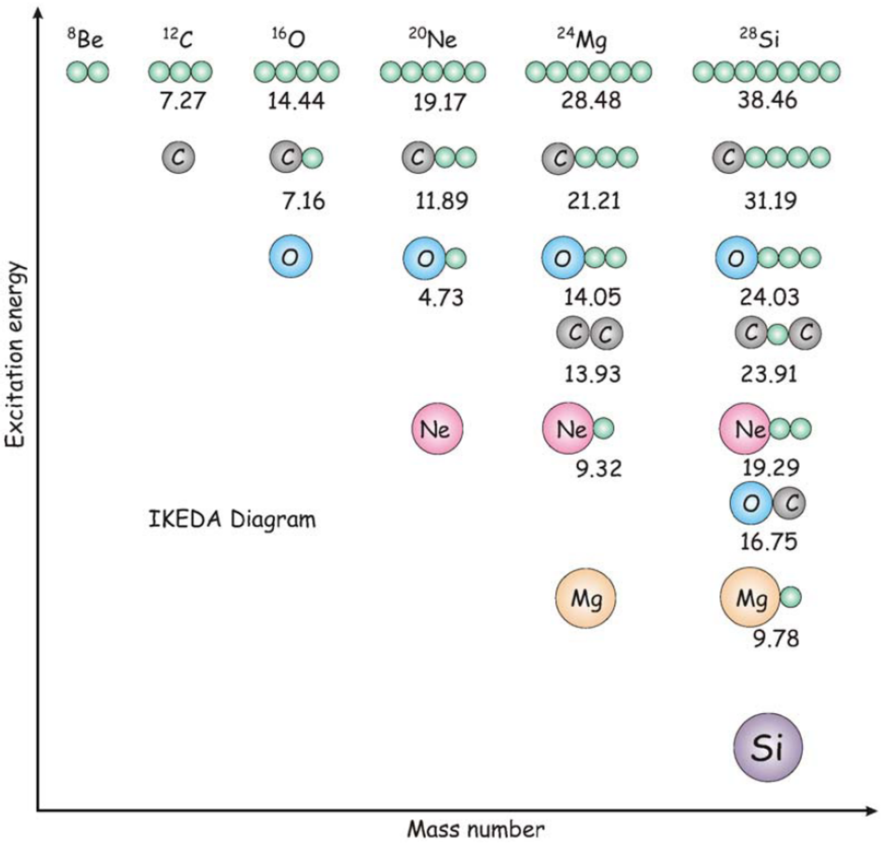

Figure 1.3: An Ikeda diagram, modified from [3]. All energies are in MeV. The x-axis represents nucleus mass and so the columns are different cluster forms of a given isotope. The proposed relationship between excitation energy and clustering can be clearly seen. For example, a ^{24}Mg *nucleus may take the form of a* ^{20}Ne *nucleus with an alpha particle at an excitation energy of 9.32 MeV, two* ^{12}C *nuclei at 13.93 MeV, an* ^{16}O *nucleus with two alpha particles at 14.05 MeV, a* ^{12}C *nucleus with three alpha particles at 21.21 MeV or, six alpha particles at 28.48 MeV.*

comparison has been shown by Buck, Dover & Vary, for example in the case of the ^{20}Ne nucleus [4]. These calculations link the quantum mechanical approach with the rather schematic ideas associated with the Ikeda diagram.

1.2 Experimental examples of Clustering

1.2.1 ^{16}O

The Ikeda model suggests that ^{16}O has a ^{12}C + alpha structure at an excitation energy around 7.16 MeV and a four alpha particle structure around 14.44 MeV. Figure 1.4 shows experimental evidence in support of the Ikeda model; the plot shows experimental rotational bands measured for states in ^{16}O as identified by plotting excitation energy against angular momentum, J. The gradient of the line for a given rotational band corresponds to the moment of inertia, I, for the nucleus in that state (where the gradient is $\frac{\hbar^2}{2I}$). Since it is possible to calculate classical moments of inertia for a given arrangement of spheres, the experimental moments of inertia can be related back to shapes. The contour plots on Figure 1.4 indicate the alpha cluster configurations suggested by the moment of inertia calculations. These calculations do not rule out the possibility that the nucleus maintains a homogeneous composition throughout the deformed shape. However the subsequent decay into two ^{8}Be, which itself is believed to have a 2α cluster structure, and from there into four ^{4}He, supports the idea of four alpha clusters [10]. However, it should be pointed out that there are many experimental data points which may be connected to form rotational bands and band assignments are far from certain. For example, a more recent investigation has found no evidence for the arrangement of four alpha particles in a chain [17].

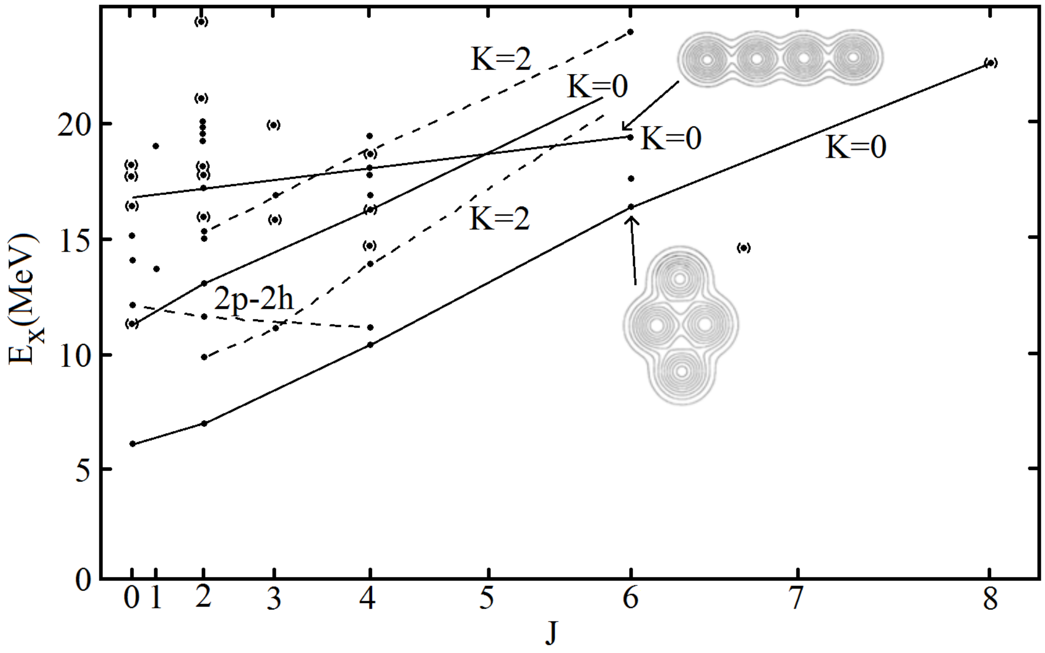

Figure 1.4: Rotational bands for ^{16}O *adapted from [21], there adapted from [9]. The lines joining points are the proposed rotational bands. K indicates the spin assignment of the rotational band. The contour plots show the alpha cluster configuration given by the Alpha Cluster Model, see Section 2.4.*

1.2.2 ^{20}Ne

^{20}Ne is a good example of cluster structure; in the configuration of an ^{16}O+α it has the binding advantage of both clusters being closed shell, doubly magic, nuclei. Figure 1.5 shows the energy levels of the rotational bands predicted by the alpha + core model described earlier, compared with experimental measurements. There is a good agreement in these rotational bands, and the model also describes the alpha decay widths well; this supports the clustered picture of ^{20}Ne. It should be noted that α-decay widths measure the propensity for the nucleus to decay into the core+α and hence are a rather precise determination of the structure.

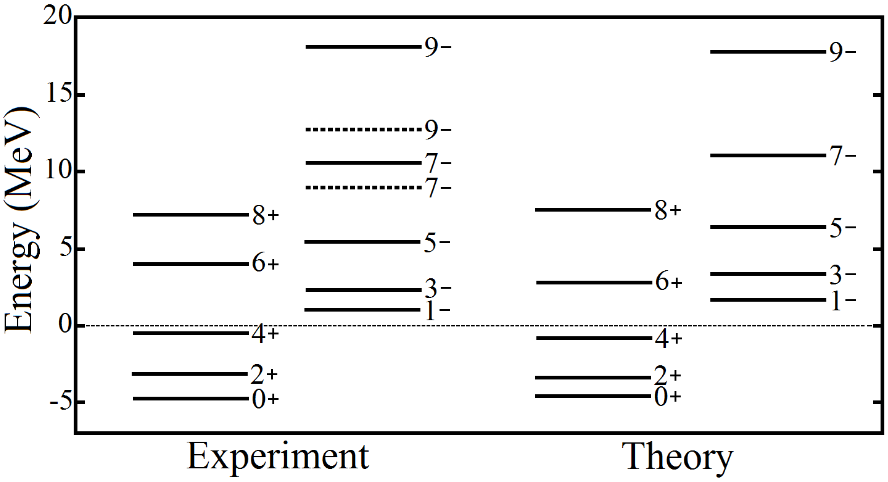

Figure 1.5: An energy level diagram of the rotational bands of ^{20}Ne*, adapted from [7]. On the left are experimental values and on the right the alpha + core model's predictions.*

1.3 Neutron Rich Clustering

In the 1990s the development of radioactive ion beams made it possible to investigate reactions with increasingly exotic nuclei, such as nuclei towards the neutron drip line - where the addition of a neutron results in an almost immediate neutron decay, as opposed to β-decay which imposes millisecond lifetimes. Results from these investigations are of great importance in the understanding of nuclear structure, as they have challenged traditional models which up to that point worked relatively well for the stable nuclides. For example they provide a greater sensitivity to the asymmetric dependencies in the nucleon force and expose features of the neutron-neutron interaction within the nucleus. The present work is particularly concerned with clustering in neutron rich isotopes.

It has recently been shown by Kanada-En'yo and Horiuchi that the valence neutrons in neutron rich nuclei with an underlying cluster structure can enhance binding in a manner analogous to covalent bonds in atomic systems, leading to the name "nuclear molecules" [5]. For example, while ^{8}Be is unbound to decay into two alpha particles, ^{9}Be is stabilised by the additional neutron forming a covalent bond between the two clusters, similar to an electron being shared between two protons in a covalent bond forming a H_2^+ ion. In both cases, the enhanced binding stems from the de-localisation of the electron or neutron lowering the overall kinetic energy contribution.

The possibility of covalently bound molecular cluster structures leads to a different Ikeda diagram for neutron rich isotopes, as seen in Figure 1.6.

A similarity between both the standard and the neutron rich Ikeda diagram is that they describe clustering at different excitation energies, typically away from the ground state. However, arguments have been made for the existence of clustering also in the ground state of neutron rich nuclei. The binding energy of a nucleus depends on the interplay of the p-p, n-n and n-p interactions. In neutron rich nuclei the number of n-p interactions is comparatively reduced. However, the n-p interaction has a very important contribution to the binding energy and nuclei may adjust their structure to maximise the potential for n-p interactions. Close to the neutron drip line, binding may be enhanced by maximising the surface area of the nucleus i.e. by forming clusters; these clusters would optimise the neutron-proton interaction, by allowing the clusters (and therefore the protons) to be surrounded by a "sea" of neutrons. The clusterisation maximises the surface area of the alpha particle cores.

Despite theoretical predictions that clustering exists in the ground state of some neutron rich nuclei, there has been very little experimental investigation [16]. This has been due to the relative difficulty of exploring the structure of the ground state (see Sections 2.9 and 2.10). The present thesis introduces a novel method for exploring this structure. This study of the structure of neutron rich nuclei is important in understanding nuclear structure in general, but is also of interest in other fields, for example it is directly relevant to the formation of heavier elements via the r-process in supernovae [12].

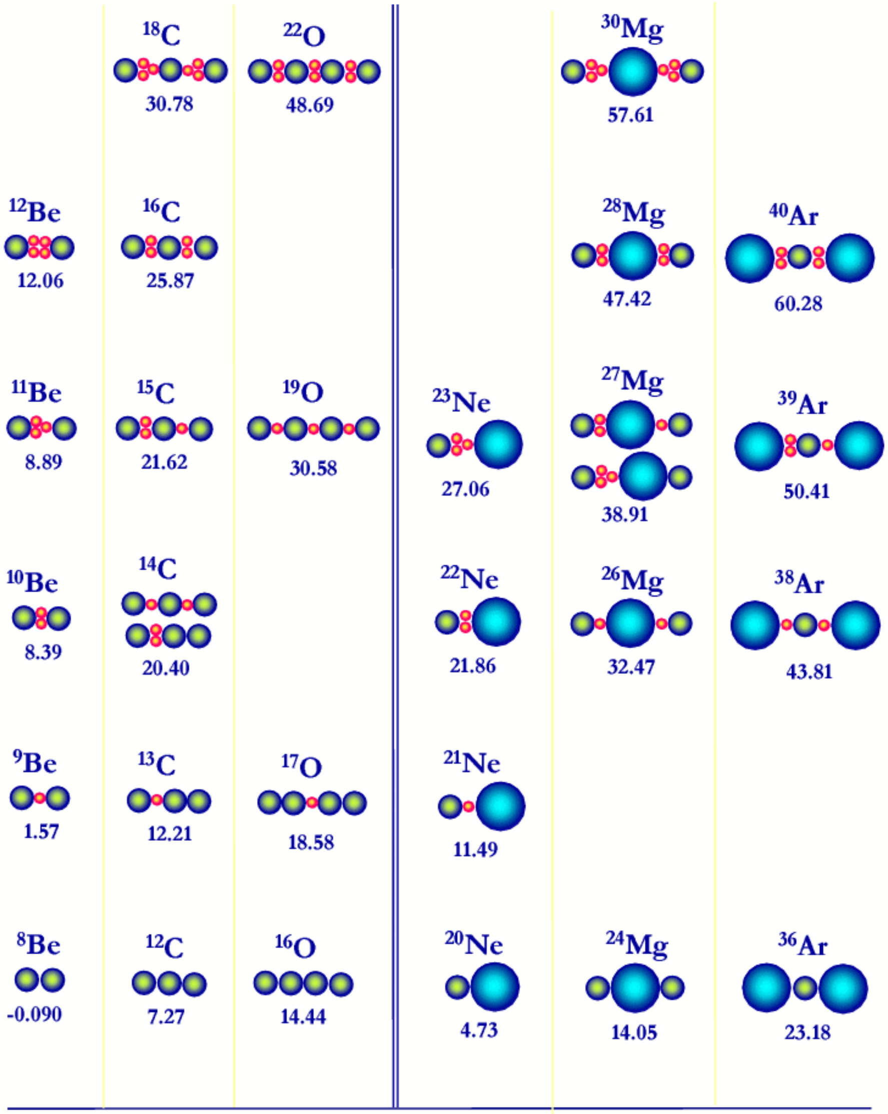

Figure 1.6: An Ikeda diagram for neutron rich isotopes, taken from [6]. All energies are in MeV. The small red circles are neutrons, the medium green circles are alpha particles and the large blue circles are ^{16}O. *Here the columns are separate elements and neutron number increases vertically. For example, five isotopes of magnesium are shown, from the N=Z* ^{24}Mg *up to neutron rich* ^{30}Mg. *These isotopes are shown as having the structure of an* ^{16}O *core with two alpha particles, separated by a varying number of valence neutrons.*

1.4 Experimental examples of Neutron Rich Clustering

1.4.1 ^{10}Be

As can be seen in Figure 1.6, it has been suggested that ^{10}Be may possess an $\alpha - 2n - \alpha$ structure in an excited state at 8.39 MeV. Evidence in support of this structure has been found via resonant elastic scattering of ^{6}He+^{4}He. Figure 1.7 shows a comparison between the experimental centre-of-mass distribution and theoretical simulations of the experiment indicating that the state discovered was $J^{\pi} = 4^{+}$. This information is shown in the inset of Figure 1.7 which is a plot of excitation energy against angular momentum, in fact $J(J+1)$, for the given rotational band. The gradient of the line, g, called the rotational parameter, is inversely proportional to the moment of inertia of the nucleus, I, as shown in Equation 1.1.

$$g = \frac{\hbar^2}{2I} \tag{1.1}$$

The value for the rotational parameter for ^{10}Be, 0.20 MeV can be compared to the same value for the ground states of ^{8}Be and ^{9}Be which are 0.57 MeV and 0.53 MeV respectively. As discussed in Section 1.2.1, measurements of the moment of inertia can be used to infer the structure of the nucleus; these values indicate a large separation between two clusters as the structure of ^{10}Be, giving strong support for the $\alpha - 2n - \alpha$ structure, where the two neutrons sit between the two alpha particles increasing their separation relative to ^{8}Be [13].

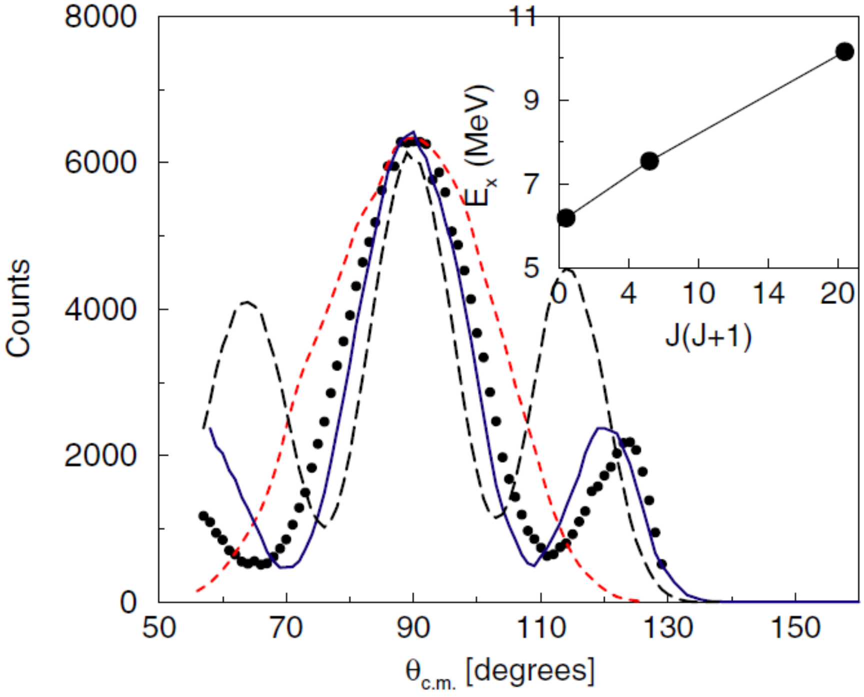

Figure 1.7: A comparison between the experimental centre-of-mass distribution (black circles) and three simulations for ^{6}He+^{4}He *scattering (spin 2 (red-dashed), 4 (blue) and 6 (black-dashed)), from [13].*

1.4.2 ^{14}Be

Evidence for clustering has been found in ^{14}Be by comparison with its mirror nuclei ^{14}B [14]. Measurements were made of the cross sections for neutron removal and cluster breakup for both nuclei. As can be seen in Figure 1.8, the cross sections for reaction fragments from the breakup of both ^{14}Be and ^{14}B are strongly correlated with the Q-value for the reaction producing them, with the exception of ^{14}Be breaking up into ^{6}He + ^{8}He which is enhanced. This enhancement supports cluster structure in ^{14}Be as compared to ^{14}B, in agreement with the idea of the development of clustering at the drip line.

In an analogue of the measurements performed in this thesis, Ashwood et al. [14] performed a series of measurements of the cluster knockout and neutron removal cross sections for a range of beryllium isotopes plus ^{14}B and ^{16}C. These measurements involved colliding the nucleus to be investigated with a carbon target to observe what fragments the nucleus preferentially broke into. In principle, this provides an insight into the structure of the projectile.

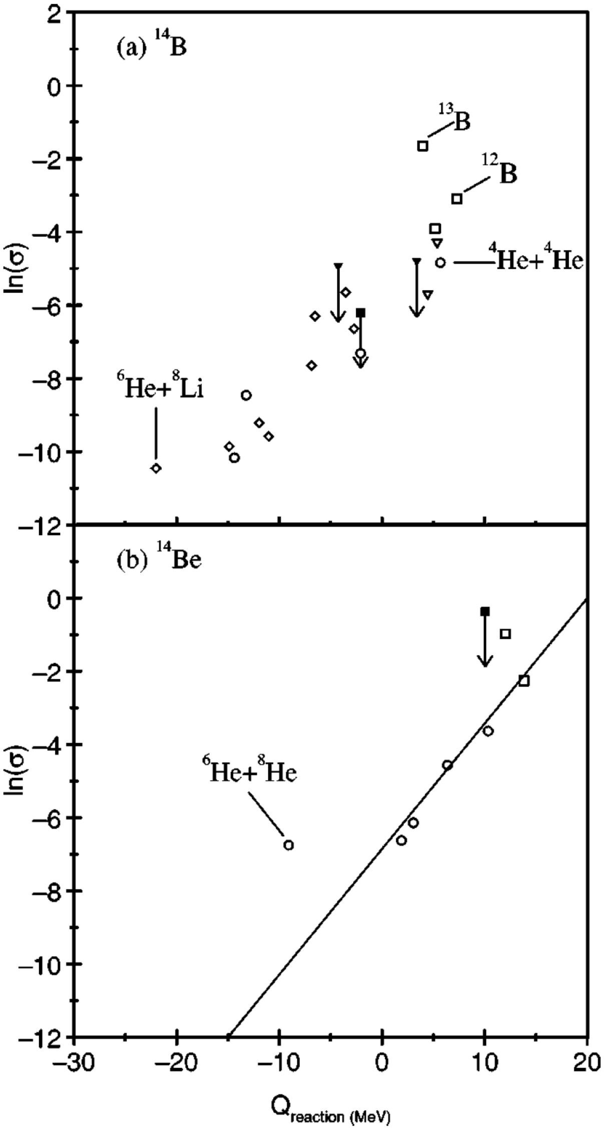

Figure 1.8: A plot of the natural log of cross section against Q-value for a) ^{14}B *and b)* ^{14}Be*, from [14].*

2 Theory

This chapter introduces the theoretical framework which underpins the experimental work, and informs the investigation. A historical and developmental view of clustering models is introduced in order of increasing complexity. Comparisons are made between models, in particular between the Deformed Harmonic Oscillator and the Two-Centre Harmonic Oscillator based on calculations using these approaches. These calculations were made using code written by the author (included in Appendix A) based on the models described in [19].

Quasi-free kinematics are discussed as relevant to the reaction channel of the subsequent analysis. Two methods of measuring alpha clustering in the ground state are introduced and critiqued.

2.1 Deformed Harmonic Oscillator (DHO)

The nuclear shell model is used to calculate the energy levels occupied by nucleons in a spherical nucleus. In analogy with the electrons of the atomic shell model, a large difference between two adjacent energy levels means that a relatively large amount of energy is required to excite a nucleon occupying the lower energy level to the higher level. The total number of nucleons occupying up to and including the lower level associated with a shell closure is referred to as a “magic number”. Any nucleus which has nucleons occupying energy levels up to a magic number will be particularly stable, owing to the large excitation energy required to cross the gap. Consequently, an additional nucleon will behave as a valence nucleon, interacting with a stable core. For nuclei further from magic numbers, the assumption of a spherical core becomes less accurate; the interactions between the valence nucleons and the core cause prolate and oblate deformations which need to be applied to the nuclear potential, as exploited by Nilsson in 1955 [18].

A simple treatment represents such a deformed nucleus by a 3-dimensional harmonic oscillator potential deformed along the z-axis with independent frequencies for the directions parallel and perpendicular to the axis of deformation. A nucleon's wave-function, along the direction of deformation can then be calculated, using the resulting formula:

$$\psi(z) = \frac{1}{\sqrt{2^n n!}} \left(\frac{\mu\omega}{\pi\hbar}\right)^{\frac{1}{4}} H_n \left(\sqrt{\frac{\mu\omega}{\hbar}} z\right) e^{\frac{-\mu\omega z^2}{2\hbar}}, \tag{2.1}$$

where n is the number of oscillator quanta associated with the z direction, μ is the mass, ω is the frequency, H_n is a hermite polynomial of order n and z is the position [19]. This wave-function is the same for each spatial dimension (x, y and z) so each nucleon's kinetic energy (implying excitation energy) can be described in terms of the oscillator quanta: (n_x, n_y, n_z). The harmonic oscillator is a useful framework to explore nuclear properties, because it can be solved analytically. Solving gives the energy of the quantum level as:

$$E = \hbar\omega_\perp n_\perp + \hbar\omega_z n_z + \frac{3}{2}\hbar\omega_0, \tag{2.2}$$

where $\omega_0 = \frac{2\omega_\perp + \omega_z}{3}$, $\omega_\perp$ is the frequency along both non-deformed axes and ω_z is the frequency along axis of deformation. A useful measure of the quadrupole deformation is defined as:

$$\epsilon_2 = \frac{\omega_\perp - \omega_z}{\omega_0}. \tag{2.3}$$

When ϵ_2 is negative, i.e. $\omega_z > \omega_\perp$, the deformation is oblate. When ϵ_2 is positive, i.e. $\omega_z < \omega_\perp$, the deformation is prolate.

Equation 2.3 allows the energy levels to be plotted as a function of deformation, as shown in Figure 2.1.

Figure 2.1 shows that the magic numbers change with deformation. This is caused by the gradient of the relationship between energy and deformation for a given combi-

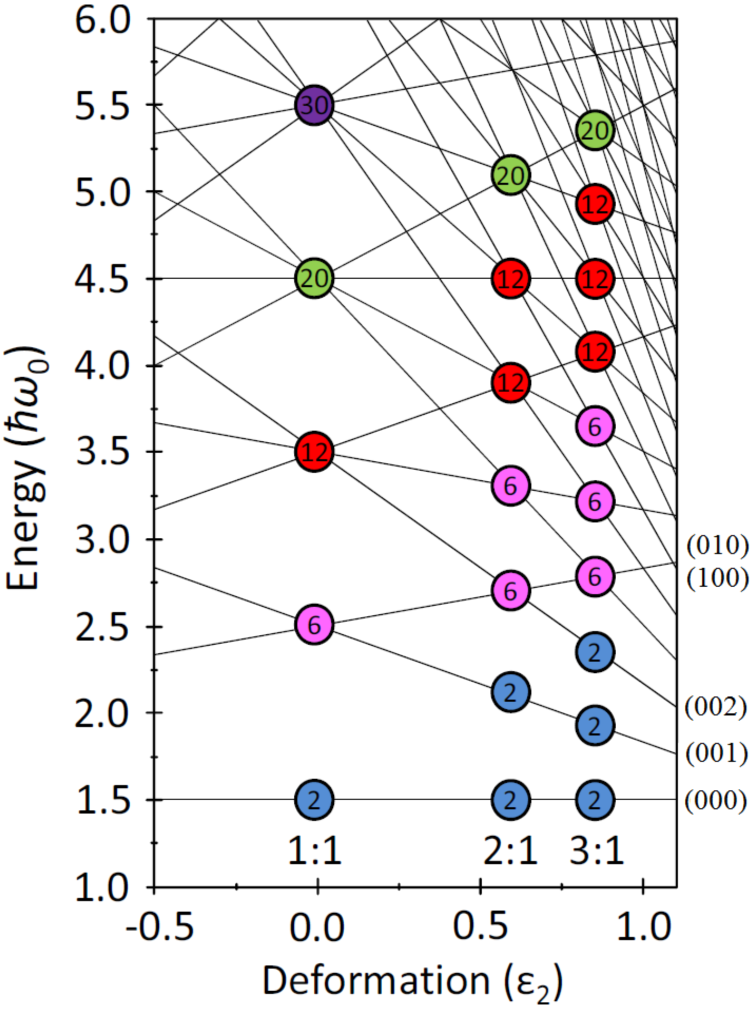

Figure 2.1: The energy levels of the DHO as a function of deformation, taken from [20] (there adapted from [21]). The coloured circles represent degeneracies of each level. The energy levels shift as the oscillation frequencies change with deformation. The ratios above the x-axis of the diagram are the ratio of the nucleus' major axis to minor axes. This is useful in visualising the deformed nucleus.

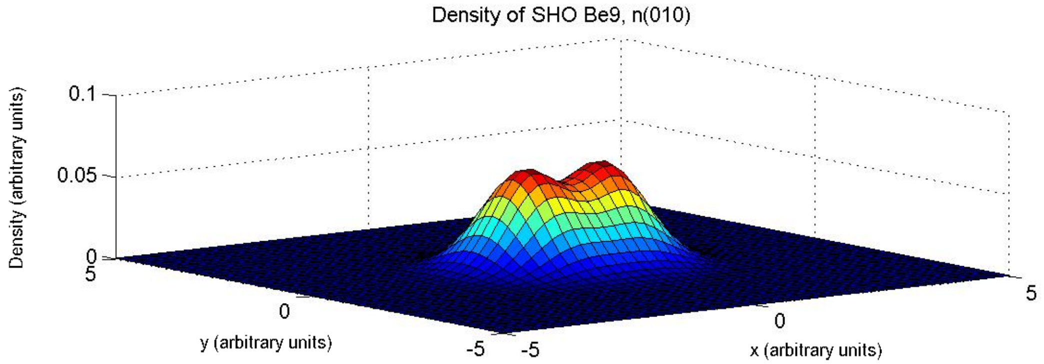

Figure 2.2: The density distribution of ^{9}Be *with a (010) neutron, calculated using the DHO model introduced in [19]. A clear clustered structure can be seen, in that there are two distinct peaks of maximum density, with a less dense region between them.*

nation of oscillator quanta and also the degeneracy of combinations, for example (010) (100) are degenerate in energy since $n_\perp$ in Equation 2.2 represents oscillator quanta from both non-deformed axes. The gradient of the relationship between energy and deformation for a given combination of oscillator quanta can be understood by considering in Equation 2.3 how $\omega_\perp$ and ω_z change under the condition of increasing deformation and constant ω_0. Assuming constant nuclear volume, to increase deformation the perpendicular axes must be constricted as the deformed axis expands. This will result in $\omega_\perp$ increasing and ω_z decreasing in inverse proportion with the change in the size of their associated potentials, thus changing the energy.

There is a repeated pattern of degeneracy with deformation, with the spherical (i.e. 1:1) pattern repeating twice at 2:1 deformation and three times at 3:1. This suggests multiple harmonic oscillators with a number proportional to the deformation, that is to say a clustered structure, or the appearance of alternate symmetry.

This is supported by the associated density distributions, which show strong cluster structure. For example Figure 2.2 is a typical density distribution produced by this method, in this case for ^{9}Be $(000)^4, (100)^4, (010)^1$.

Appendix B contains the density distribution plot produced for other isotopes of

Beryllium, using the same method. Most show some evidence of clustering, others demonstrate strong evidence of clustered structure.

2.2 Two Centre Harmonic Oscillator (TCHO)

Given the clustered nature suggested by the harmonic oscillator, a more appropriate approach to modelling clustering may be the Two Centre Harmonic Oscillator. Here each alpha particle cluster is represented by its own harmonic oscillator potential. One framework to make such a calculation for neutron rich nuclei in is the Hückel method. The Hückel method is used to calculate the energy of orbital elections in molecules; however the idea can be adapted for a nuclear system composed of alpha clusters and valence neutrons [19].

Clustering is assumed and each cluster is modelled as a separate potential using the harmonic oscillator method. These clusters are then separated. The density distribution of any valence nucleons is calculated from the combined potential of the clusters. The final density distribution is the combination of the clusters and the valence neutrons. It is important to note that while the clusters are represented by harmonic oscillator potentials, because they are spatially separated the Pauli principle does not prevent nucleons within the two separate potentials having the same quantum numbers.

The wave-functions of the neutrons in a two cluster system are calculated using the following formula:

$$\psi(z) = \frac{1}{\sqrt{\pi 2^n n!}} \left(H_n\left(z - z_1\right) e^{\frac{-\omega (z-z_1)^2}{2}} \pm H_n\left(z - z_2\right) e^{\frac{-\omega (z-z_2)^2}{2}} \right) \tag{2.4}$$

where n is the number of oscillator quanta, ω is the frequency, H_n is a hermite polynomial of order n and z is the position (z_1 and z_2 are the locations of the two clusters). This wave-function is the same for each spatial dimension (x, y and z), with the exception that the centres of the clusters are only displaced in the z dimension. Equation 2.4 is the normalised superposition of a valence neutron's wave-function over both alpha clusters. When the two terms are added this is called "gerade", and where they are subtracted "ungerade"[2].

The details of the neutron wave-function depend on the clusters. Using ^{9}Be as an example, the neutron must reside in a p-orbital because the shell model ground-state spin and parity of the ^{5}He ground state would be $\frac{3}{2}^-$, which is the state occupied by the unpaired neutron. It is then linear combinations of these p-orbitals which form the molecular bonds. The π (pi) and σ (sigma) bonds are both formed by the combination of two p-states but, as shown in Figure 2.3, the orientation of the p-states used for the different bonds are orthogonal to each other. The π and σ configurations were chosen as likely to resulting in bound systems. Figure 2.4 shows alternate configurations with the same states, but added where they were previously subtracted and vice versa. These configurations give distributions less likely to resulting in binding systems because they have a greater curvature in their wave-functions, which results in a higher energy state.

The choice of bond has a strong effect on the similarity between the Hückel method and the DHO.

Figure 2.5 is the density distribution for ^{9}Be with a π bond. Again strong cluster structure can be seen, similar to that observed in Figure 2.2.

Appendix C contains the density distribution plots produced for other isotopes of Beryllium, using the TCHO. The lighter nuclei with π bonds show the strongest cluster structure. This is an interesting result as it would be expected that σ bonds show the strongest cluster structure. However this expectation is based on mechanisms not present in the simplistic TCHO model: in a more realistic system the σ bond is associated with stronger clustering as it becomes energetically favourable for the

---

[2] "gerade" and "ungerade" are German words and can be translated to "even" and "odd".

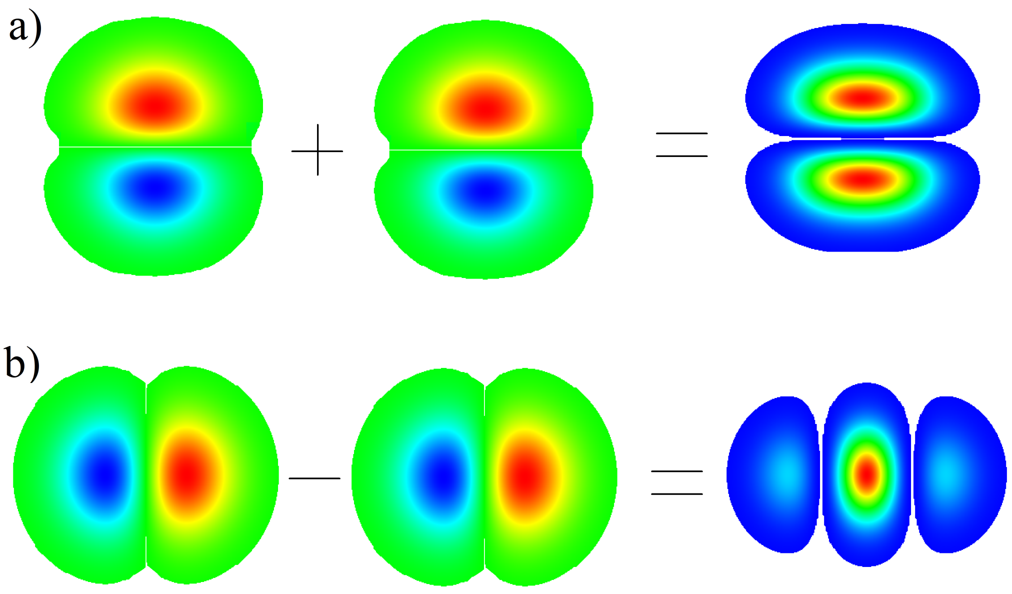

Figure 2.3: a) π ((010) gerade) and b) σ ((001) ungerade) molecular bonds. Both bonds are formed from p-orbitals with similar though orthogonal distributions. However, the produced bonds are very different in shape, and result in different overall density distributions for the nucleus.

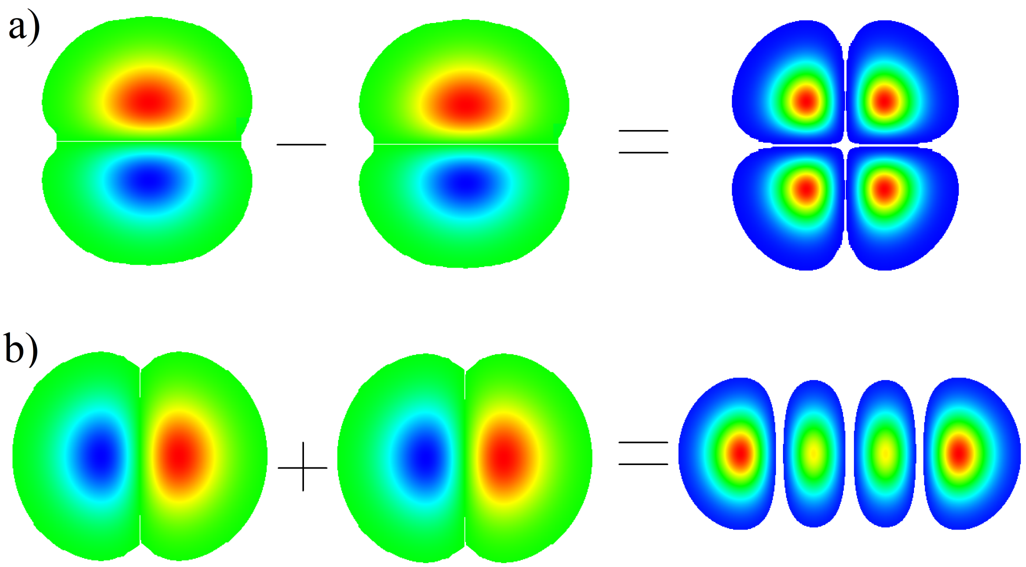

Figure 2.4: Alternate configurations for molecular bonds, a) (010) ungerade and b) (001) gerade.

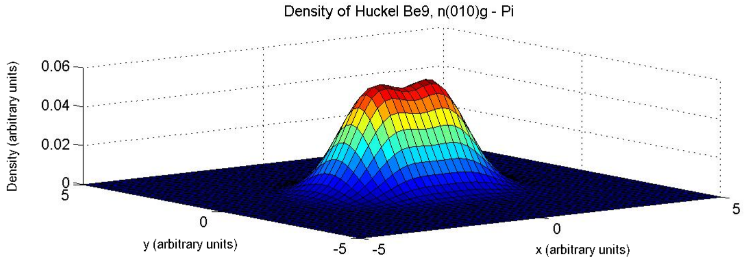

Figure 2.5: The density distribution of $^{9}\mathrm{Be}$, *calculated using the Hückel method with a* π*-type configuration. This distribution shows clear cluster structure, in much the same way as the DHO.*

neutron to be positioned in between the two cores experiencing a repulsion caused by the Pauli exclusion principle; essentially if the valence neutron has to enter the alpha particle, it must occupy a high energy state, making such an occurrence energetically unfavourable.

2.3 Comparison of DHO and TCHO

A comparison can be made between the density distributions produced by the DHO and the TCHO. The method used is an overlap function, calculated with the formula shown below:

$$Overlap = \frac{\sum\limits_{y,z} \rho_A \rho_B}{\sqrt{\sum\limits_{y,z} {\rho_A}^2 \sum\limits_{y,z} {\rho_B}^2}} \tag{2.5}$$

To clarify, this overlap function calculates the product of the two density distributions, ρ_A and ρ_B, at each yz point and then sums these values. The overlap value of identical distributions is unity as the overlap function is normalised by the denominator. The overlap value along the the non-deformed axes, x and y, will be unity. As such summing over y may seem unnecessary and in most cases will not affect the result, but it avoids the requirement of choosing a given y value in the yz plane over which to sum z. This is useful, as an arbitrarily chosen value would, for some distributions, lie along a minima

Isotope	DHO	TCHO	Overlap Value
^{9}Be	^{8}Be + n(010)	^{8}Be + n(010)g	0.9962
^{9}Be	^{8}Be + n(002)	^{8}Be + n(001)u	0.9939
^{10}Be	^{8}Be + 2n(010)	^{8}Be + 2n(010)g	0.9950
^{10}Be	^{8}Be + n(010) + n(002)	^{8}Be + n(001)u + n(010)g	0.9957
^{10}Be	^{8}Be + 2n(002)	^{8}Be + 2n(001)u	0.9821
^{11}Be	^{8}Be + 2n(010) + n(002)	^{8}Be + 2n(010)g + n(001)u	0.9963
^{12}Be	^{8}Be + 2n(010) + 2n(002)	^{8}Be + 2n(010)g + 2n(001)u	0.9894
n	n(010)	n(010)g	0.9631
n	n(002)	n(001)u	0.5839

Table 2.1: The overlap integrals of density distributions of various isotopes of beryllium, calculated using the DHO and the TCHO. In the case of the TCHO, the 'g's and 'u's indicate gerade and ungerade.

and so the overlap value would be undefined, as the denominator would be 0.

Table 2.1 shows the overlap values between some of the density distributions produced by both models. The final two values compare the neutron density distributions only, with, as expected, the π bond showing far better agreement than the σ bond.

Typical overlap integrals between the DHO and the TCHO are around 0.98, showing excellent agreement between the DHO and the Hückel method. Agreement is best for π bonds, consistent with these distributions showing stronger cluster structure.

The substantial agreement between these two methods is of interest. Although the TCHO assumes cluster structure, the DHO not only predicts cluster structure without assumption, but also agrees with the TCHO in the details of that prediction.

These rather simple calculations show that cluster structures found in the mean-field approach are very similar to those that would be constructed explicitly using clusters plus molecular valence particles.

2.4 Brink-Bloch Alpha Cluster Model (ACM)

The Brink-Bloch ACM assumes that a collection of 2 protons and 2 neutrons will form a "quartet" with a coupled angular momentum of 0. It can therefore only be applied to nuclei with $N = Z$ and $A = 4n$, i.e. not neutron rich nuclei.

Having assumed that the nuclei are formed by clusters of alpha particles, wavefunctions are combined and the resulting energy of the system is then examined for local minima. The qualifier "local" should be emphasised, as an absolute energy minimum for a given nucleus might not be a clustered state but rather the ground state. The configuration of the clusters which produces this minimum can then be examined. This ultimately gives an idea of the structure the nuclei may possess when it is excited to an energy in the region of the local minimum. Figure 2.6 shows some examples of ACM configurations for ^{24}Mg.

This model is easier to apply to light systems, as a large amount of computational power is required and this increases significantly with the size of the system. Further, the results are more realistic for light systems as the mean field potential is more accurate [24].

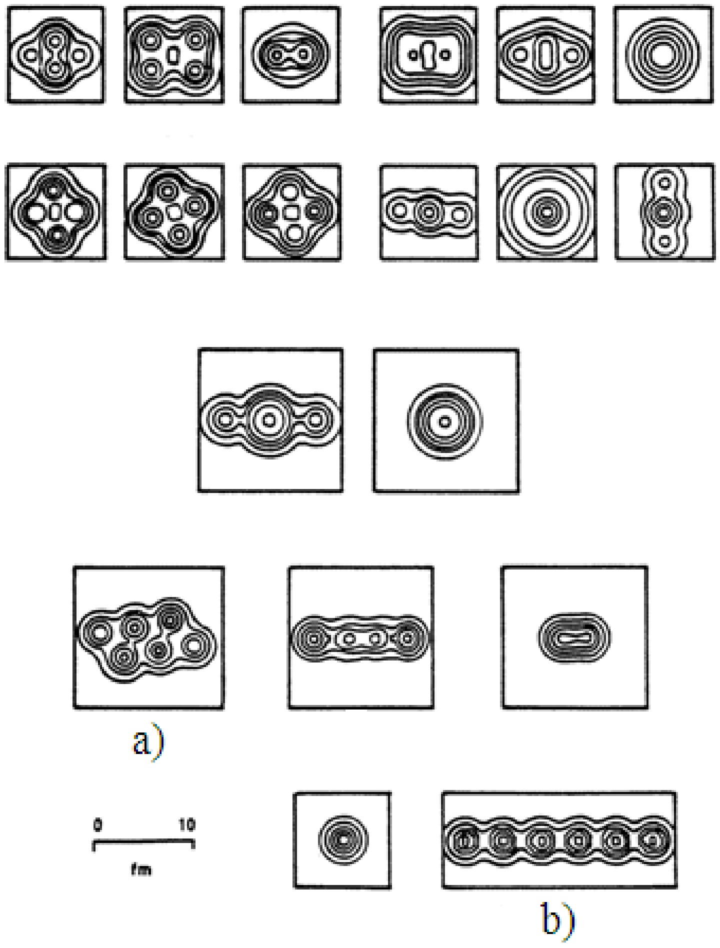

Figure 2.6: ACM configurations for ^{24}Mg*, adapted from [23]. A variety of configurations can be seen, including many clustered structures. In a) the 6 alpha clusters are groups of three, strongly resembling a triangular cluster configuration of* ^{12}C*, in this way ACM can predict the structure of* ^{24}Mg *as two* ^{12}C *nuclei. In b) the* ^{24}Mg *is configured as a chain of 6 alpha particles.*

2.5 Anti-symmetrised Molecular Dynamics (AMD)

Anti-symmetrised Molecular Dynamics (AMD) can be considered a development of ACM; rather than dealing with the wave-functions of alpha particles, AMD uses wave-functions of the individual nucleons. This gives AMD the important advantage of assuming neither clustering nor an inert core. This also allows calculations to be made for $N \neq Z$ nuclei, e.g. neutron rich nuclei.

Wave-functions are generated for each nucleon in the form of the Slater determinant of Gaussian wave packets with parameters for spatial, spin and isospin degrees of freedom. The wave-function for the nucleus is the superposition of the individual nucleon wave-functions. An effective interaction potential is assumed to govern the forces between individual nucleons, this allows the energy of the system to be minimised to obtain a prediction for the density distribution of the ground state. As with ACM, this process is computationally intensive, in the case of AMD the computational requirements are proportional to $A^{4\sim6}$ [35], and so easier for light nuclei; AMD has been used to study the structure of nuclei up to A=40 [36].

As described previously, valence neutrons can stabilise a clustered system by enhancing binding, analogous to an electron in a covalent bond in an atomic system. The nature of the construction of the AMD wave-function also allows an examination of the behaviour of the individual valence neutrons. In beryllium for example, the molecular orbits corresponding to either π or σ orbits are found, as shown previously in Figure 2.3 discussing the TCHO.

The orbitals occupied have a strong impact on the development of clustering, this is shown schematically by Figure 2.7. The three parallel lines represent the orbitals occupied by the valence neutrons. Taking ^{10}Be as an example, the two valence neutrons can be arranged in three ways, one represented by each line. The bottom line indicates that both valence neutrons are in the p-shell (with an orbital of π character), the middle

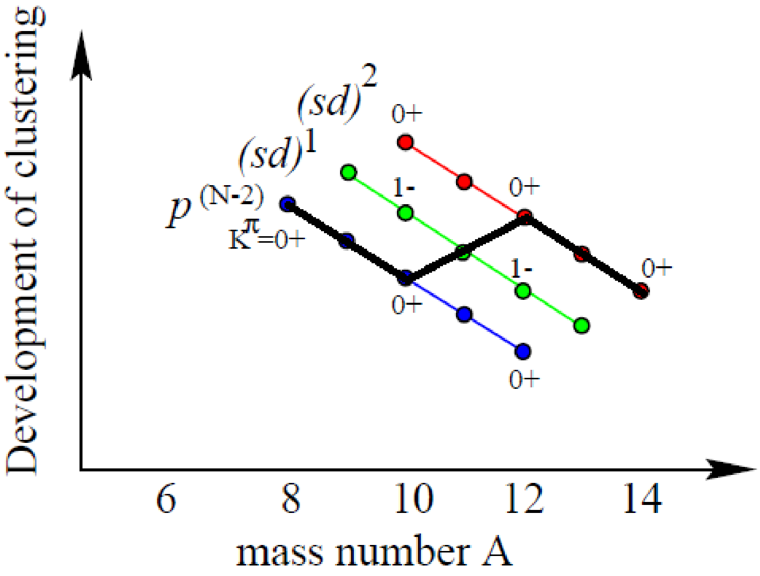

Figure 2.7: A schematic of the development of clustering as a function of mass number in beryllium isotopes. The parallel lines represent the orbitals occupied by the valence nucleons, K^π denotes the spin and parity of the states. Adapted from [5]

line that one valence neutron is in the p-shell and one is in the sd-shell (with an orbital of σ character), and the top line indicates that both valence neutrons are in the sd-shell. The thick overlaid black line shows how the ground state shifts between isotopes; this line therefore makes a prediction of ground state clustering as a function of increasing neutron number. So one would expect clustering to be strongest in the ground state of ^{14}Be, amplified by the σ valence neutrons.

Figure 2.8 shows the AMD density distributions predicted for beryllium isotopes. Cluster structure is most evident in the proton distribution, with decreasing separation of the cluster cores as neutron number increases. The AMD calculations shown in Figure 2.8 predict a 2 alpha-particle core structure for a range of isotopes of beryllium. It is worth noting that the separation is greatest for ^{8}Be and hence the cluster structure is most developed. From an experimental perspective ^{8}Be is unbound to decaying into two alpha particles and has a large decay width compared with the Wigner limit. Moreover, the rotational behaviour of the first 0^+, 2^+ and 4^+ states is consistent with two touching

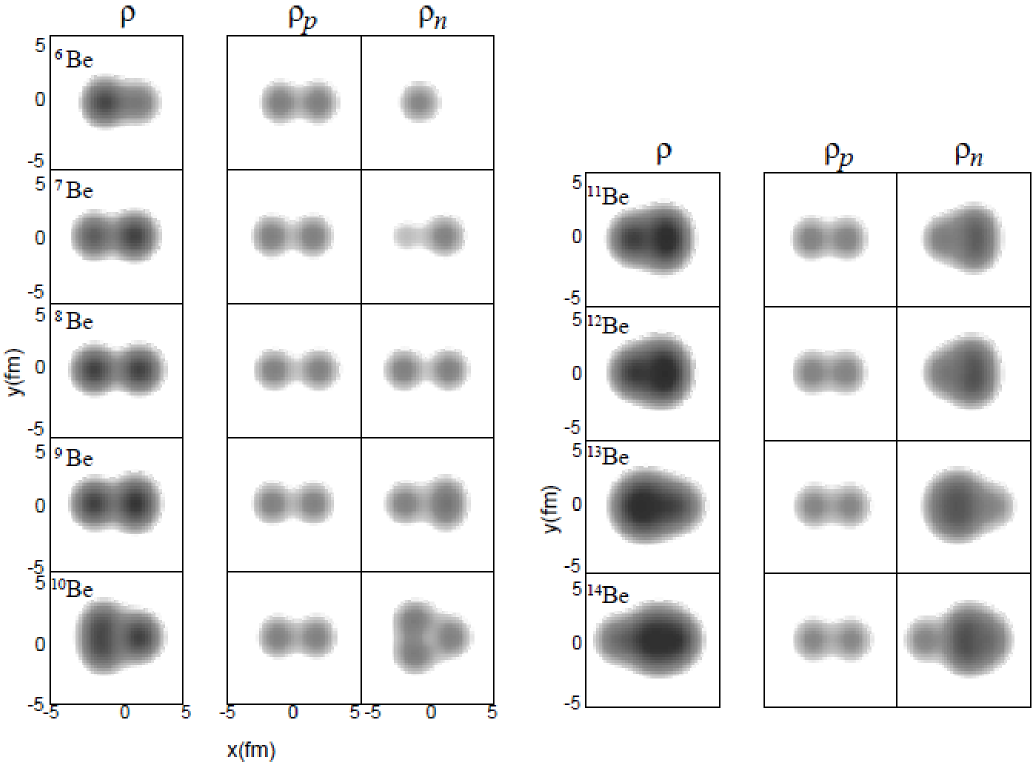

Figure 2.8: Density distributions for beryllium isotopes from mass 6 to 14. Adapted from [5]. The left most column is total density, and the two right hand columns are separated proton and neutron densities.

alpha particles. The AMD calculations predict that clustering will weaken as neutron number increases up to the neutron magic number at $N = 8$, but then become more pronounced for heavier isotopes as the neutron drip line is approached.

Neutron rich nuclei often exhibit deformation in the ground state. This can cause crossings of energy levels in the shell model, as previously discussed in Section 2.1. As a consequence of these crossings, the ground state spin and parity of a deformed nucleus may not be what would be expected from the standard shell model. Figure 2.9 shows the AMD densities of some non-normal (negative) parity states, again demonstrating the importance of the valence neutron wave-function, in this case via its effect on parity. At lower neutron numbers, the neutron density has a large overlap with the proton densities. As the neutron number increases however, some of the neutron density

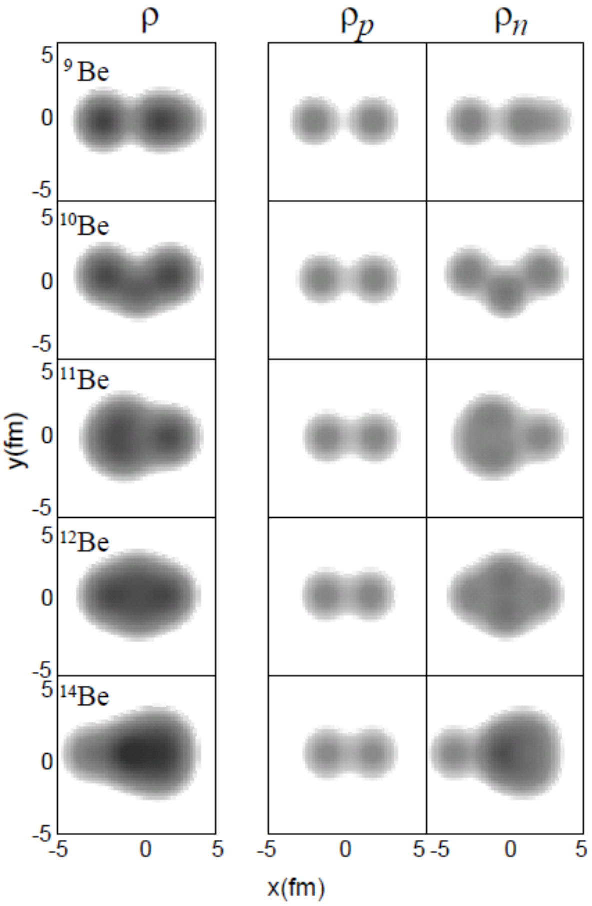

Figure 2.9: AMD densities of non-normal-parity states of neutron rich isotopes of beryllium, adapted from [5]. The left most column is total density, and the two right hand columns are separate proton and neutron densities.

is found outside of the cluster structure; the neutron densities of ^{10}Be and ^{12}Be in particular resemble clusters with shared valence neutrons. It should be noted that these configurations are the results of the AMD calculations before parity projection and hence do not always display good symmetry.

More generally, AMD predicts that for lithium, beryllium, boron and carbon, cluster structure will be most pronounced where $N = Z$, and weakest for $N = 8$ [25], this trend is clearly shown in Figure 2.10, a plot of cluster separation distance against mass number. Figure 2.10 also serves to demonstrate the importance of parity in AMD calculations.

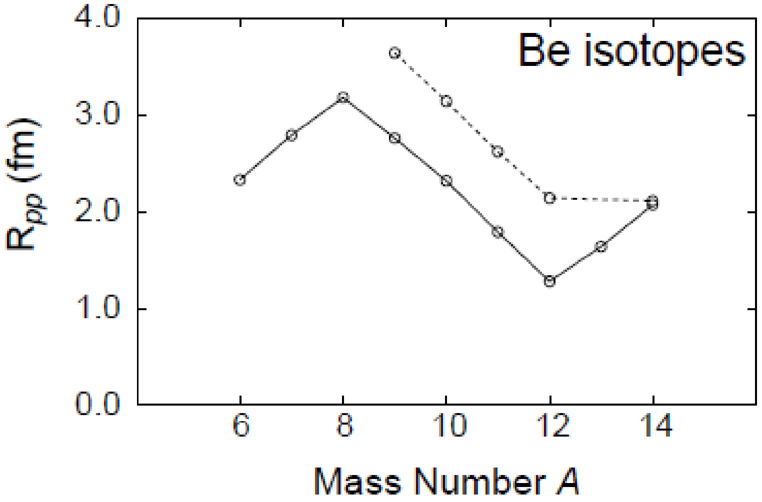

Figure 2.10: Cluster separation distance (R_{pp}), which is sensitive to the degree of clusterisation, plotted against mass number for normal and non-normal parity states of beryllium, from [5]. The solid line represents normal parity and the dotted line non-normal parity.

It is these predictions of the prominence of clustering, as well as trends with changing neutron number, that are compared to experimental data in this work. Figure 2.11 shows a previous attempt at evaluating the degree of clusterisation, by plotting cross section against mass for the cluster breakup of several isotopes of beryllium.

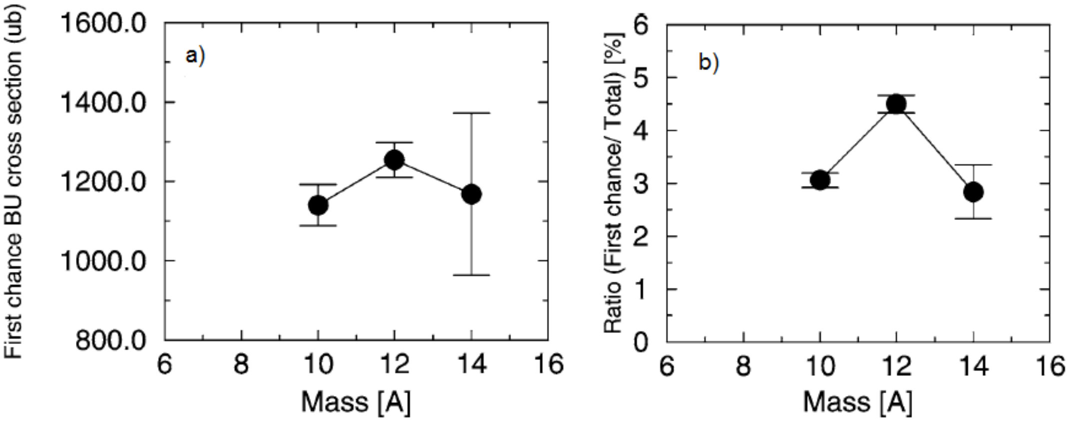

Figure 2.11: Cluster breakup cross sections as a function of incoming beryllium projectile mass adapted from [16]. a) is the raw cross sections, b) is the ratio between the cluster breakup cross sections and the total breakup cross sections.

2.6 Green's Function Monte Carlo (GFMC)

It can be argued that Green's Function Monte Carlo (GFMC) calculations are an improvement over AMD in much the same way that the AMD approach is an improvement over the ACM; the difference between the models comes from the removal of some approximations and assumptions. The model uses a realistic nucleon-nucleon interaction derived from nucleon scattering data, as opposed to the effective interaction potential of AMD which is a truncated interaction. This interaction also includes three body forces and the spin orbit interaction. The drawback to this method is that it is even more computationally demanding than AMD; the size of the wave-function on which the calculations are based, embiggens exponentially in proportion to the number of nucleons [26].

The GFMC approach produces interesting results, but importantly it reproduces some of the results of AMD. For example the alpha-alpha cluster structure can be clearly seen in ^{8}Be, shown in Figure 2.12.

This agreement goes some way in validating the use of AMD as a compromise

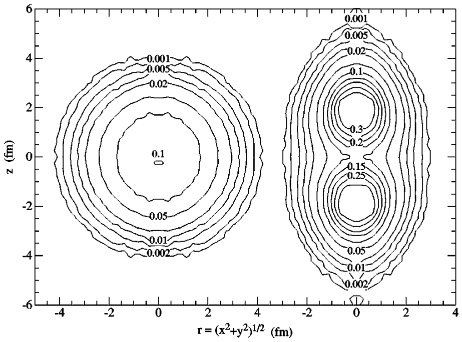

Figure 2.12: Density of ^{8}Be *as calculated by GFMC, from [27].*

between required computational power and naivety of the model (and therefore the significance of the produced densities). It would be interesting to observe the calculated densities of other Be isotopes generated using this approach.

2.7 Inverse Kinematics

Inverse kinematics is an important feature in the following experimental discussion. Briefly, inverse kinematics describes a reaction in which a heavy projectile is fired at a light target, for example a proton; there are several advantages over normal kinematics. Firstly, if one particle is radioactive, it is likely to be easier to produce this as the beam, rather than manufacture and maintain a pure, contained target, especially for very short half-lives. Secondly the reaction products are more likely to emerge at forward angles, reducing the required angular coverage of detectors; this however also results in a potential disadvantage: the compressed angular spread requires the detectors to have a finer spatial resolution in order to extract the available data. Finally because the target is lighter, it can recoil with higher energy, meaning that all the reaction products can be detected and a kinematically complete measurement made.

2.8 Quasi-Free Scattering (QFS)

QFS is an approximation that has previously been used to explore the properties of single nucleon states in the nucleus. If a reaction occurs with a sufficiently high centre of mass energy (in the range of 200 to 1000 MeV/nucleon [28]), the cross section for nucleon-nucleon reactions is relatively low. When a nucleon is knocked-out, this low cross section allows the simplifying assumption to be made that the remainder of the nucleus is undisturbed by the reaction. An important distinction must be made between "undisturbed" and "unexcited". When the nucleus has a nucleon knocked-out it is undisturbed and does not receive any excitation energy, but it may still be left in an excited state. For example if a neutron is knocked-out of an unexcited ^{12}Be it could be taken from the $1p_{1/2}$ level, leaving the $1/2^+$ ground state of ^{11}Be or it could be taken from the $1p_{3/2}$ level, leaving the $3/2^-$ excited state of ^{11}Be. To distinguish between the two situations it would be necessary to detect the gamma ray resulting from the de-excitation. It should also be clarified that while the nucleus is undisturbed this does not mean that it will be unaffected. For example if a neutron is knocked-out of a ^{9}Be the remainder of the nucleus would be ^{8}Be. ^{8}Be is unbound, so even without receiving any excitation energy this will result in a decay into two alpha particles.

QFS has been extensively, and successfully, used as a technique for nucleon knockout. For example, in [33] the reaction $^{16}\mathrm{O}(e, e'p)^{15}\mathrm{N}$ was used. Since the ground state spin and parity of ^{16}O is 0^+, the ^{15}N must possess the spin and parity of the knocked-out proton. In another example QFS was used to measure the cross section for knockout of a proton from ^{16}O either in the ground state or an excited state [30].

In Section 2.10 a method is described, making a novel use of QFS. In short, the method can be considered similar to nucleon knockout experiments, simply knocking out an alpha particle instead.

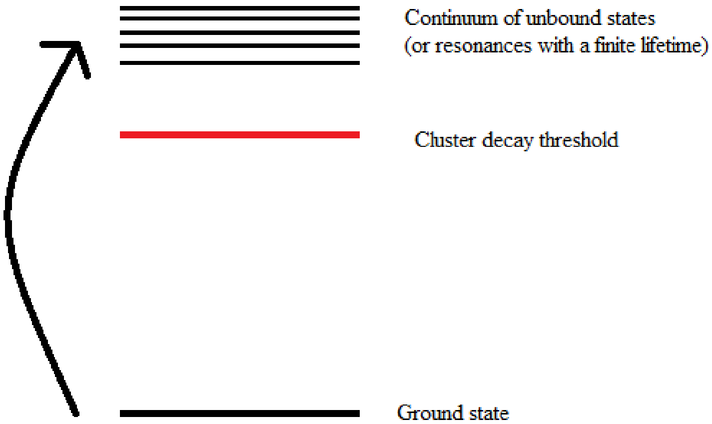

Figure 2.13: A simplified schematic of the excited states in a nucleus.

2.9 Accessing the ground state - Wave-function Overlap

Historically, low energy experiments investigating clustering have inelastically excited nuclei above their cluster decay threshold and observed the subsequent decay. This method is useful in parametrising clustering in excited states as well as identifying the threshold itself. While this does not allow a direct examination of ground state clustering, it is useful indirectly. Figure 2.13 shows a schematic of the energy levels in a nucleus; the nucleus is excited to an energy level in the continuum of states above the cluster decay threshold, and then cluster decays. This reaction can be repeated with a range of nuclei, for example different isotopes of a given element. The changing cross-sections for this reaction give an indication of how similar the wave-functions of the ground state and the continuum or cluster states are for each isotope. If the wave-functions are more similar the excitation will occur more readily, as less rearrangement of the nucleus is required, as discussed in [34]. Since the nucleus ultimately cluster decays in this reaction, it is clear that the excited state possesses cluster structure to some degree; this property can then be inferred for the ground state [16].

This is by no means a “clean” look at clustering in the ground state. There are numerous other competing reaction channels for each isotope, but it is a zeroth order determination of the structure of the ground state, providing an approximate and comparative measure of the prominence of clustering in the ground state.

2.10 Accessing the ground state - QFS

QFS allows for a more refined examination of clustering in the ground state. Events are selected as shown in Figure 2.14.

The reaction shown in Figure 2.14 is a knockout reaction from the ground state of the beam particle in the centre of mass frame. Here the proton target is assumed to interact with only the alpha cluster in the projectile in a “quasi free” elastic collision. Several details must be noted to demonstrate that it is the ground state being examined. Firstly the incoming beam is unexcited as, barring isomeric states, excited states of nuclei have lifetimes in the picoseconds range [31] and so will have decayed to the ground state in transit between the production and reaction targets (more detail on beam production will follow in Section 3.1). Secondly, QFS asserts that the beam fragments do not participate in the reaction and so cannot have absorbed any energy. Finally the large centre-of-mass opening angle between the recoil proton and the knocked-out alpha particle indicates, by conservation of momentum, that neither particle absorbed energy and became excited. Consequently it must be the ground state from which the alpha particle is knocked-out.

This method exploits an additional advantage of QFS; since a kinematically complete measurement is made, an extremely low background can be achieved [32]. This is possible because in the events of interest, the recoiling target and the knockout particle are coplanar (as a consequence of momentum conservation), whereas background events will have a random distribution of relative angles and so are unlikely to be coplanar.

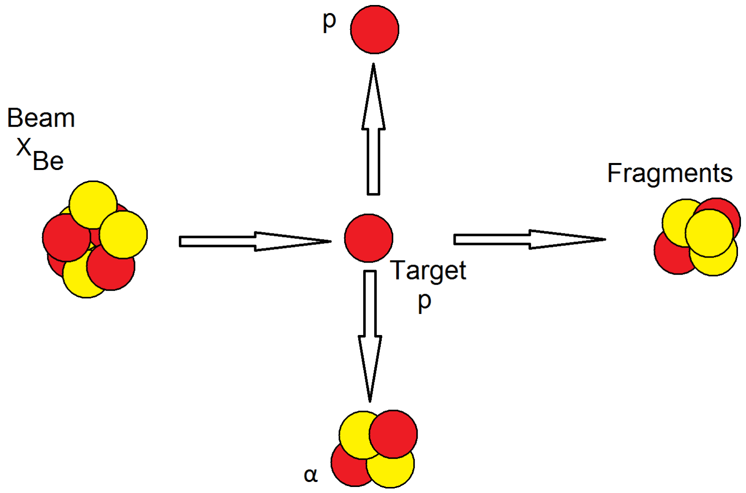

Figure 2.14: A schematic of the QFS knockout reaction in the centre of mass frame.

3 Experimental Details

This chapter describes the facilities and equipment used to conduct the S393 experiment, which was run on the R^{3}B setup at the GSI Helmholtz Centre for Heavy Ion Research in Darmstadt, Germany, during the period August to September 2010.

A variety of beams and targets were used, as the experiment had many physics objectives. In the case of this thesis, the reaction of interest was alpha knockout on proton and carbon targets, for example p(^{10}Be, pα)^{6}He; this alpha knockout was analysed with a variety of neutron rich light nuclei beams. In place of the desired proton target, a polyethylene target ($[C_2H_4]_n$) was used, with separate data taken using a pure carbon target to enable correction for the carbon present in the polyethylene target. Nevertheless, the measurements made from knockout on the pure carbon target are valuable in their own right.

A large number of detectors were employed in the S393 experiment; Figure 3.1 shows an overview of the experimental setup.

The target chamber was evacuated; however the majority of the setup was not held at vacuum. Consequently there was an increase in the energy spread of the beam due to

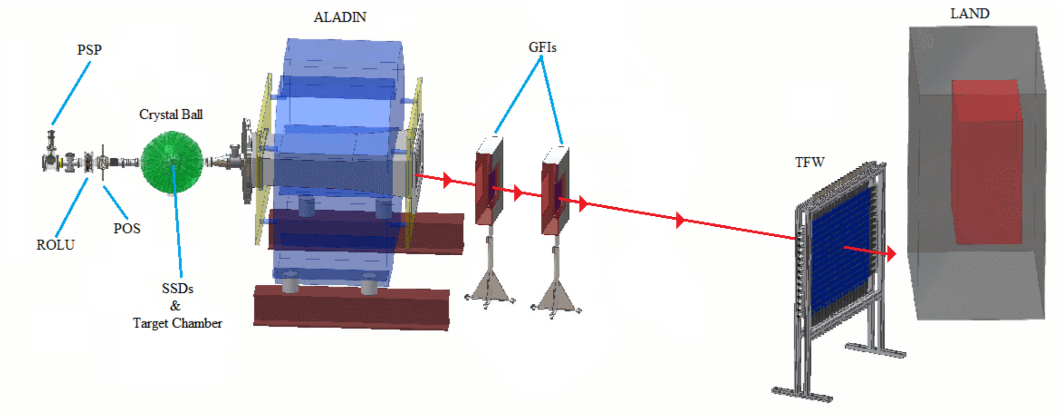

Figure 3.1: The setup for the S393 experiment, adapted from [41]; detectors not directly relevant to the work of this thesis have been omitted.

the statistical process of energy loss of charged particles in a medium; this is known as straggling. This was not ideal, but in the energy regime of the experiment, the increased spread in beam energy was tolerable. The detectors can be divided into three groups: incoming-beam, target area and outgoing-fragment i.e. after the ALADIN magnet.

First the methods of beam production will be discussed. Subsequently, the operation of the detectors used in the analysis will be described.

3.1 Beam Production

Radioactive beams were created using the fragmentation method. An overview of the equipment at GSI that was used in this process is shown in Figure 3.2; the following describes the acceleration and beam production in more detail.

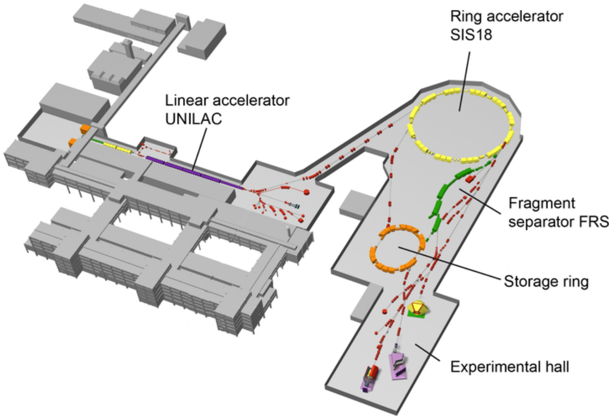

Figure 3.2: A schematic of the beam production at GSI, adapted from [37].

3.1.1 Ion Source

Beam production began at the ion source. An Electron Cyclotron Resonance (ECR) source was used, which operates as follows. A vapour of the required isotope is injected into the ECR region, then ionised to form a plasma by heating within the ECR - the frequency is chosen to resonate the electrons and thus heat through collisions. The plasma is confined by a magnetic trap consisting of an axial field generated by a solenoid and a radial field generated by a hexapol magnet. The magnetic fields are arranged such that the trap has a gap which allows positive ions from the plasma to be extracted and then injected into the accelerator.

3.1.2 Universal Linear Accelerator (UNILAC)

The ions injected from the ECR source were accelerated by a linear accelerator (UNILAC) up to energies of 11.4 MeV per nucleon. The principle of operation of a linear accelerator can be most easily understood schematically. Figure 3.3 shows how a drift tube linear accelerator accelerates charged particles by applying an oscillating RF power supply to hollow tubes which the particles pass through. Between tubes the particle is accelerated by the potential difference across the gap. While inside a tube, there

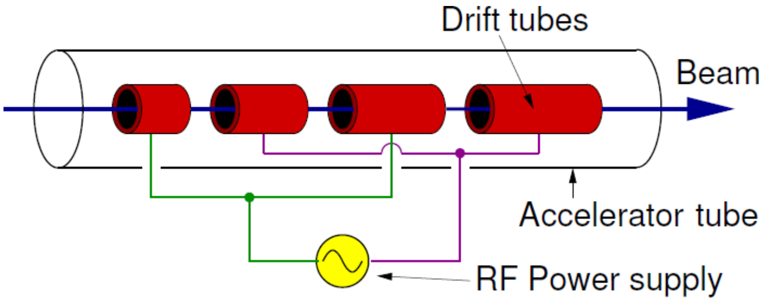

Figure 3.3: A schematic explanation of the operation of a drift tube accelerator, from [38].

is no effective field because the tube acts as a Faraday cage; by the time the particle emerges from the other end of the tube, the oscillating power supply has switched the polarities of the tubes and so another stage of acceleration occurs. The tubes must be made longer towards the target end of the path, as the particles are moving faster.

A disadvantage of this design is that the tube lengths are tuned to a given mass to charge ratio. To accelerate a variety of particles using the same linear accelerator, a different design such as a split loop resonator must be used. Briefly, a split loop resonator operates in same way as described above, but all tubes are the same length and grouped into pairs. The phase of the power supply is managed independently for each pair; this allows the accelerator to be tuned for a range of mass to charge ratios. UNILAC was of the split loop resonator design.

3.1.3 Heavy Ion Synchrotron (SIS18)

The beam from UNILAC fed into the Heavy Ion Synchrotron (SIS18), which provided further acceleration. The available acceleration from SIS18 was dependent on the specific isotope, for example uranium could be accelerated to 50-1000 MeV per nucleon, neon to 50-2000 MeV per nucleon and protons up to 4.5 GeV [39]. In the case of the S393 experiment, the primary beam was ^{40}Ar with an energy of 490 MeV per nucleon. A synchrotron operates by accelerating particles along a path of constant radius, over many rotations; the beam is accelerated with every rotation and extracted when it reaches the desired energy. Separate elements are used to bend, focus and accelerate the beam. After SIS18, the beam was pulsed, as the operation of a synchrotron leads to a pulsed beam structure.

3.1.4 Fragment Recoil Separator (FRS)

After extraction from SIS18, the beam was incident on a target called the production target, in the case of S393 this production target was ^{9}Be. This fragmented the beam to produce a variety of isotopes with approximately the same energy per nucleon as the primary beam.

At this point the Fragment Recoil Separator was used to select the desired isotopes. Fragment separators typically operate using two dipole magnets with an achromatic degrader between them. The first dipole selects for desired energy and mass to charge ratio. The achromatic degrader then reduces the remaining particles energy - this reduction will be different for every isotope, this is explained in more detail during the discussion of Equation 3.5, in Section 3.3.2. The second dipole is then used to select for a given energy, which will eliminate the unwanted isotopes. This process is shown in Figure 3.4. The FRS could achieve beam purities of 90-95%. However, for S393 mixed beams were intentionally produced and isotope selection was made using detectors upstream of the target, as discussed later.

A dipole magnet can be used to select by mass to charge ratio. The force exerted on a charged particle moving through a magnetic field is:

$$\underline{F} = q\left(\underline{B} \times \underline{v}\right) \tag{3.1}$$

where $\underline{F}$ is force, q is charge, $\underline{B}$ is magnetic field strength and $\underline{v}$ is particle velocity.

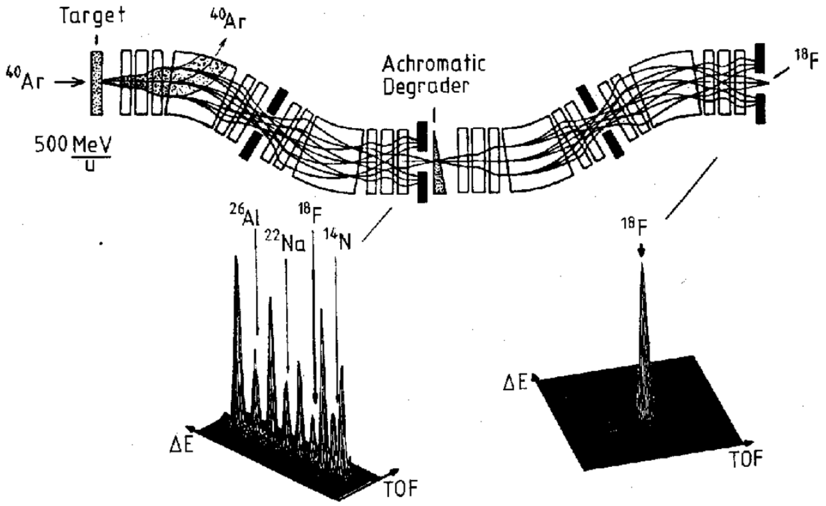

Figure 3.4: A schematic of the GSI FRS, selecting ^{18}F*, from [40]. The upper diagram shows the path, from the primary beam of* ^{40}Ar *hitting the production target, through the dipole magnets and the degrader, up until the desired isotope has been selected. The lower graphs represent which isotopes are present at the indicated points along this beamline.*

Fleming's left-hand rule can be employed to demonstrate that the applied force will always be perpendicular to direction of motion. Consequently, while the charged particle is travelling through the magnetic field it will follow the equation of circular motion:

$$F = \frac{mv^2}{r} \tag{3.2}$$

where m is mass, and r is the radius of curvature. Equations 3.1 and 3.2 can be combined to show that the radius of curvature for a given magnetic field and velocity is directly proportional to the mass to charge ratio of the particle:

$$r = \frac{1}{B} v \frac{m}{q} \tag{3.3}$$

The angle at which a charged particle emerges from a dipole magnet is therefore dependent on its velocity and mass to charge ratio; if the velocity of a particle is known, then a dipole of given magnetic field strength can be used to select particles by mass to charge ratio.

3.1.5 Storage Ring

After the FRS there was an option to direct the beam into another synchrotron called the Storage Ring. The Storage Ring was not intended to provide further acceleration, but instead to apply “cooling” methods to reduce the energy spread of the beam and to measure the in flight properties of novel isotopes [37]. In the case of the S393 experiment the Storage Ring was not used so the beam passed directly from the FRS to the experimental hall.

3.1.6 Final Beam

Figure 3.5 gives an example of the beam rates for the different isotopes in one production run; note that the relative rates are a result of the chosen optimisation of the FRS, other runs were optimised for different mass to charge ratios and so changed the relative rates and isotopes present.

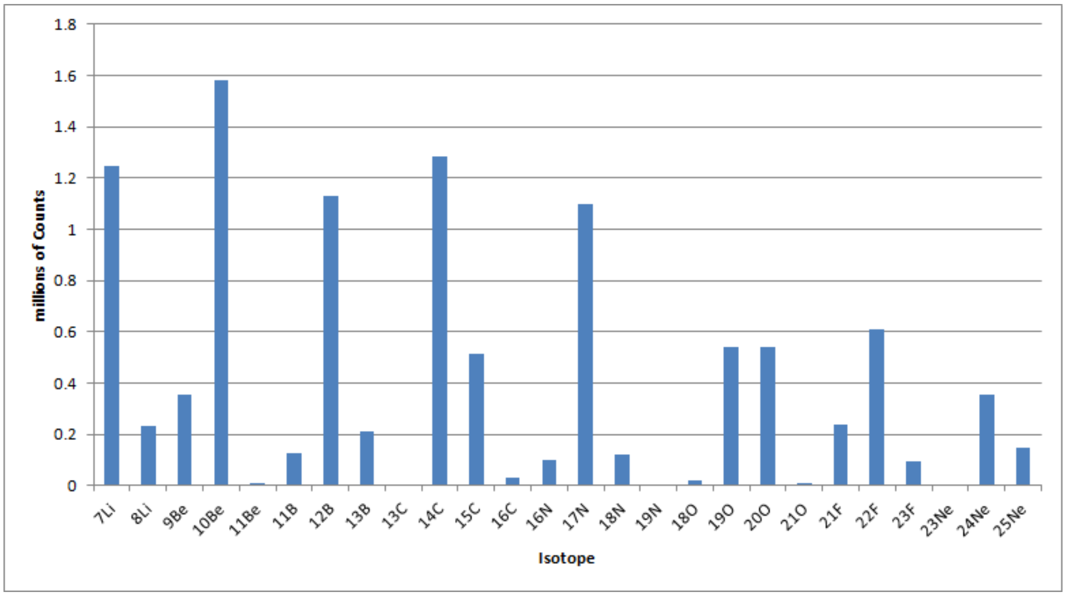

Figure 3.5: A graph showing the available counts of each isotope present in production run 453.

3.2 Detector Theory

The function of a detector is to produce a useful signal from incident radiation, such that the details (for example charge, energy or position) of that radiation can be determined.

Most of the detectors that are described in the following section are based around scintillators. When a gamma-ray is incident on a scintillator, energy can be transferred to the scintillator material by a variety of mechanisms; these mechanisms occur in a proportion dependant on the energy of the incident gamma-ray.

Figure 3.6 shows the cross sections as a function of energy for photoelectric absorption, Compton scattering and pair production: the three main methods of a gamma-ray interacting with matter. Strictly, what is shown is the mass attenuation coefficient - the bulk property of the material, in this case aluminium, to attenuate gamma-rays. This value for the bulk material arises from the interaction cross sections for individual atomic centres and can be related to them by:

$$\sigma = \frac{\mu}{\rho} * m \tag{3.4}$$

where σ is the cross section, $\frac{\mu}{\rho}$ is the mass attenuation coefficient and m is the mass per atomic centre [60]. Figure 3.6 is useful in showing the comparative energy dependence of the interaction processes and also can be used to give an estimate of typical cross sections, for example a 1 MeV gamma ray has a mass attenuation coefficient of around 0.07 cm^2/g, using Equation 3.4 this can be converted to a cross section of 3.14 barns for each atomic centre.

Figure 3.7 is a schematic representation of the interaction processes taking place in a detector medium.

In each case a fast electron is produced which in turn loses energy to atomic electrons. In the case of the positron created during pair production; the positron will

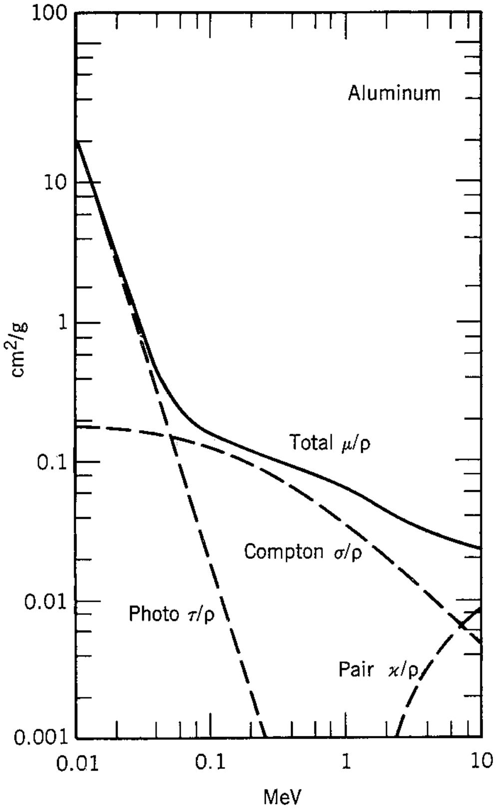

Figure 3.6: The energy dependence of the gamma-ray interaction processes in aluminium showing the variation of photoelectric absorption, Compton scattering and pair production, from [42].

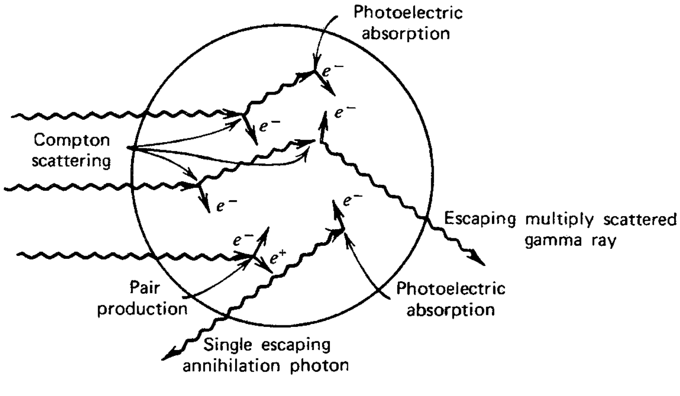

Figure 3.7: A schematic diagram of gamma-rays interacting in a detector, from [43].

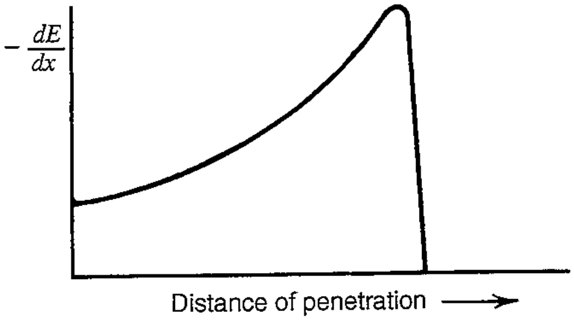

Figure 3.8: The rate of energy loss for a heavy charged particle in matter, adapted from [44].

lose energy, again to atomic electrons, as it slows down before finally annihilating with an atomic electron, producing further gamma-rays which may go on to interact as described above. In an infinite detector medium, all energy would eventually be deposited; however as Figure 3.7 shows, occasional escapes can occur. These escapes can be either the Compton scattered gamma-ray or the 511 keV annihilation gamma-rays.

Heavy charged particles passing through a scintillator lose almost all their energy by Coulomb scattering with atomic electrons. Because each interaction transfers only a small amount of energy, a huge number of interactions must occur and so the loss of energy becomes statistical but with negligible uncertainty and hence a predictable process. Figure 3.8 shows a graph of the energy deposition as a function of range for a charged particle in matter, this is known as the Bragg curve; the pronounced peak is known as the Bragg peak and occurs because the overall interaction cross section increases as the particle's energy decreases.

In the case of both gamma-rays and heavy charged particles travelling through the scintillator, the interactions ultimately result in the excitation of many atomic electrons. Freed electrons may go on to collide with and excite further atomic electrons, or may simply de-excite producing radiation. This light will then travel to a photomultiplier tube (PMT), where the signal will be amplified. For this reason it is necessary that a scintillator is transparent to the wavelength of the light characteristic to the energy difference between the valence and conduction bands. Some scintillators are not transparent to photons of the frequency produced by their characteristic de-excitation. The probability of this production, and therefore the efficiency of the scintillator, can be improved by a process called activation; for example a small thallium impurity can be introduced into the crystal lattice of the scintillator sodium iodide. This has the effect of creating discrete intermediate electron energy levels within the region between the valence and conduction band, consequently an excited electron may de-excite by stages, and production of photons to which the scintillator is transparent is more likely. In addition, electron holes produced by excitation drift around the lattice stopping by becoming trapped at the activator impurities, because ionisation there is more energetically favourable; as a result the majority of de-excitation happens at impurity sites [45]. This process takes time giving the detector a poor time resolution when compared to, for example, plastic scintillators which typically do not possess the band gap structure requiring this approach.

The output of the PMT will undergo further processing in the data acquisition electronics, before being digitally recorded. Scintillator detectors do not typically have good energy resolution, but are cheap, robust and easy to manufacture into different shapes and sizes, and hence are widely used.

Another type of detector is the semi-conductor detector. A basic semi-conductor detector is constructed using two adjacent doped semi-conductors materials (such as silicon). One is doped positively and the other negatively. Their interface is called a junction. The migration of electrons to fill the holes (in the positively doped material) creates a depletion zone on the border between the two materials; as the extra electrons move to fill the extra electron holes. The depletion zone can be expanded by applying a voltage across the junction, forcing more electrons to fill holes. When ionising radiation is incident on the depletion zone, the electrons are promoted from the valence band to the conduction band and current flows through the junction to re-fill the holes. The accumulated charge is measured and the average energy required to excite an electron from the valence band to the conduction band is known (for example approximately 3.6 eV for silicon at 300 K [46]), so the energy of the ionising radiation can be calculated. By dividing the opposing faces of the detector into orthogonal strips and reading a signal from each strip individually, it is also possible to extract the position of the incident particle; the strips are created by segmenting the electrodes evaporated onto each face. Semi-conductor detectors are more expensive and fragile when compared to scintillator detectors, however they offer better energy resolution and better time resolution than scintillators requiring doping, though worse time resolution than plastic scintillators.

3.3 Incoming-beam Detectors

3.3.1 Position Detector (POS)

The POS detector was used as both a start and end point for time of flight measurements. The design was a 5.5 cm by 5.5 cm plastic scintillator detector with a PMT on each side, as shown in Figure 3.9. The name "Position Detector" referred to a previous usage of the detector, that is, to measure beam position as well as timing; this is why the scintillator had a PMT on each side. As an end point the POS completed the time of flight measurement started in the FRS, which allowed the beam constituents to be identified (see discussion in 3.3.2). As a start detector, it began a time of flight measurement which ended at the time of flight wall, helping to identify the reaction products.

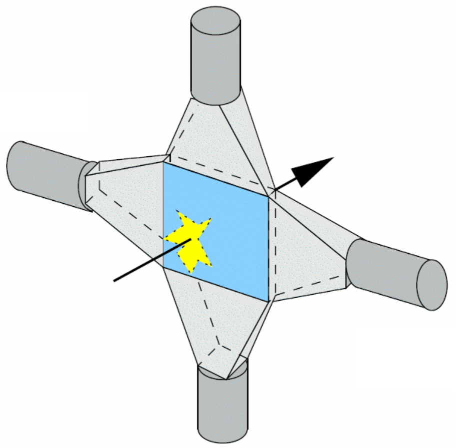

Figure 3.9: A schematic of the POS detector. The central blue square is the scintillator and the cylindrical attachments are the photo-multiplier tubes. Adapted from [47]

3.3.2 Position Sensitive silicon Pin diode Detector (PSP)

The PSP detector was a 300 μm thick silicon detector with an active area of 4.5 cm by 4.5 cm [49]. It was used to make an energy loss measurement which contributed to particle identification by determining the charge of a particle using the Bethe-Bloch formula:

$$-\frac{dE}{dx} = \frac{4\pi}{m_e c^2}\frac{nZ^2}{\beta^2}\left(\frac{e^2}{4\pi\epsilon_0}\right)^2\left[\ln\left(\frac{2m_e c^2\beta^2}{I\left(1-\beta^2\right)}\right)-\beta^2\right] \tag{3.5}$$

where $\frac{dE}{dx}$ is the rate of energy loss (dE) distance travelled (dx), m_e is the electron mass, c is the speed of light, n is the electron density of the material, Z is the particle charge, β is particle velocity divided by c, e is the electron charge and I is the mean ionization potential of the material [48]. For a given detector, most of these variables are known which means that a particle of given energy and charge has a characteristic energy loss.

As discussed in Section 3.3.1, the POS detector contributed a time of flight measurement to particle identification. As the energy of the particles was fixed by the acceleration process and the distance between the detectors used for the time of flight measurements was known, the time of flight could be used to calculate the mass of incident particles. Similarly, using the known energy the charge of the particle could

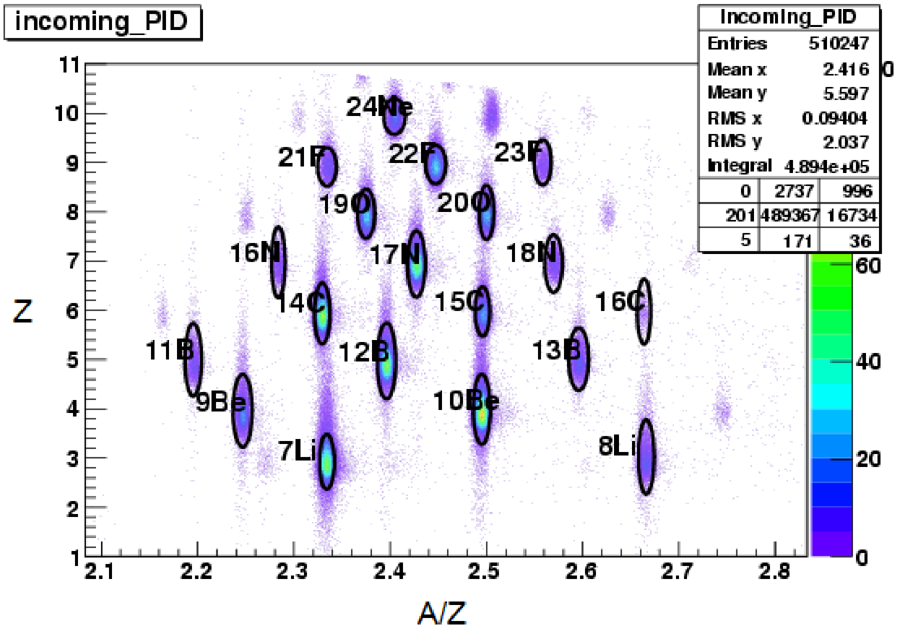

Figure 3.10: A typical calibrated example of particle identification from online analysis of the S393 experiment. The vertical axis shows charge, and the horizontal axis shows the mass to charge ratio. This type of graph was regularly produced during runs to assess the proportions of the isotopes in the beam [57].

be determined as described above.

These two calculations were used to make a particle identification graph such as Figure 3.10. This was vital to determine the constituents of the beam and the relative intensities of these contributions. Software gating was then used to select the desired projectile.

3.3.3 Rechts Oben Links Unten Detector (ROLU)

The ROLU detector consisted of four plastic scintillator detectors positioned normal to the direction of the beam. The scintillators were arranged in two pairs, one forming a horizontal gap and the other a vertical gap, as shown in Figure 3.11.

ROLU was used as an active filter to define a beam spot size by vetoing events that hit any of the four scintillators. The scintillator pairs could be opened or closed to

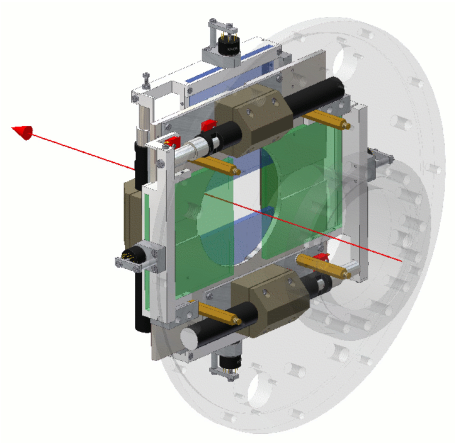

Figure 3.11: A CAD diagram of the ROLU detector from [50].

change the effective beam spot size. This method was more suitable for high energy particles than using passive slits to define the beam, as high energy particles could punch through such slits, or scatter significantly.

3.4 Target Area Detectors

Figure 3.12 shows the target wheel, mounted together with the Silicon Strip Detectors (SSDs). The target wheel contained nine slots for targets; the target in use was changed by rotating the wheel, which could be done remotely. This setup was located inside the target chamber, which was surrounded by the Crystal Ball array.

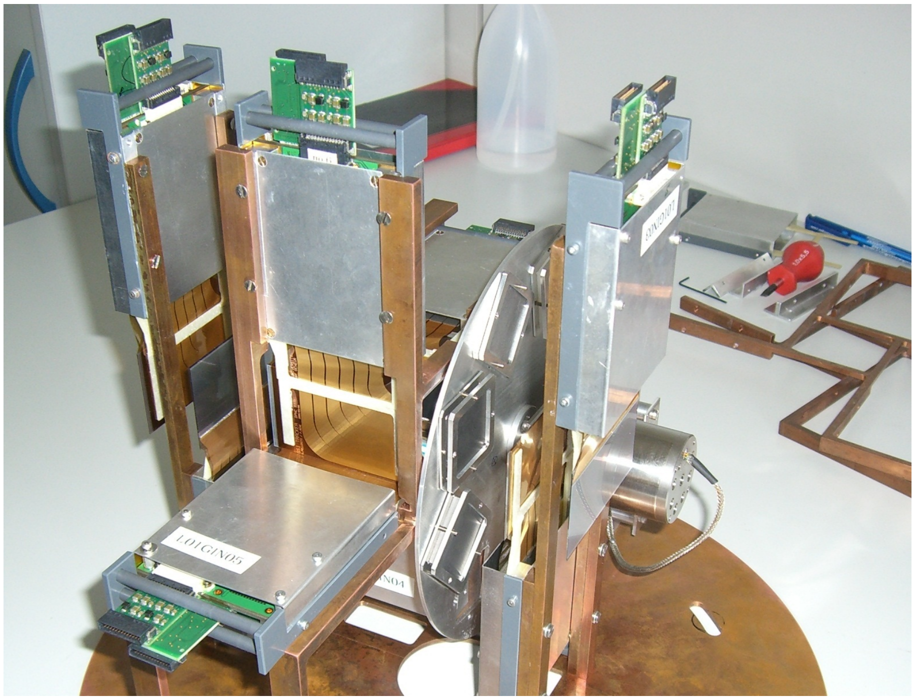

Figure 3.12: A photo of the arrangement of the target wheel and Silicon Strip detectors which were located inside the target chamber, from [51].

3.4.1 Crystal Ball

The Crystal Ball was a spherical array of 162 NaI scintillator detectors surrounding the target chamber. The array covered approximately 4π solid angle, with gaps to allow for the beamline. It detected both gamma-rays and protons with high efficiency (for example 96% for 1.3 MeV gamma-rays). Detected gamma-rays could be used to determine the energies of excited nuclear states which had decayed via gamma-ray emission. Protons of appropriate energy range deposited all of their (remaining) energy in the Crystal Ball, allowing a total energy measurement. Only crystals at more forward angles had a dual gain read out allowing for the measurement of charged particles. Figure 3.13 shows the Crystal Ball separated to allow access to the target and silicon detectors (see Section 3.4.2) [52].

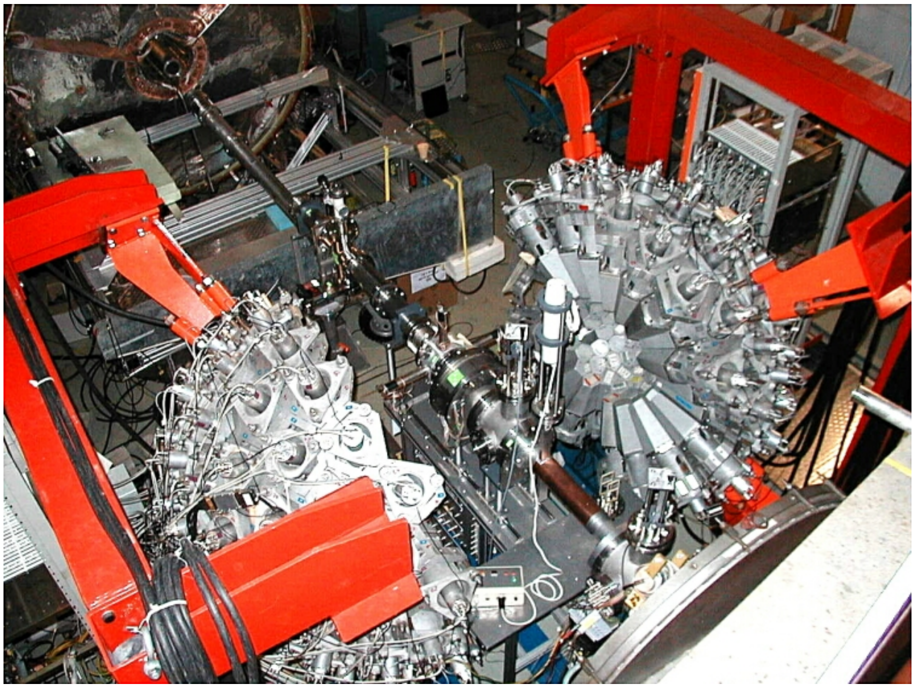

Figure 3.13: The crystal ball, separated about the beamline. The internal surface can be seen, which makes clear the large angular coverage of the detector. Image taken from [53].

3.4.2 Silicon Strip Detectors (SSDs)

The SSDs were double sided silicon strip semi-conductor detectors measuring 72 mm by 40 mm and 0.3 mm thick. The s-side had vertical strips with an implantation pitch of 27.5 μm but a read out pitch of 110 μm (i.e. every fourth strip was read out). Over the 72 mm this gave 640 readout channels. The k-side had vertical strips with an implantation and read out pitch of 104 μm. Over the 40 mm this gave 384 read out channels.

Figure 3.14 shows the arrangement of the silicon detectors relative to the beam. The four out of beam detectors formed a box downstream of the target, and so were called the "box-detectors". The four in-beam detectors were referred to as either upstream or downstream of the target. It is worth noting that the beam intensities for radioactive beams were comparatively low, so the in-beam detectors were not significantly damaged by exposure. The SSD detectors were primarily used to determine emission angles for charged particles leaving the target area.

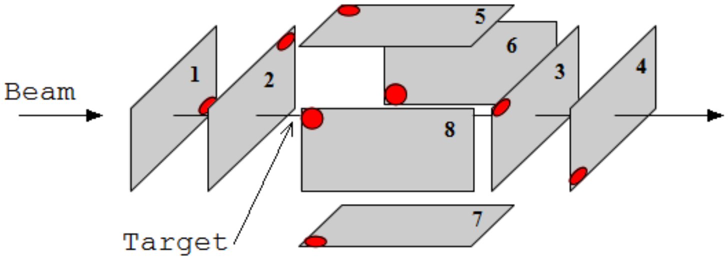

Figure 3.14: A schematic diagram of the arrangement of the silicon detectors, from [54]. The red spot on each detector shows a common corner which defines the orientation.

3.5 ALADIN (A LArge DIpole magNet)

ALADIN was positioned approximately 1.5 m downstream of the target. As charged particles passed through its magnetic field, they were bent off the beam axis, towards the outgoing-fragment detectors, which are discussed in the following section. The interior of ALADIN was filled with helium rather than air, this served to reduce energy straggling as a result of collisions; it was particularly important to keep straggling to a minimum within ALADIN to aid particle tracking, which is explained in Section 5.1.

Charged particles passing through ALADIN were bent in proportion to their magnetic rigidity which is dependent on their energy and mass to charge ratio. For particles of known mass to charge ratio, the resulting spread allowed for a measurement of the momentum distribution. For example, if a neutron had been knocked-out of the beam particle, the outgoing fragment is of known mass and charge and the spread will result from the momentum change caused by the neutron knockout. In the case of knockout in the QFS regime where the beam fragments are undisturbed, the spread allows for identification of these fragments, in much the same way as described for the FRS isotope selection in Section 3.1.4. Figure 3.15 shows ALADIN in situ. Also visible are the

GFI detectors, discussed below.

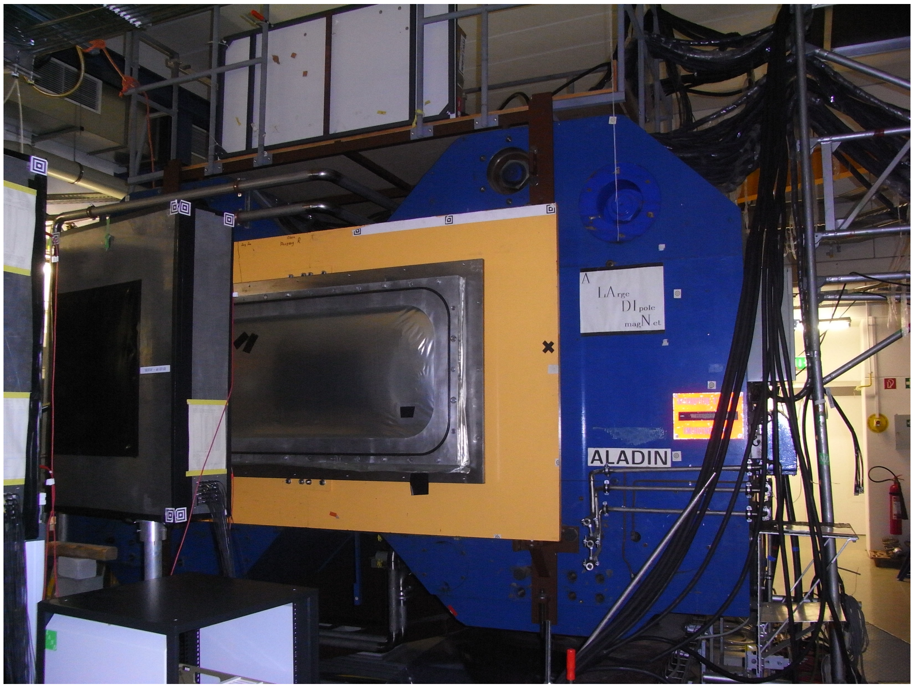

Figure 3.15: ALADIN and to the left, the GFI detectors.

3.6 Outgoing-fragment Detectors

3.6.1 Grosser FIber detektors (GFIs)

The GFIs were scintillating fibre detectors with a total effective active area of roughly 500 mm by 500 mm. They consisted of 475 vertical fibres, giving a particle's horizontal position on the detector to a resolution of about 1 mm for Lithium and decreasing with increasing particle charge. Each fibre had one end connected to a position sensitive PMT, and the other end connected to a normal PMT for timing as shown in Figure 3.16. The GFIs were placed at an angle of roughly 15° from the beamline; they aided in particle identification by giving a horizontal position showing the extent to which a particle has been bent by ALADIN. The detection efficiency also varied with particle charge, and is stated as 89% for $Z \geq 3$ particles, rising to almost 100% for $Z \geq 10$

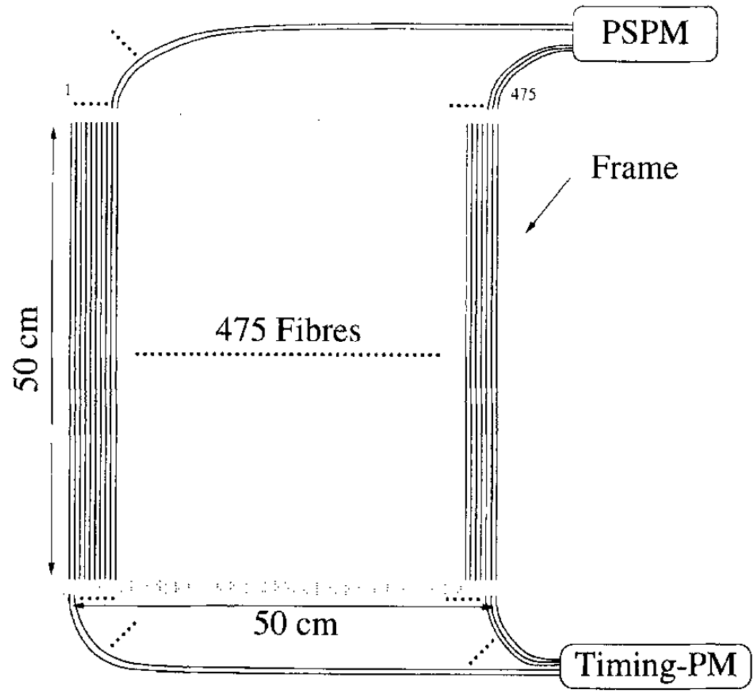

Figure 3.16: A schematic diagram of the GFI fibres and photo-multiplier tubes, from [55].

particles [55]. This efficiency variation existed because the deposited energy was proportional to the square of the nuclear charge, as indicated by Equation 3.5. Unfortunately, as discussed in the Analysis chapter, the efficiency dropped off more significantly than stated for lower charges.

3.6.2 Time of Flight Wall (TFW)

The TFW consisted of 18 vertical and 14 horizontal plastic scintillator paddles, each with a PMT at both ends, as shown in Figure 3.17. The vertical paddles were 1470 mm in length and the horizontal paddles were 1890 mm; for both the width was 100 mm and the depth 5 mm [56].

The TFW provided the last measurement along the trajectory of charged particles. The energy deposited was used to determine the charge of particles, in much the same way as discussed for the incoming-beam detectors. However, it was not possible to

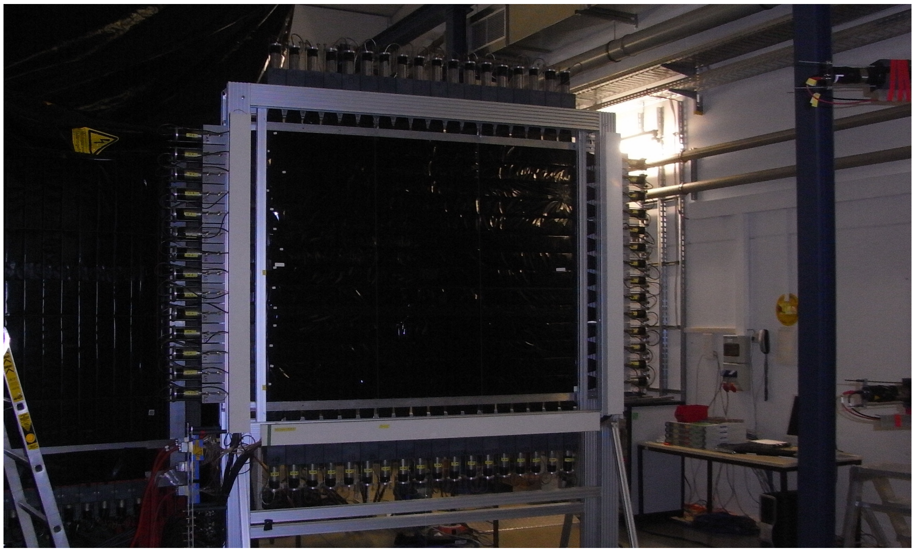

Figure 3.17: A photo of the TFW. To the left, the edge of LAND can be seen.

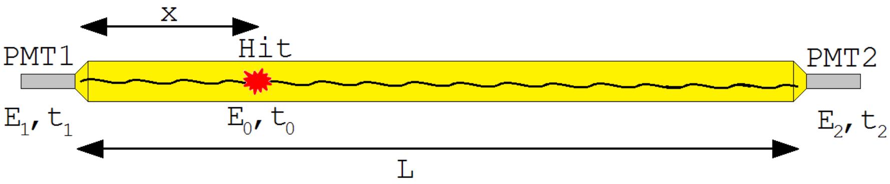

Figure 3.18: A schematic of event reconstruction for the TFW, adapted from [58].

determine the mass of particles using timing alone because the path of a particle through ALADIN was not known. The solution to this issue is discussed in detail in the Analysis chapter.

Figure 3.18 shows a hit in a single paddle of the TFW, and how this hit is measured in the two PMTs. From these signals the energy, position and timing of the hit can be calculated [59].

The time of a hit at either PMT is the true time of the hit, plus travel time to the PMT:

$$t_1 = t_0 + \frac{x}{v} \tag{3.6}$$

$$t_2 = t_0 + \frac{L-x}{v} \tag{3.7}$$

where v is the speed of light in the detector medium. Combining these formulae and solving for t_0 gives:

$$t_0 = \frac{t_1 + t_2}{2} - \frac{L}{2v} \propto \frac{t_1 + t_2}{2} \tag{3.8}$$

since $\frac{L}{2v}$ is a constant. Similarly the energy response of either PMT is a simple function of the true energy, in this case multiplied by the exponential of the distance to the PMT:

$$E_1 = E_0 e^{-\lambda x} \tag{3.9}$$

$$E_2 = E_0 e^{-\lambda(L-x)} \tag{3.10}$$

where λ is the attenuation co-efficient. Multiplying these formulae and solving for E_0 gives:

$$E_0 = \sqrt{\frac{E_1 E_2}{e^{-\lambda L}}} \tag{3.11}$$

It should be noted that the denominator $e^{-\lambda L}$, is a constant and will be taken care of by gain matching. Note that neither the timing nor the energy have dependence on the position. The position of a hit can be calculated by comparison of the two PMTs timing or energy signals. Combining Equations 3.6 and 3.7 and solving for x gives:

$$x = \frac{v}{2}(t_1 - t_2) + \frac{L}{2} \tag{3.12}$$

To extract position information from the energy signal, Equation 3.9 is divided by Equation 3.10 and the resulting formula is solved for x:

$$x = -\frac{1}{2\lambda}\left(\lambda L - ln\left(\frac{E_1}{E_2}\right)\right) \tag{3.13}$$

The situation of having two methods to calculate the position is useful: in the event that one PMT fails to supply time or energy information, this can still be reconstructed and the event recovered.

3.6.3 Other Detectors

Figure 3.17 also shows LAND (the Large Area Neutron Detector). LAND was directly in line with the beam axis, as any neutrons produced would not be bent by ALADIN. This detector will not be discussed in detail here, as it was not used in the present analysis.

4 Calibrations

This chapter describes the processes of calibrating the detectors of the experimental setup. Not all calibrations detailed below were undertaken as part of the present work, but were instead shared by colleagues performing other analyses of the S393 experiment. These calibrations have been described to give a more thorough understanding of the resulting data. Where possible these calibrations have been attributed; in some cases the online calibration has proven sufficient, for these attribution is not possible.

4.1 Time Calibration

Detectors must be synchronised in time so that the information from all detectors is available for a given event. Further, synchronisation is important in calculating accurate times of flight. A beam of known energy and isotope is used, as this will have a calculable velocity. The positions of the detectors are known to a reasonable accuracy and so the expected time of the hit is known for each detector. The discrepancy between the expected time and the actual time can then be used to synchronise later events, taking into account any delays caused by the acquisition electronics and the intrinsic time response of the individual detectors. The beam-rate is low compared to the time resolution of the detector setup, such that there is no issue of confusing hits from an event with hits from subsequent or prior events.

4.2 SSDs

The SSDs require a complicated calibration with multiple steps that need to be performed in order. The position calibration however is not especially complex as the relationship between strip number and position on the detector face is fixed by design. The key spatial calibration is the alignment and position of the SSDs within the total experimental setup. This was performed in two stages; firstly an initial estimate was made based on physical measurements and photogrammetric methods. Secondly the precise alignment was inferred during the refinement of the tracking process, this is discussed in more detail in Section 5.1.

4.2.1 Pixel Runs

Many of the calibration procedures for the SSDs and other detectors make use of specific calibration runs called "Pixel" runs. Pixel runs have a defocused beam, which gives a broad illumination of the detectors, as compared to the typically narrow beam spot used for production runs. It should be noted that in the S393 experiment the Pixel runs were not of good quality as they did not give this broad illumination. As such, Pixel runs were sometimes replaced by production runs, or multiple production runs with differing beam spot locations in order to illuminate more of the detector.

4.2.2 Pedestal Correction

Devices called Charge to Digital Converters (QDCs) convert the signal read out from an individual strip into a digital value. This is accomplished by allowing the signal to charge an internal capacitor, then measuring the charge accumulated over the duration of the signal. Because the QDC also supplies a small residual current, a charge will be accumulated even with no signal. This produces an offset in the final strip value. These offsets are called pedestals and are different for each strip on each detector, Figure 4.1 shows an example.

The size of the pedestals can be calculated by observing the measured values when no other detectors have been triggered. These values can then be subtracted to remove the pedestal offset.

The pedestals can drift during the course of an experiment, so the offsets are cal-

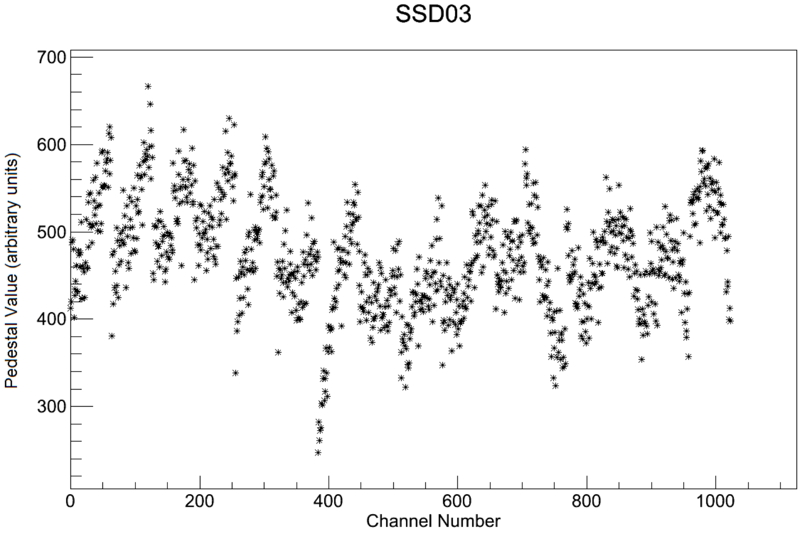

Figure 4.1: A graph showing the pedestal values for SSD 3.

culated at several points in time. If the difference was minor, one set of values would be sufficient; otherwise a time-dependent calibration was necessary. In the case of the S393 experiment a time dependent calibration was required. This requirement is demonstrated by Figure 4.2, which shows a comparison of the pedestals found for a run approximately in the middle of the beam-time, and a run towards the end of the beam-time. The variation ranges from around 0.5% to 1.5%.

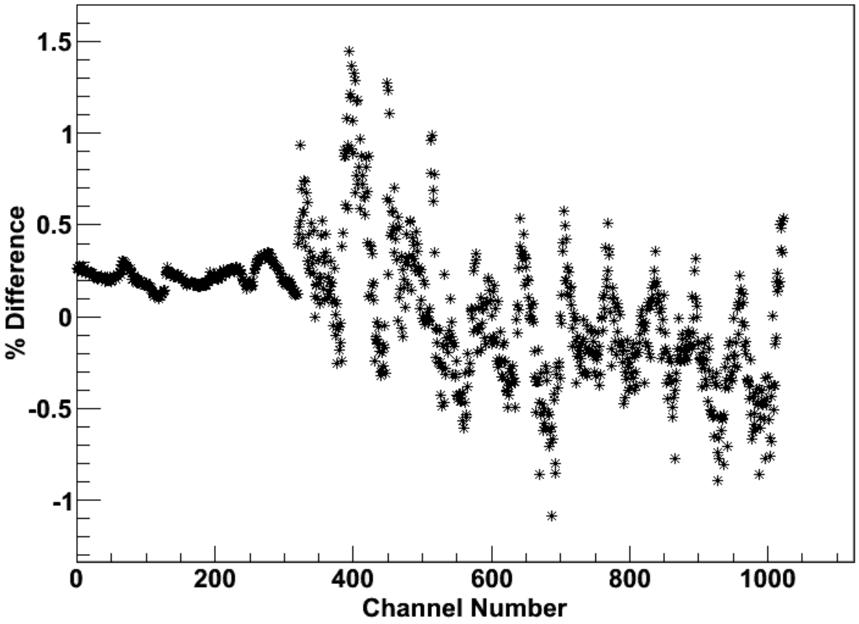

Figure 4.2: A comparison of the pedestals found for SSD 1 during a mid beam-time run and a run towards the end of the beam-time.

4.2.3 VA Chip Gain Synchronisation

The pre-amplification for each SSD is performed by chips called “VA chips”. Each SSD required 16 VA chips as each chip handled 64 channels. As a result, the pre-amplification gain was set in blocks of 64 channels; any difference in these gains had to be corrected for. For the in-beam SSDs this wass accomplished by using the Pixels runs, which deposited a common amount of energy across most of the strips of the detector. This could then be used to account for any differences in gain. Unfortunately no such broad illumination of known energy and isotope was available for the box SSDs. This difficulty in calibrating the box SSDs was also present for later calibration steps.

4.2.4 Dead Strip Identification

For various reasons, such as broken bond wires or broken VA chips, some of the readout strips of the SSDs were unresponsive. These are called dead strips and it was necessary

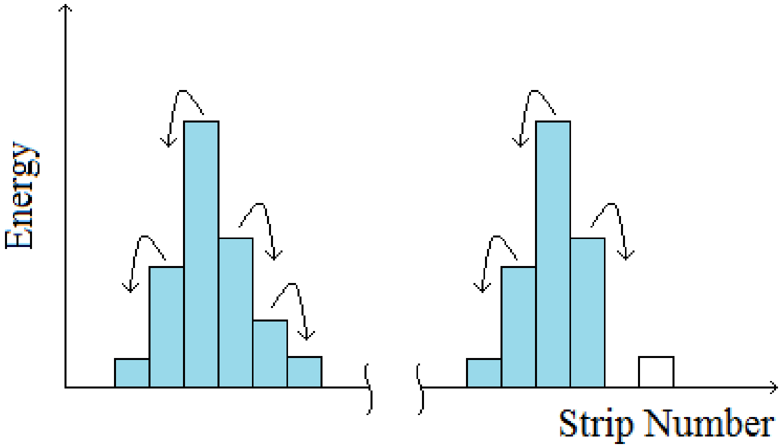

Figure 4.3: A schematic explanation of the importance of dead strip identification in energy summing in the SSDs. On the left, the cluster is correctly summed by stepping from the highest energy strip to all strips of the cluster. On the right, the dead strip causes the summing algorithm to prematurely conclude that the edge of the cluster has been reached. This means that the cluster is incorrectly summed as it is missing the energy of the final strip, as well as the energy that ought to have been reported by the dead strip.

to identify these strips in order to get good data from the SSDs. The energy of a hit is spread over a small number strips; starting at the strip with the highest energy, the total energy is calculated by examining adjacent strips, stopping where there is a strip with negligible energy. So if an unidentified dead strip were to be present, this would result in an incorrect energy measurement, as shown schematically in Figure 4.3.

Dead strips were identified by plotting uncalibrated energy against strip number, as shown in Figure 4.4, and noting the strips which gave a significantly lower energy response than their neighbours.

Once identified the dead strips were noted and therefore accounted for in the energy summation, partially ameliorating the issue of incorrect energies.

This process was easiest and most complete with the broad illumination of the Pixel runs. Consequently, it was not as thorough for the box SSDs, and the quality suffered for all detectors due to the poor Pixel runs.

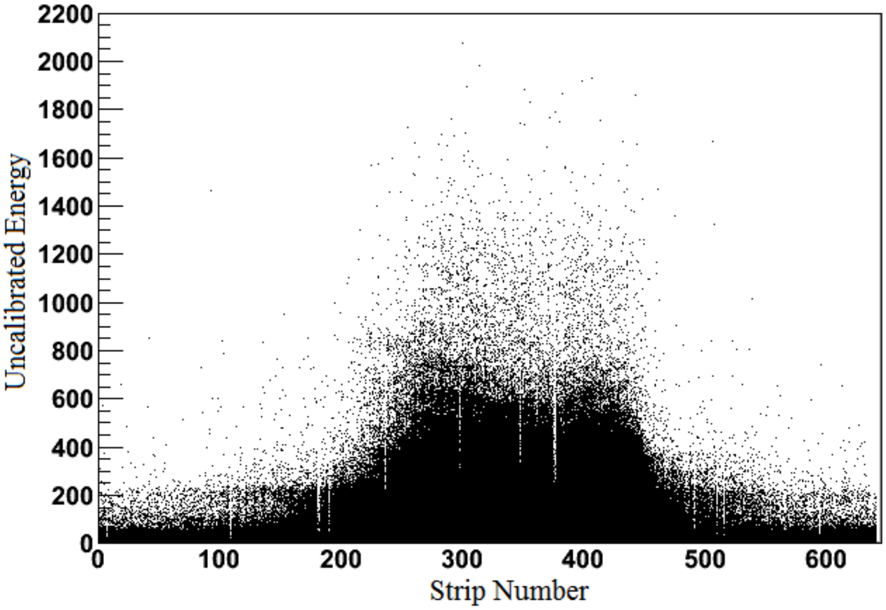

Figure 4.4: A plot of uncalibrated energy against strip number on the SSDs, used to identify dead strips.

4.2.5 Eta Correction

The need for the eta correction results from the difference between the strip pitch and the readout pitch of the SSDs: only every fourth strip was read out. This caused a strong variation in energy depending on the proximity of a hit to a readout strip, as shown in Figure 4.5. The strength of the variation was dependent on the particle's charge, so separate eta corrections had to be made if isotopes differing substantially in charge were investigated. Again this process required a broad illumination such as the Pixel runs, and so was not possible for the box SSDs.

For each side of each detector, eta corrections are made by plotting measured energy against eta-position. Eta-position has the range $0 \leq eta < 1$ and is calculated by comparing the hit position to the readout strips: a value of 0 means the hit passed exactly through the centre of a readout strip, 0.5 means the hit passed equidistant between two neighbouring readout strips. A strong correlation should be observed, as shown in Figure 4.6.

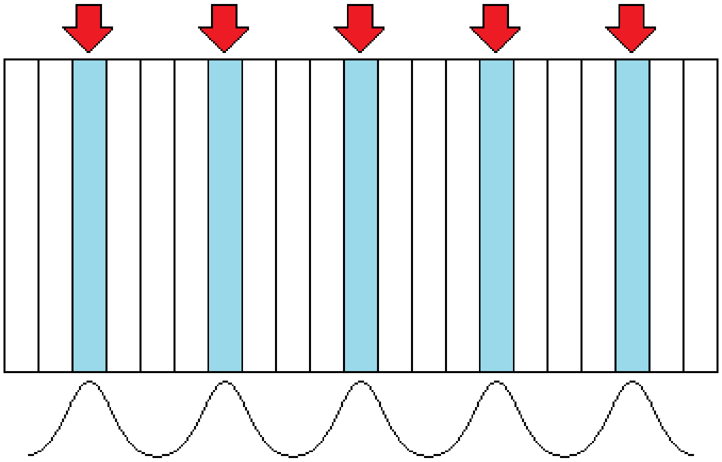

Figure 4.5: A schematic of an SSD showing the energy dependence on proximity to a readout strip. The red arrows indicate the readout strips, and the plot below the detector face is a rough indication of the measured energy for a hit of given energy at that position.

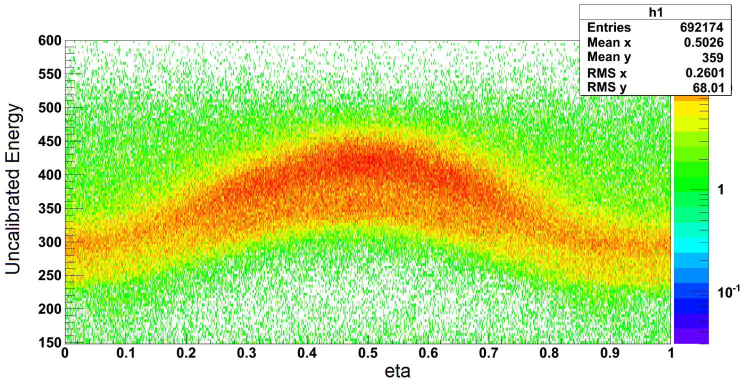

Figure 4.6: A graph showing the eta dependence of the measured energy of the s-side of SSD 2.

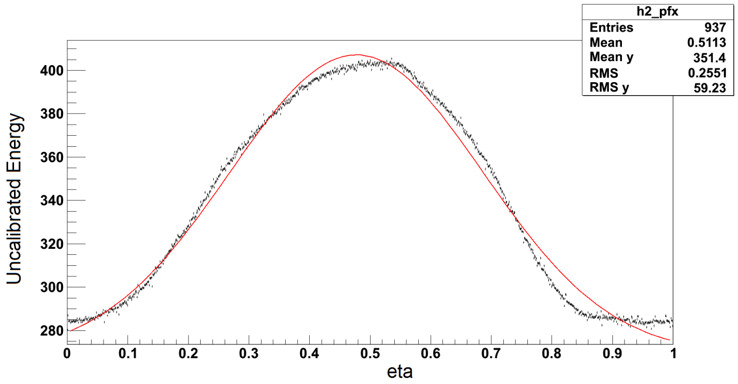

Figure 4.7: A graph showing the profile of the eta dependence of the measured energy of the s-side of SSD 2.

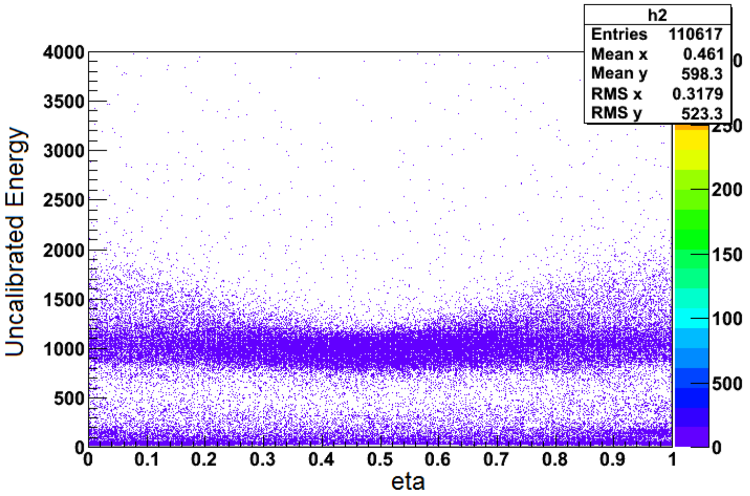

Figure 4.8: A graph showing eta corrected energy for the s-side of SSD 2.

A cut was then made around the region showing the eta dependent behaviour. From this data a profile can be made, comparing the eta-position to the average measured energy. A Gaussian can be fitted to this profile, as shown in Figure 4.7.

This fit was then used to make the eta correction, resulting in the flat profile shown in Figure 4.8.

4.2.6 Gain Matching

The in-beam SSDs were gain matched by comparing the measured energy to a known energy. Since this process needed to be repeated for every strip, the Pixel runs were used so that as many strips as possible were illuminated. To ensure a single incoming energy, a single isotope was selected from the beam. The initial energy of the beam was known from the FRS, and so the energy loss in each detector could be sequentially calculated using Equation 3.5, as discussed in Section 3.3.2. For this calibration, LISE++ was used to calculate the energy loss [64].

The energy response of a given strip should form a Gaussian distribution. This distribution was fitted, and the centroid was compared to the known incoming energy. The gain factor for this strip was the factor required to shift the centroid to the known energy. Figure 4.9 shows a typical graph for one side of an SSD.

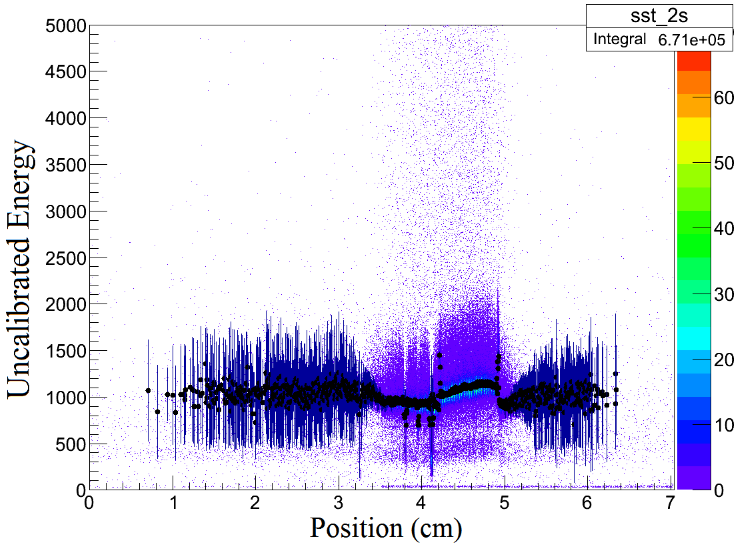

Figure 4.9: A graph showing the gain matching of individual strips of the s-side of SSD 2. Note the large error bars outside of the beam spot.

Outside of the beam spot this method cannot work. As a best approximation, the average value of the fitted strips inside the beam spot, was applied to the unfitted strips

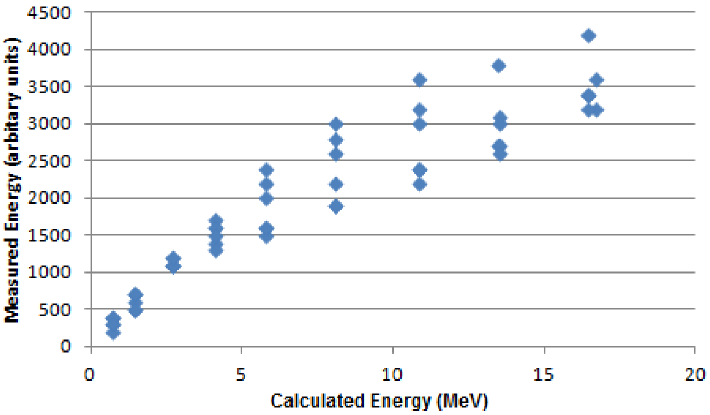

Figure 4.10: A plot of measured energy against "known" energy, calculated from Equation 3.5, in the in-beam SSD detectors.

outside of the beam spot. For the same reason, this method cannot be applied to the box SSDs; the best guess for the s-sides of the box detectors was taken as the average over all s-sides of the in beam detectors, and likewise for the k-sides.

To confirm the linearity of the gain, this process was repeated with different expected energies; in the case of this calibration, this was accomplished by using different isotopes due to a low variety of empty target run energies. Figure 4.10 shows the comparison of measured energy and the calculated energy loss. The relationship is acceptably linear in the lower energy region of the graph, where the focus of this work will take place.

4.2.7 Eta Dependent Position Correction

The discrepancy between strip pitch and readout pitch discussed in Section 4.2.5 can also have an effect on measured position. This appears as regular structures in the position data. Figure 4.11 shows position data before and after a correction script is applied.

In the case of the present work, this effect was not found to be significant, and so the correction script was not applied.

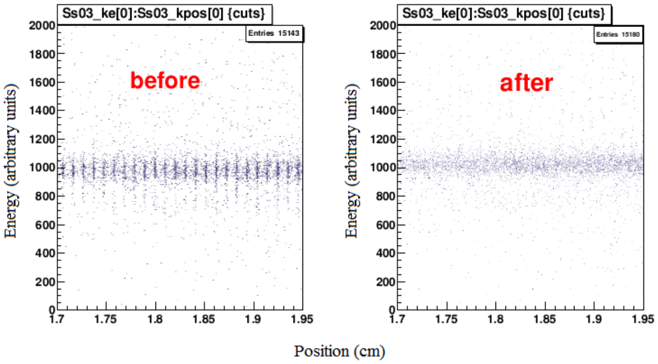

Figure 4.11: Position data for the k-side of SSD 3, showing the eta dependent position effect, from [66].

4.3 PSP Detector

This calibration was generously shared by Marcel Heine.

4.3.1 Position Calibration

The PSP was read out by four contacts, one in each corner. As a consequence the position data was not linearly related to the signal on the contacts. This was corrected using a detector called the Pixel detector, which functioned as an active mask for the PSP. The Pixel detector was a square array of 0.5 mm by 0.5 mm pixels, connected to a single PMT. The Pixel detector was only in place during Pixel runs, and was remotely removed for production runs.

By vetoing events which did not trigger the Pixel detector, the position data on the PSP was made to display how its non-linearity distorts a known geometry, that is the regular geometry of the Pixel Detector. This is shown in Figure 4.12.

The position calibration was the adjustment required to correct the distorted position data to the regular geometry. An example of the corrected data is shown in Figure 4.13.

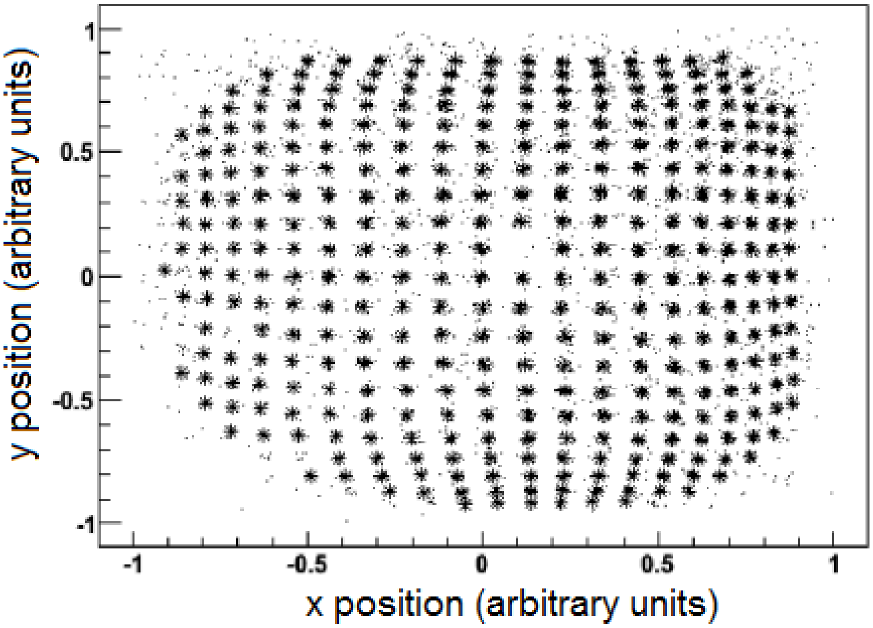

Figure 4.12: Distorted position data on the PSP detector, taken from [61].

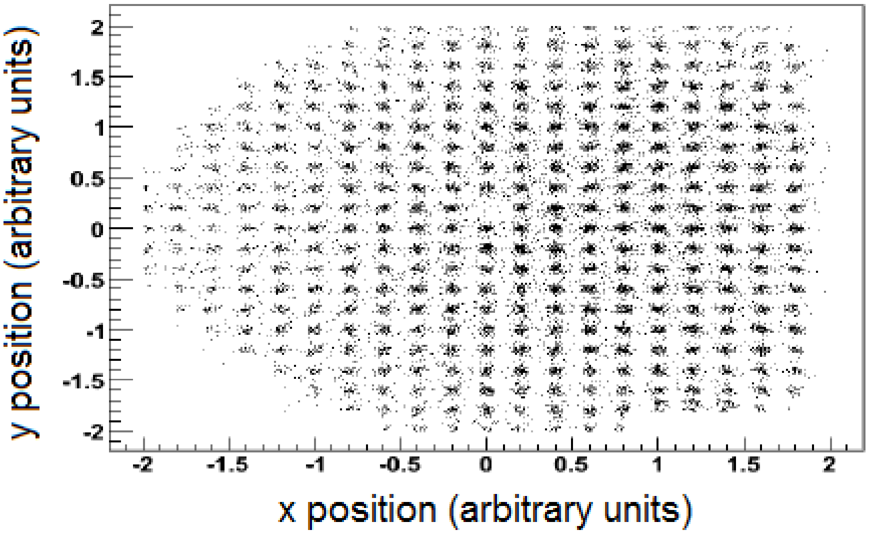

Figure 4.13: Corrected position data on the PSP detector, taken from [61].

4.3.2 Energy Calibration

The initial energy calibration procedure was much the same as discussed for the SSDs in Section 4.2.6. In this case three known energies were measured, this was considered sufficient to demonstrate a linear relationship between measured and calculated energy loss. The fit then gave the offset and gradient to correct future energy loss data.

4.3.3 Position Dependent Energy Calibration

To perform the position dependent energy calibration, data was taken from the pixel runs i.e. a broad illumination of a single energy. A histogram was made, binning the energy of all events as a function of x and y position on the detector. The total energy of each bin was then normalised against how many events contributed to that energy, giving an effective energy-per-hit for each position. These energy-per-hit values were then normalised against the value for the central bin, which was assumed to have the most proportionate response as it was the point equidistant from the contacts.

4.4 Crystal Ball

This calibration was generously shared by Ronja Thies.

4.4.1 Gamma-ray Calibration

The individual crystals of the Crystal Ball were gain matched for gamma-rays using two sources, giving four calibration energies: ^{22}Na giving 511 keV and 1275 keV; ^{88}Y giving 898 keV and 1836 keV, energies from [62]. For each crystal a plot of channel number against known energy can be made and fitted. The offset of the fit is interpreted as the effective pedestal value for the crystal, and the gradient as the required gain to convert channel number to energy.

4.4.2 Charged Particle Calibration

The charged particle calibration of the dual gain crystals was performed using cosmic muons. The muons have approximately 2 GeV and are minimally ionising, therefore they take a very straight path through the Crystal Ball. This is useful because the expected energy loss can only be calculated if the path length through the crystal is known. To ensure such a case, events are selected which have a high energy deposited in a crystal, with no energy in the neighbouring crystals and a high energy deposited in the crystal on the opposite side of the Crystal Ball, again with no energy in the neighbouring crystals. In this case it can be assumed that the muon traversed the centre of the crystals and so has a known path length. The muon will have deposited approximately 90 MeV in both crystals, and this can be compared to the measured energy.

It is also possible to reconstruct a path for muons which "graze" the side of the crystal ball. In this case a chain is made of five to eight adjacent crystals all with high energy hits, and no energy in neighbouring crystals, excepting the others in the chain. The path of the muon through the central crystals of this chain can be approximated, and so an expected energy deposition of 45 MeV is calculated. Again, this can be compared to the measured energy and the crystals gain matched.

It should be noted that only the dual gain crystals can give a proportionate response to charged particles. The other crystals, lacking the low gain channel, will respond to a muon hit by giving a saturated energy signal. This can still be used, because it shows that a muon hit occurred [67][68].

4.5 GFIs

This calibration was generously shared by Matthias Holl.

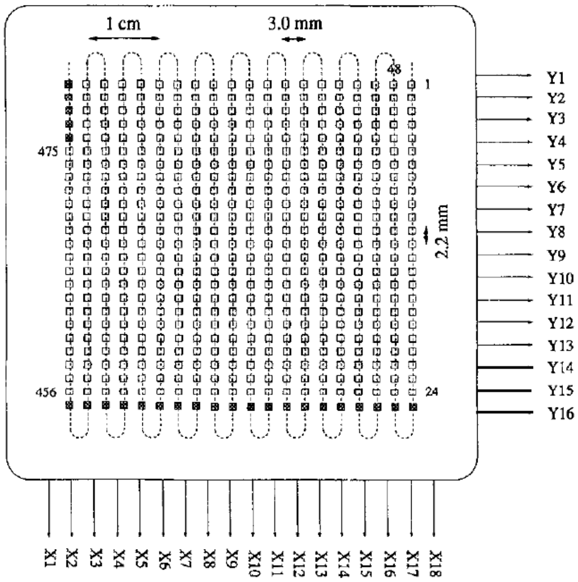

Figure 4.14: A schematic of a GFI detector's fibres on the PMT, from [55].

The fibres of the GFIs form a grid on a position sensitive PMT, as shown in Figure 4.14.

In order to get useful position information from the GFIs, a calibration was required to convert x and y position on the position sensitive PMT to horizontal position on the detector face. The hits on the position sensitive PMT appeared in clusters, each cluster centring on the location where one of the fibres connected to the PMT. The clusters formed a rough grid, which allowed each cluster to be given an xy index to describe its position on the grid. This index had a simple relationship to fibre number, which had a known conversion to horizontal position on the detector face. So after calibration, the horizontal position of a hit on a GFI could be easily calculated from the position of the hit on the PMT. To aid this, each cluster was fitted with a Gaussian describing its x and y distribution on the PMT. The spread of the cluster in x and y was taken as the standard deviation of the Gaussian, which allowed hits to be more easily distinguished from noise.

4.6 TFW

Parts of this calibration were generously shared by Matthias Holl.

The measured energies of the TFW require pedestal subtractions in the same way as described for the SSDs in Section 4.2.2. After this, the individual paddles must be synchronised in terms of energy and time. This is accomplished by exposing the target to beam, and selecting events which trigger exactly one horizontal and one vertical paddle. The travel time for the particle through the 5 mm depth of the first paddle can be neglected, and so any time offset between the two paddles can be corrected. By repeating this process all paddles can be corrected to one arbitrary offset. Similarly the energy loss through the first paddle is minimal and so the energy losses in both paddles can be treated as equivalent, and all paddles corrected to give the same energy signal. For more detail on this “self-calibration” see [65].

Once the paddles are synchronised, an absolute gain matching can be performed as discussed for the SSDs in Section 4.2.6.

5 Analysis

This chapter introduces the methods used to analyse the experimental data. The bulk of the analysis was performed using the ROOT data analysis program and libraries [69], with many smaller scripts and sub-programs written to support this. These programs dealt with the calibrated data, as discussed in Chapter 4.

The first stage was isolation of a single isotope from the mixed beam. Then a program called the "tracker" was used to identify the reaction fragments of each event. The tracking had to be run separately for each charge, and exhibited some charge dependent behaviour necessitating alternate methods for some charge 2 (helium) fragments. The integrated counts of the reaction fragments were then converted into cross sections. Finally the distribution of hits on the TFW was examined as an indicator of the transverse momentum distribution of the fragments.

5.1 Tracking

For all of the reaction fragments, the key measurements were mass and charge. The charge was determined by energy loss in the downstream SSDs and the TFW, as described during the discussion of Equation 3.5, in Section 3.3.2. The benefit of using both the SSDs and the TFW to measure charge was that it could be asserted that the particle had not broken up in flight [3] (although this did not exclude the loss of neutrons). This selection process is shown in Figure 5.1.

However, measuring a fragment's mass is not as simple as a time of flight measurement. Such a measurement relies on a correlation between particle velocity and mass; this correlation existed before the target as it was selected based on these criteria by the FRS. After the target, particles which have reacted and changed mass, would not have

---

[3] The flight time between the downstream SSDs and the TFW was of the order 10 nanoseconds.

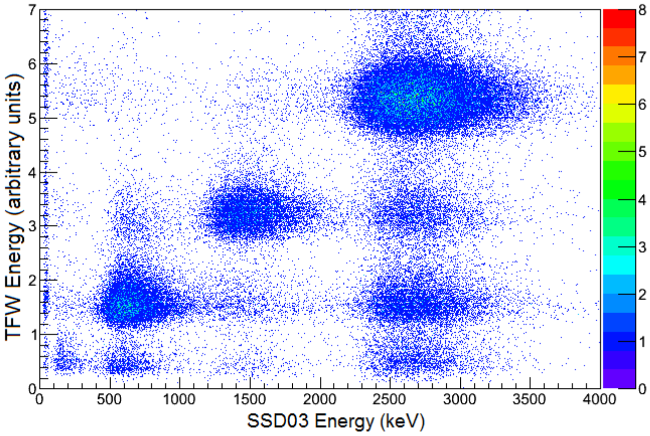

Figure 5.1: A spectrum showing charge selection during the tracking process. The loci lying along the diagonal are fragments which kept the same charge between the downstream SSDs and the TFW. There is a number of explanations for the three loci of events which appear to lose charge between the SSDs and the TFW, i.e. the three lower loci forming the vertical column at around 2700 keV. Firstly these events may have reacted with the SSDs, or some other part of the equipment; secondly they may have broken up in flight and finally they may be the result of a reconstruction error i.e. mismatched events between the SSDs and the TFW. In all instances these events have been removed from the analysis.

changed appreciably in velocity, so this correlation was lost. Therefore, mass was measured by observing how the particle's trajectory was changed by ALADIN, determining the magnetic rigidity and therefore the mass to charge ratio.

The "tracker" was a program written for this purpose by Ralf Plag [70]. This program calculated possible paths, then compared where these paths would strike the outgoing-fragment detectors, to where the detectors actually recorded hits, and calculated a chi-squared value. Figure 5.2 shows an example of this comparison. The tracker then varied the path and performed a chi-squared minimisation. Ultimately, the path with the best chi-squared was taken to be correct. The particle velocity could then be calculated using the distance of the path and the time measurement from the TFW. The velocity and curvature through the magnetic field were then used to calculate the particle's mass to charge ratio; this could then be used with the measured charge to

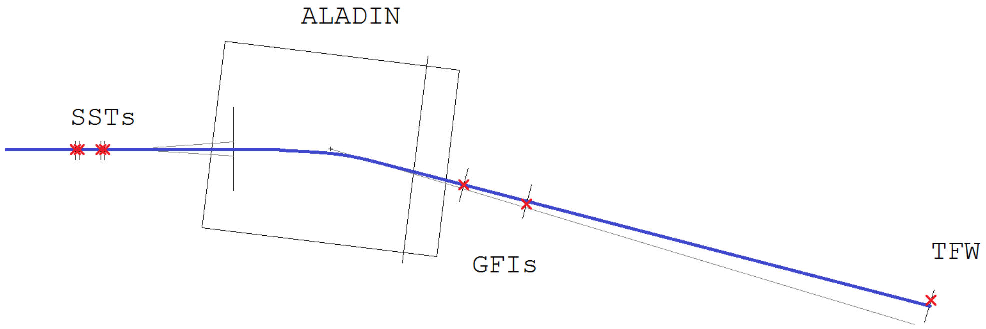

Figure 5.2: Comparison between tracker path and recorded hits. The blue line is the path being tested and the red crosses represent the hits recorded on the detectors.

calculate the mass.

The calculated masses were then collated giving a histogram of fragment masses for each charge, an example of which is shown in Figure 5.3. These mass peaks were then fitted using a script which fitted multiple Gaussian curves simultaneously, to avoid double counting any overlap between the mass peaks. The total number of counts for each peak was calculated as the area of the fitted Gaussian curve for that peak. The error on the number of counts was calculated from the fitting error. Because the tracker rejected events which were not successfully tracked, the mass spectra produced had very little background - any background was dwarfed by the effect of the adjacent mass peaks overlapping. As a result no background subtraction was necessary for fitting of the mass spectra. For some spectra and peaks the fitting script did not give a good fit, as shown in Figure 5.4. The main causes of this were when the peaks had a non-Gaussian character, comparatively small peaks being missed by the script or the run having insufficient counts to form peaks recognisable by the script. For these spectra or peaks the number of counts in each mass peak was estimated by bin counting, judging by eye where the limits lay between peaks. The bin counting method was used for approximately $\frac{3}{4}$ of peaks. The error for this method was estimated by comparison to cases where a good fit had been made and by observing the deviations when making

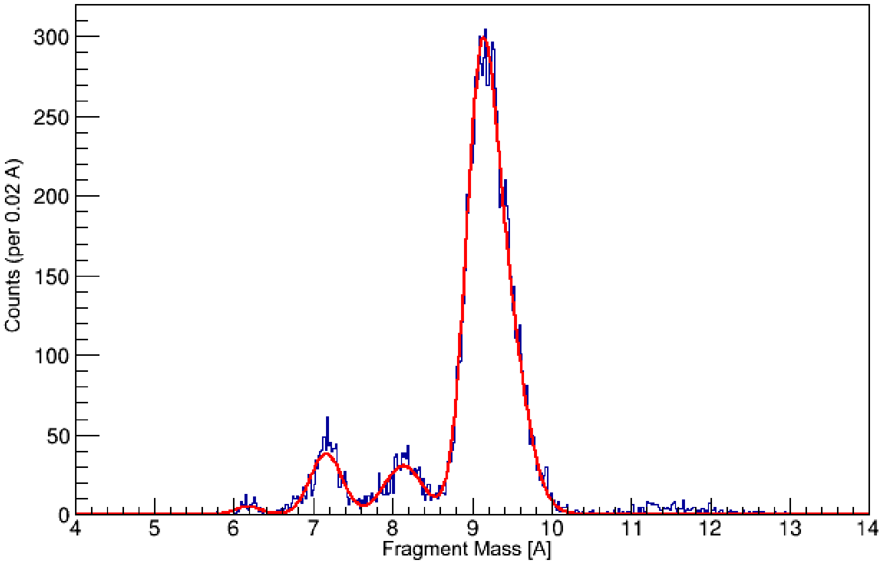

Figure 5.3: A well tracked fragment mass spectrum for charge 3 fragments from a ^{12}Be *beam and a carbon target.*

repeated measurements of a given peak; a value of 30% of the total counts in the peak was used.

The tracker required careful calibration of the detector positions and the strength of ALADIN's magnetic field. The detector positions were measured approximately during the experiment[4], but these values were fine tuned using the tracker. The magnetic field strength during the experiment was recorded indirectly via the current supplied to the coils. However, due to hysteresis effects the current was only a rough measure of the actual strength and so this in turn required more involved tuning. Fine tuning of this value was also needed as the magnetic field strength for all positions within ALADIN was interpolated from field maps measured for given currents; measuring the field maps was a labour intensive process and so was performed once and not repeated for each new experiment using ALADIN. Consequently the field maps were not measured at the time of the experiment, but at an earlier date. If improperly tuned, the spectra produced by

---

[4] The positions of the SSDs were known to 0.5 mm resolution, the GFIs to 1 cm and the TFW to 2 cm.

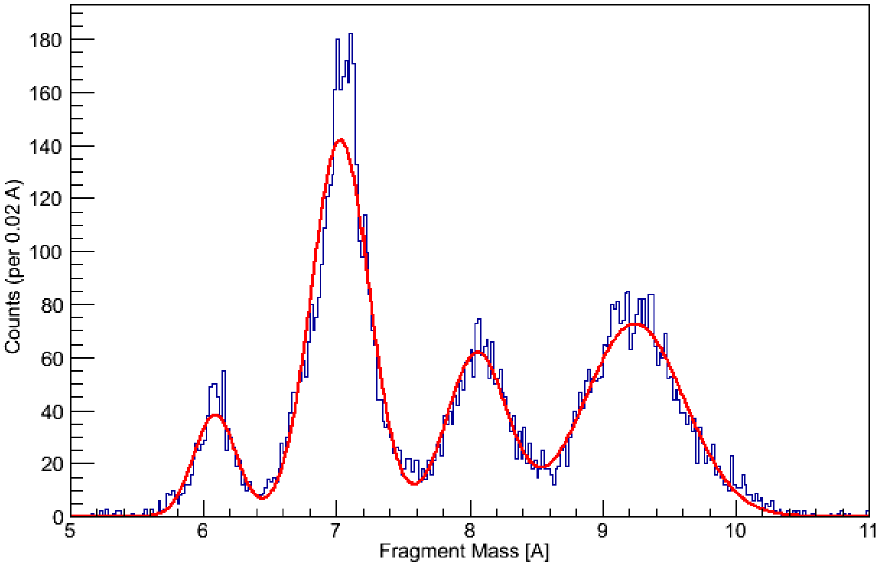

Figure 5.4: A poorly tracked fragment mass spectrum for charge 3 fragments from a ^{11}Be *beam and a polyethylene target. It is clear that the area of the fitted curves will not give an accurate estimate of the number of the counts in each mass peak, particularly A=7.*

the tracker suffered a reduction in both precision[5] and resolution; the tuning process therefore proceeded in large part by trial and error: making changes, re-tracking and judging whether the spectra had improved.

5.2 Problems with Tracking

The most significant problems with the tracking were not caused by the tracking algorithm itself, but by the detectors. It should be noted that some of the SSDs had a large number of dead strips and hence were not used in the analysis. Specifically, SSDs 1 and 5 were of no practical use and SSDs 6 and 7 had unusable k-sides. Only the in-beam SSDs were used by the tracker, and fortunately SSD 1 was redundant with SSD 2 so these issues did not interfere with tracking. A greater problem was caused by the charge dependant efficiency exhibited by the GFIs: the GFIs had a strongly charge

---

[5] A minor lack of precision can be seen in Figure 5.4, where the mass peaks do not all centre exactly on integer masses.

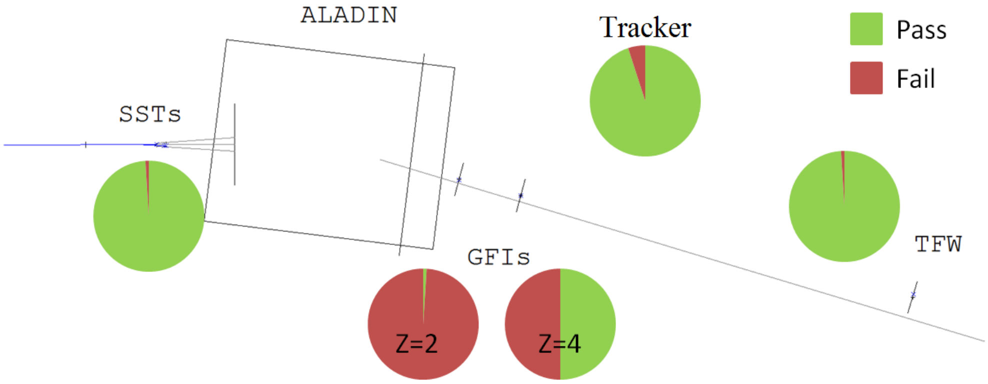

Figure 5.5: Losses in tracking due to detector efficiencies. The SSDs, TFW and tracker did not exhibit significant charge dependence in their efficiencies.

dependant efficiency being approximately 50% for charge 4 and 1% for charge 2.

As shown by Figure 5.5, the largest losses for light charged particles came from the GFIs. However, it was possible to more crudely track the fragments without the GFIs. This resulted in a significant loss in the resolution of the resulting mass spectra (as shown in the example in Figure 5.6, the mass peaks were broadened by an average of 35%), however the increase in efficiency (which in the example in Figure 5.6 was an increase from approximately 26% to 96%) compensated for this. All fragments of charge 3 or greater were tracked without the GFIs. For charge 2 fragments, the same method was attempted. However, the efficiency gain was minimal owing to a corresponding increase in the failure of the tracker to converge on a sensible mass - the tracker was less able to cope with fewer known positions when tracking charge 2 fragments. This is believed to be due to the details of the chi-squared minimisation process - where the step size had been chosen and optimised for higher charges.

Fortunately, for charge 2 fragments, the mass could be determined by another method. An approximation for outgoing angle was made by comparing the horizontal positions on the downstream SSDs, as shown by Figure 5.7.

The sine rule gives $\frac{h}{\sin 90} = \frac{x}{\sin\theta}$, h can be replaced with $\sqrt{L^2 + x^2}$; this reduces to L as $x << L$, giving $x = Lsin\theta$. Finally the small angle approximation gives $x = L\theta$,

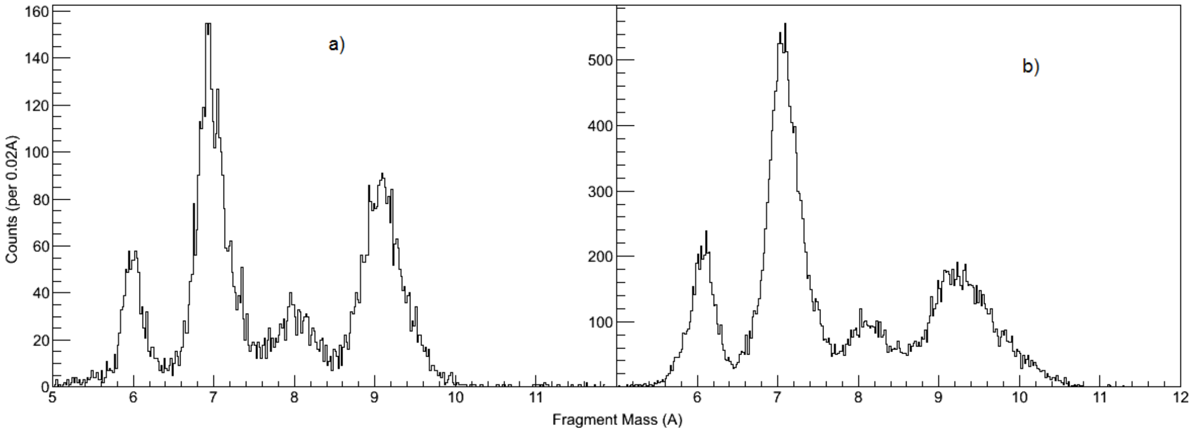

Figure 5.6: Tracking resolution (a) with and (b) without GFIs. Fitting a Gaussian to each of the mass peaks shows that all widths were increased, by an average of 35% as a result of tracking without the GFIs. The improvement in efficiency can also be seen, by the different scales of the two histograms (noting that the tracker was run on the same number of events both with and without the GFIs).

showing that x, the displacement, is linearly proportionally to θ, the outgoing angle, and so can be used for this purpose.

By plotting a particle's outgoing angle after the target against its horizontal position on the TFW, it was possible to see separate mass loci, as shown in Figure 5.8. The mass loci were separated because a particle's position on the plot depended on its magnetic rigidity; the position on the TFW compared to the outgoing angle provided an approximation of the curvature through ALADIN's magnetic field.

For greater charges, this would have resulted in a continuum, as can be seen in Figure 5.9, as the mass loci would be unresolved. However, for helium isotopes the mass to charge ratio varies more between neighbouring isotopes and also, as Table 5.1 shows, ^{5}He and ^{7}He are neutron unbound and will decay before leaving the target area. These effects make the separation clearer as the mass to charge ratio varies more between the observed isotopes. Another effect of this was that ^{4}He and ^{6}He may have been over-counted as, for example, any reaction fragments of ^{5}He were measured as ^{4}He. This effect may also have occurred for a number of other fragments which are the

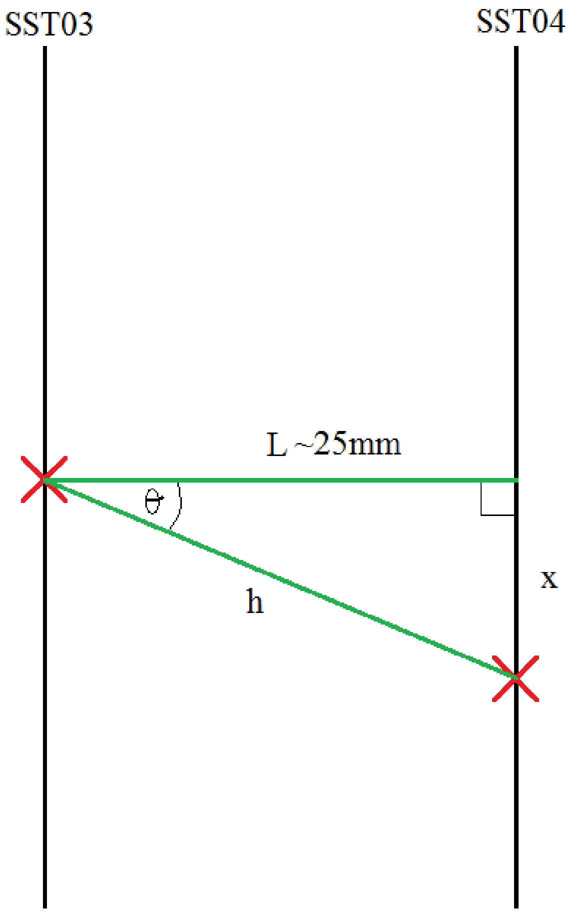

Figure 5.7: Horizontal displacement on the downstream SSDs as an approximation for outgoing angle. Where L is the distance between the two downstream SSDS, approximately 25 mm; x is the horizontal displacement, typically of order 0.1 mm; h is the hypotenuse of the right-angle triangle formed; and θ is the outgoing angle. The horizontal displacement has been exaggerate for clarity.

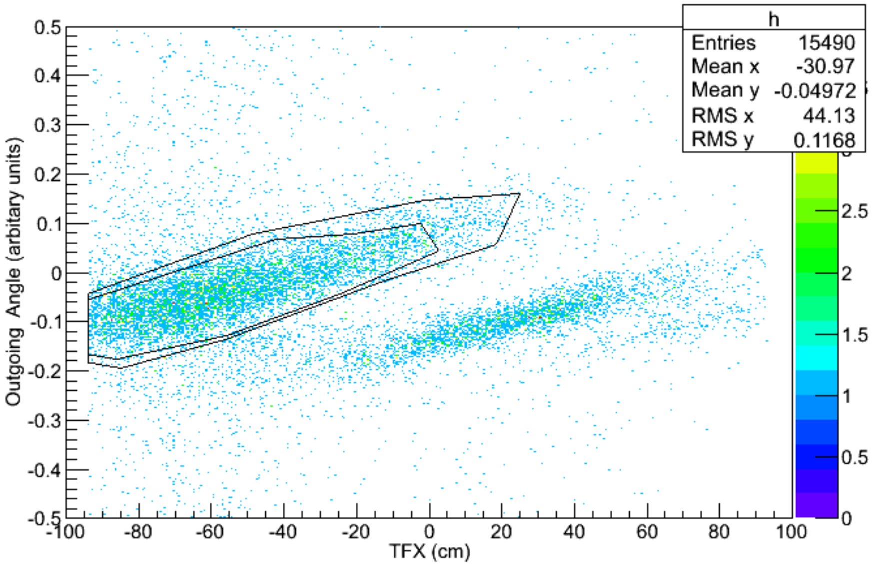

Figure 5.8: A plot of outgoing angle against TFW horizontal position, used to separate masses for charge 2 fragments. Two cuts are shown around the mass 4 locus, one tight and one loose. The other clear locus is mass 6 and there is a small locus of mass 8 on the far right.

Isotopes	Stability
^{3,4}He	Stable.
^{6,8}He	β-unstable, half-lifes of order 100 milliseconds.
^{5,7,9,10}He	neutron unbound, half-lives of order 10^{-21} seconds or shorter.

Table 5.1: The half-lives of isotopes of helium.

decay products of unbound parent nuclei.

This method was successful in separating the mass loci, but did not explicitly identify them. It was possible to clarify the specific masses measured by producing a linear fit for mass to charge ratio and horizontal position on the TFW as shown in Figure 5.10. This fit was calculated using successfully tracked masses (from higher charges) and their distributions on the TFW. By inputting the horizontal TFW position of the given locus into the linear fit, a mass to charge ratio was obtained for each mass locus. These mass to charge ratios gave an approximately integer mass for the given charge, and identified the mass loci as the expected (i.e. not neutron unbound) isotopes of

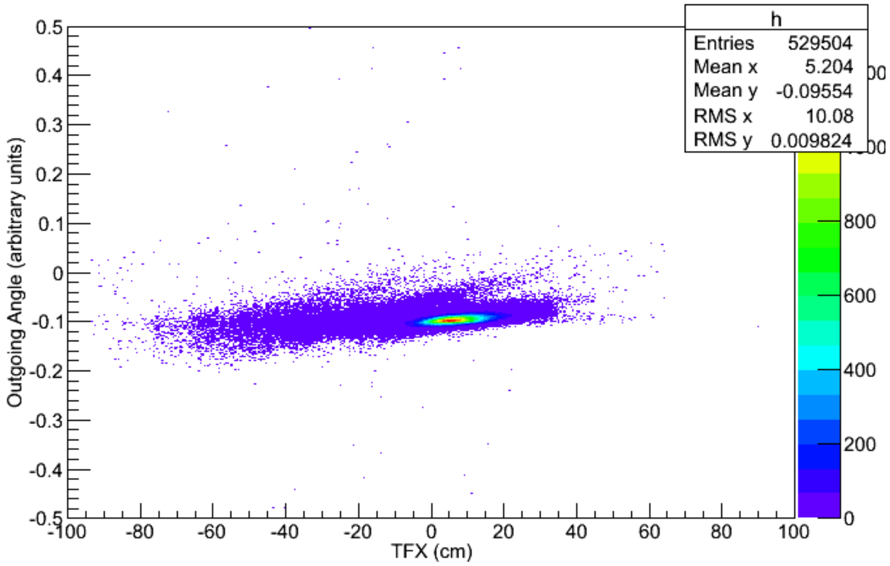

Figure 5.9: A plot of outgoing angle against TFW horizontal position for charge 4 fragments. The loci from the masses are not easily distinguishable; the only clear locus is the unreacted beam, which is visible not by separation but as a result of having comparatively more counts.

helium.

The total number of counts for each mass was the integrated number of counts within the locus, less a background subtraction. Clearly this method was sensitive to the cut used to select the loci, to allow for this, cuts were repeated several times. The average number of counts was used and the standard deviation taken as the error. Events outside the mass loci were considered background, resulting from detector noise or incorrectly reconstructed events. A background subtraction was performed by calculating the density of the background counts assuming a uniform distribution and that this same density continued under the mass loci. The calculated background density was also sensitive to the variation of the cuts, as was the cut area. For the cut area, again, the average of repeated cuts was used and the standard deviation taken as the error. The background density was calculated using the average counts and areas of all masses; the error was taken as the square root of the number of background counts, divided by

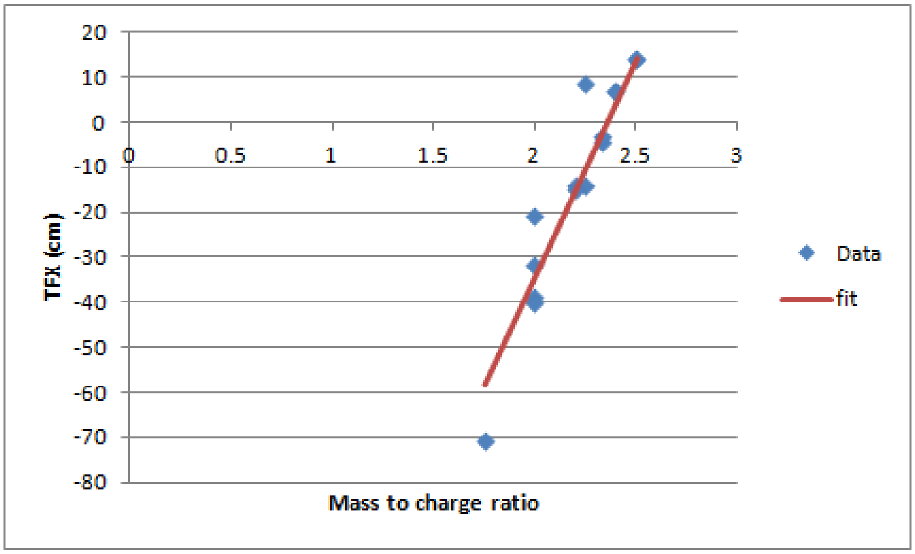

Figure 5.10: A plot of TFW horizontal position against mass to charge ratio. The linear fit is shown is sufficient to identify the masses of the loci shown in Figure 5.8.

the background area.

For some masses a further factor affected the total number of counts - the mass peaks fell partially outside of the horizontal acceptance of the TFW. A correction factor was calculated by locating the centre of the peak using a Gaussian fit (or by eye where there was insufficient counts) and assuming that the peak was symmetric about that centre. An example of where the acceptance cuts the distribution is shown in Figure 5.11. The error introduced by this method was calculated by repeating the method on peaks where the full width of the peak was available and comparing the estimated result to the actual number of counts.

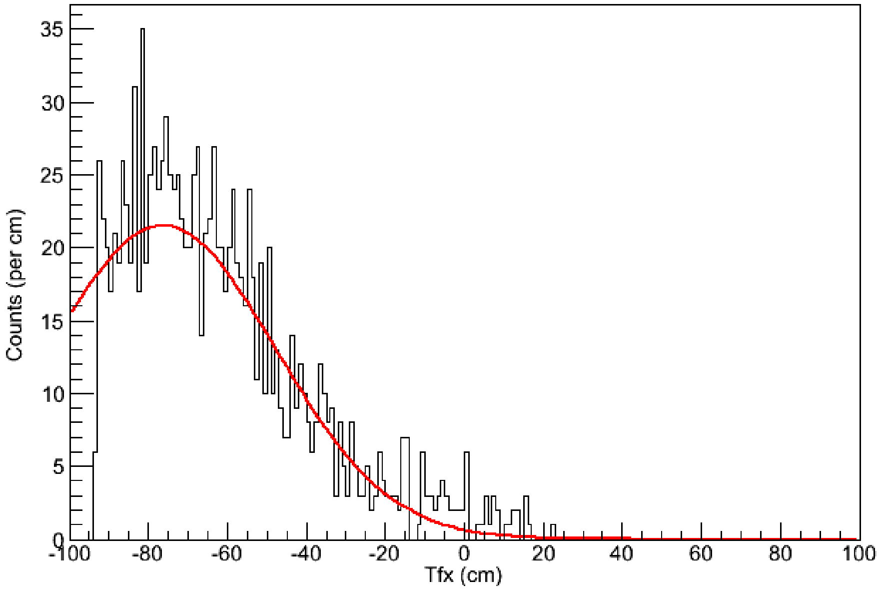

Figure 5.11: An example of where the finite horizontal acceptance of the TFW cuts the distribution.

5.3 Efficiency Calculations

The efficiency was calculated separately for each production run, beam isotope and fragment charge. Averaged over the available isotopes, $^{7,9-12}$Be & $^{8,10-15}$B, the average efficiencies were 60%, 79%, 94% and 99% for charges 2, 3, 4 and 5 respectively. All efficiency values are tabulated in Appendix D. Because of the differing methods for mass identification, the efficiency calculation varied depending on whether the fragment charge was 2 or greater. For charges greater than 2, i.e. where the tracker was used, the efficiency was taken as the fraction of events successfully tracked to a sensible mass, remembering that the unreacted beam was also tracked. The error on the numbers of events was taken as the square root of this number, and the final error on the efficiency was calculated by propagation of this error. The efficiency losses consisted of events where the tracker was unable to converge on a sensible mass, or events where a hit was not recorded on all required detectors on account of their own efficiencies. As such this tracking efficiency intrinsically included all detector efficiencies; the SSDs and the TFW had efficiencies of approximately 100%. As an example, for the charge 4 fragments from the ^{12}Be beam of run 386, the tracker successfully tracked 177306 events of the 177616 attempted. This gave an efficiency value of 0.9983 ± 0.0034.

For charge 2 fragments, the efficiency calculation was more complex. The efficiency was taken as the sum of counts for all mass loci (after the background subtraction) as a fraction of the total number of events. For example, in Figure 5.8, the background subtracted counts for the loci of ^{4}He, ^{6}He & ^{8}He would be summed, then this sum would be divided by the total number of events. Again, the error was calculated by propagation of statistical errors, with the error on the yield, area and background subtraction as described above. The error on the total number of events was taken as the square root of this number. The ^{10}B beam of run 451 is a simple example as it contained only ^{4}He fragments: The total number of events was 7875, the number of counts within the ^{4}He locus was 5006 with an area of 20.09 (arbitrary units). The number of counts considered background outside the locus was 1953 (some events fell outside of the main distribution around the loci and so could be neglected from the background calculation) with an area of 167.12, giving a background density of 11.69. This reduced the number of counts for the ^{4}He by 235 (11.69 × 20.09) to a total of 4771. This value was then divided by the total number of events to give the efficiency value of 0.6059 ± 0.026.

5.4 Cross Section Calculation

In order to convert a raw number of events into a cross section a normalisation is necessary, and in some cases also a carbon target component subtraction. Where a subtraction is not required the cross section can be calculated from Equation 5.1.

$$\sigma = \frac{Yield}{N_{beam}\epsilon N_t t} \tag{5.1}$$

where σ is cross section, $Yield$ is the raw number of events for the given reaction, N_{beam} is the total number of incoming events, ϵ is the efficiency, $N_t t$ is the areal density of the target (composed of N_t the target's number density and t the target's thickness).

Where a subtraction for the carbon component is required, the formula is slightly more complex. As discussed in Chapter 3, in lieu of a proton target a polyethylene target was used with data also being taken under the same conditions with a carbon target. Yields for both the polyethylene target and the carbon target are normalised against their respective beam counts and the efficiency, as in Equation 5.2.

$$T = \frac{Yield}{N_{beam}\epsilon} \tag{5.2}$$

This intermediate value from the carbon target is then multiplied by the ratio between the areal densities of the two targets. In other words, the value from the carbon target is normalised to the amount of carbon present in the polyethylene target. The subtraction can now be made, before the result is normalised against the areal density of the polyethylene target. This process is expressed by Equation 5.3.

$$\sigma = \frac{T_{polyethylene} - T_C \frac{N_t t(polyethylene)}{N_t t(C)}}{2N_t t\,(polyethylene)} \tag{5.3}$$

where $N_t t\,(C)$ and $N_t t\,(polyethylene)$ are the areal densities of the carbon target and the polyethylene target respectively. The factor of 2 in the denominator is required to account for the polyethylene target having 2 hydrogen nuclei for each molecular centre. Equation 5.3 is useful in showing how the carbon subtraction works, but for ease of calculation it can be rearranged as Equation 5.4:

$$\sigma = \frac{T_{polyethylene}}{2N_t t\,(polyethylene)} - \frac{T_C}{2N_t t\,(C)} \tag{5.4}$$

With reference to Equation 5.1 it can be seen that the final cross section is simply the cross section for polyethylene target minus the half the value of the cross section for the carbon target, as shown in Equation 5.5:

$$\sigma = \sigma\left(polyethylene\right) - \frac{\sigma\left(C\right)}{2} \tag{5.5}$$

The following is a worked example of this calculation for single neutron knockout from a beam of ^{10}Be at an energy of 5366 MeV. Starting at the point of having extracted yields from the mass spectra produced by the tracker:

$$Yield(polyethylene) = 326.22 \pm 97.87$$

$$Yield(C) = 339.38 \pm 101.81$$

These values are then normalised to the separate cross section values using Equation 5.1. The relevant constants are:

$$N_{beam}(polyethylene) = 87856$$

$$\epsilon(polyethylene) = 0.9984 \pm 0.0053$$

$$N_t t(polyethylene) = 3.96551 \times 10^{26}$$

$$N_{beam}(C) = 118924$$

$$\epsilon(C) = 0.9984 \pm 0.0045$$

$$N_t t(C) = 4.68954 \times 10^{26}$$

The normalisation gives:

$$\sigma(polyethylene) = 93.78 \pm 28.14 \ mb$$

$$\sigma(C) = 60.95 \pm 18.29 \ mb$$

As discussed above, there are 2 hydrogen nuclei in each polyethylene molecule, so the cross-section for polyethylene needs to be scaled by this factor, giving:

$$\sigma(polyethylene) = 46.89 \pm 14.07\ mb$$

The final stage is the carbon subtraction, using Equation 5.5. This gives a cross section of:

$$\sigma = 16.42 \pm 16.78\ mb$$

The error on this value comes from the error in measuring the yield and the error on the efficiency value, the error on the total number of incoming events and the error on the details of the target being negligible in comparison. The formula for the error was calculated by propagation of error and is shown in Equation 5.6.

$$E_{cs} = \sqrt{\left(\frac{E_{Yield}}{N_{beam}\epsilon N_t t}\right)^2 + \left(\frac{E_\epsilon Yield}{N_{beam}\epsilon^2 N_t t}\right)^2} \tag{5.6}$$

where E_{cs} is the error on the cross section, E_{Yield} is the error on the Yield, E_ϵ is the efficiency and all other symbols keep their previous definitions. Where a subtraction is required, the combined error is shown by Equation 5.7; the differing targets do not complicate the equation as the error from the target details is neglected.

$$E_{cs} = \sqrt{E_{polyethlene}^2 + \frac{E_C^2}{4}} \tag{5.7}$$

Table 5.2 shows the calculation of all cross sections for of ^{10}Be at an energy of 5366 MeV.

Target	Fragment	Yield	ϵ	σ (milli-barns)	Error Contribution	
					Yield	ϵ
Carbon	^{4}He	382.11 ± 16.40	0.6550 ± 0.0230	104.61 ± 5.79	55.19%	44.81%
polyethylene		389.74 ± 20.52	0.6285 ± 0.0093	89.00 ± 4.88	78.00%	22.00%
proton		-	-	36.70 ± 5.67	-	-
Carbon	^{6}He	62.51 ± 13.30	0.6550 ± 0.0230	17.11 ± 3.71	86.01%	13.99%
polyethylene		67.82 ± 5.88	0.6285 ± 0.0093	15.49 ± 1.36	85.37%	14.63%
proton		-	-	6.93 ± 2.30	-	-
Carbon	^{7}Li	178.63 ± 53.59	0.9784 ± 0.033	32.74 ± 9.88	89.85%	10.15%
polyethylene		217.24 ± 65.17	0.9923 ± 0.031	31.42 ± 9.48	90.61%	9.39%
proton		-	-	15.05 ± 10.69	-	-
Carbon	^{8}Li	42.05 ± 12.61	0.9784 ± 0.033	7.71 ± 2.33	89.85%	10.15%
polyethylene		34.51 ± 5.72	0.9923 ± 0.031	4.99 ± 0.84	84.20%	15.80%
proton		-	-	1.14 ± 1.44	-	-
Carbon	^{9}Li	113.59 ± 34.08	0.9784 ± 0.033	20.82 ± 6.29	89.85%	10.15%
polyethylene		144.20 ± 43.26	0.9923 ± 0.031	20.86 ± 6.29	90.61%	9.39%
proton		-	-	10.45 ± 7.03	-	-
Carbon	^{9}Be	339.38 ± 101.81	0.9984 ± 0.0045	60.95 ± 18.29	98.52%	1.48%
polyethylene		326.22 ± 97.87	0.9984 ± 0.0053	46.89 ± 14.07	98.25%	1.75%
proton		-	-	16.42 ± 16.78	-	-

Table 5.2: Cross section calculations for all reaction fragments of ^{10}Be *at an energy of 5366 MeV.*

5.5 TFW Peak Widths

In addition to the cross sections, it was also of interest to measure the angular distribution of reaction fragments as this provided an indication of the transverse momentum distribution. Systematic changes in these widths can therefore be used to investigate how cluster structure changes with neutron number, as discussed in [71]. For all fragments, this was performed in essentially the same way. The given reaction fragment was isolated using the method previously discussed for mass and charge identification. The events for the given fragment only were then plotted on horizontal axis of the TFW and fitted with a Gaussian; the width of this Gaussian was taken to represent the angular spread. Peak widths were then measured for the unreacted beam in empty target runs, this data is shown in Figure 5.12. A rough linear decrease of width with beam mass can be seen, this relationship was used to correct widths against the small mass variation. This was performed by subtracting (in quadrature) the calculated empty target run width from the measured width.

Corrected widths were then compared for the unreacted beams through all targets, in order to establish the effect of the target on straggling in energy and angle. This data is shown in Figure 5.13; the effect from differing targets appears insignificant, within experimental error. This lack of effect from the targets allows the analysis of the reaction product data, presented in Section 6.5.

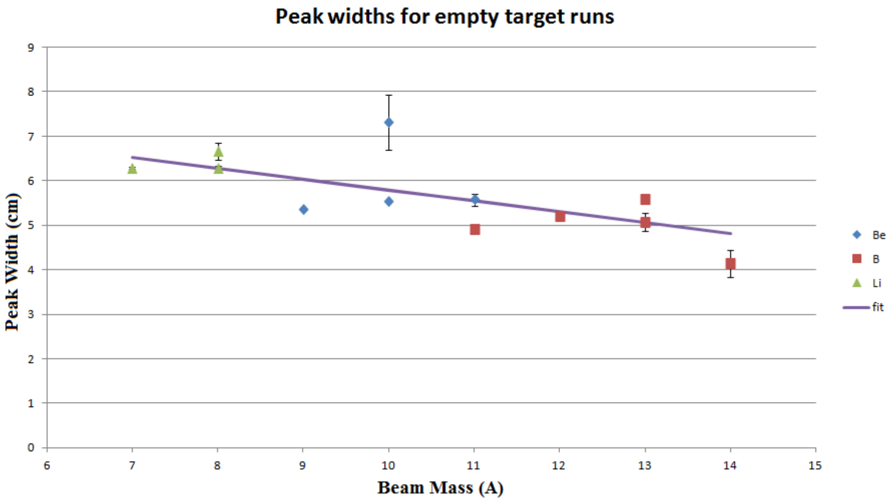

Figure 5.12: Peak widths on the TFW for the empty target runs.

Figure 5.13: Corrected TFW peak widths for all targets for beryllium beams.

6 Results & Discussion

This chapter presents the measured cross sections of fragments resulting from reactions between $^{7,9-12}$Be & $^{8,10-15}$B beams and the proton & ^{12}C targets. The energy dependence of these cross sections is then investigated. The cross sections for single neutron knockout, single proton knockout, α cluster knockout, ^{6}He knockout and the total cross sections are used to investigate how the beryllium and boron structures change with neutron number. The α cluster knockout cross sections are also compared to AMD measurements. Finally the fragment TFW peak widths are examined for systematic trends with changing neutron number.

6.1 Breakup cross sections on proton target

This section presents examples of cross sections for breakup on the proton target for $^{7,9-12}$Be and $^{8,10-15}$B beams. The remaining graphs are in Appendix E, where Figures E.1 to E.7 show data for beryllium beams and Figures E.8 to E.17 show data for boron beams. The data is also presented in table form in Appendix F.

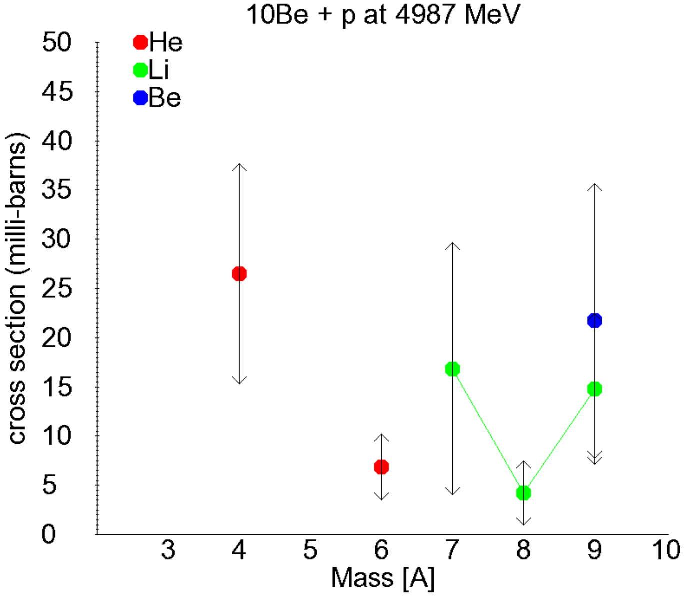

Figure 6.1: Cross sections for reaction fragments of ^{10}Be+p *at 4987 MeV.*

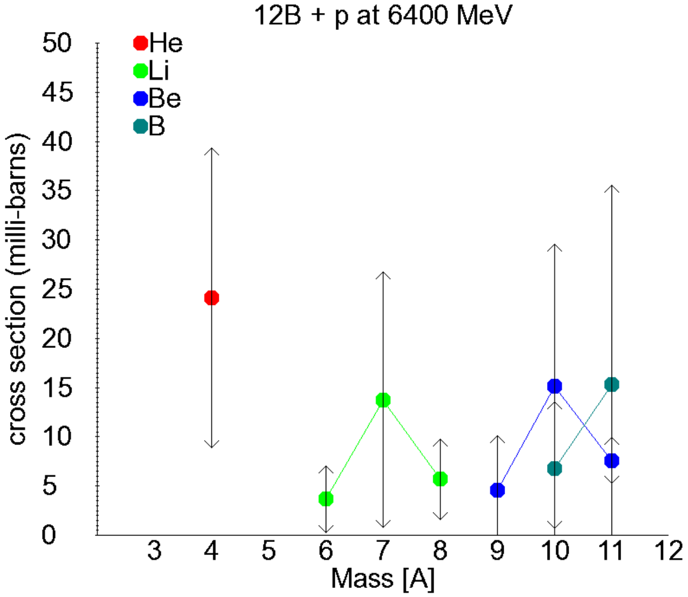

Figure 6.2: Cross sections for reaction fragments of ^{12}B+p *at 6400 MeV.*

6.2 Breakup cross sections on ^{12}C target

This section presents examples of cross sections for breakup on the ^{12}C target for $^{7,9-12}$Be and $^{8,10-15}$B beams. The remaining graphs are in Appendix G, where Figures G.1 to G.9 show data for beryllium beams and Figures G.10 to G.19 show data for boron beams. The data is also presented in table form in Appendix H.

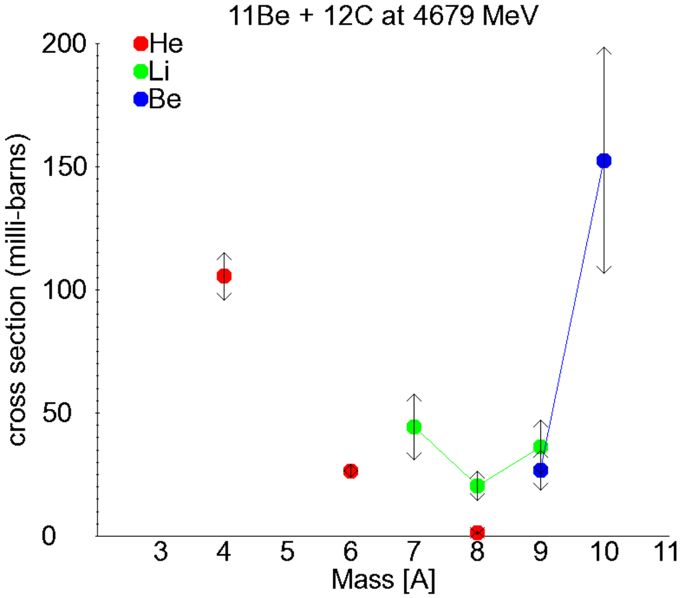

Figure 6.3: Cross sections for reaction fragments of ^{11}Be+^{12}C *at 4679 MeV.*

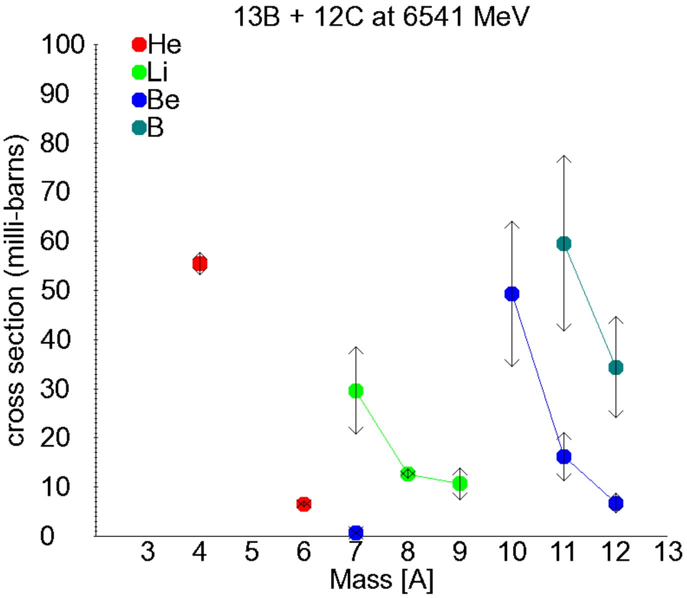

Figure 6.4: Cross sections for reaction fragments of ^{13}B+^{12}C *at 6541 MeV.*

6.3 Energy Dependence

For some isotopes, cross sections have been measured at more than one beam energy. It is of general interest to observe how the cross sections change with energy, but it is of particular importance in this analysis because it tests the validity of comparing cross sections with dissimilar energies, as is undertaken in Section 6.4. For ease of distinguishing data points, Figures 6.5 to 6.18 have some masses offset slightly on the x-axis.

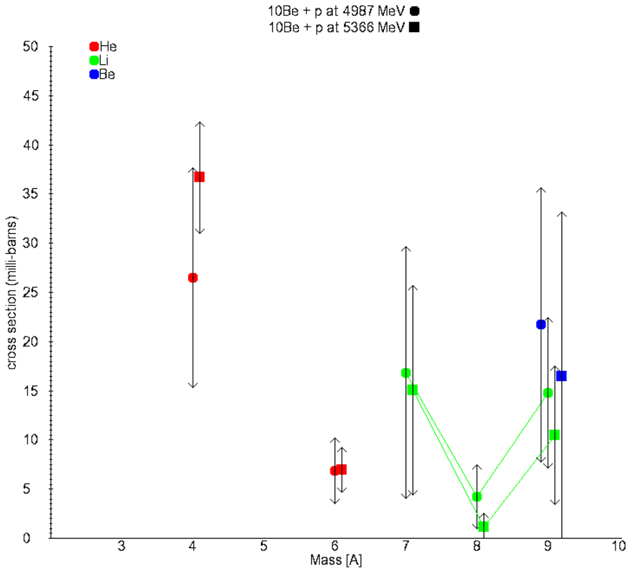

Figure 6.5: A comparison of cross sections for ^{10}Be+p *at 4987 and 5366 MeV.*

Figure 6.5 shows a comparison for the reaction fragments for a ^{10}Be beam on proton target at 4987 MeV and 5366 MeV. All cross sections are within error of their counterpart at the other energy. Figure 6.5 shows a good example of a behaviour seen for some, but not all, reactions: the cross sections for the lithium fragments are staggered with higher cross sections for the odd mass fragments. It is possible that this effect is caused by the relative Q-values for the reactions. The Q-values for the breakup of ^{10}Be into ^{7}Li, ^{8}Li and ^{9}Li are -17.250 MeV, -21.474 MeV and -19.636 MeV respectively. As discussed in Sections 1.4.2 and 6.4, cross sections are strongly correlated with the reaction Q-values.

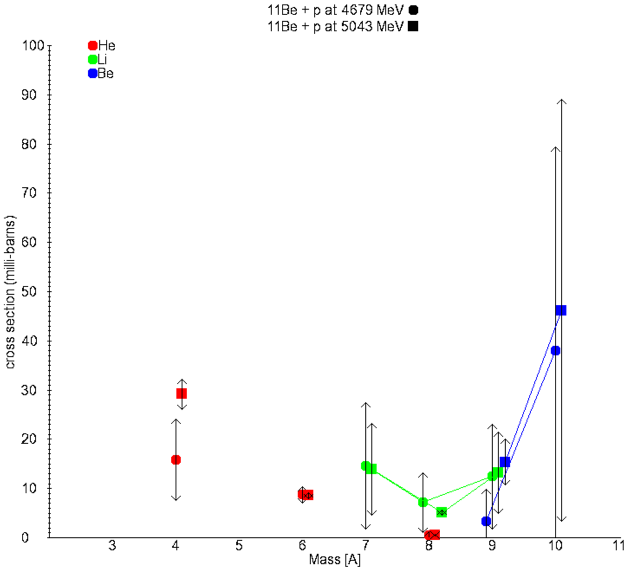

Figure 6.6: A comparison of cross sections for ^{11}Be+*p at 4679 and 5043 MeV.*

For ^{11}Be+p, Figure 6.6, all cross sections are again within error with the exceptions of ^{4}He and ^{9}Be which both differ by roughly 1.5 sigma.

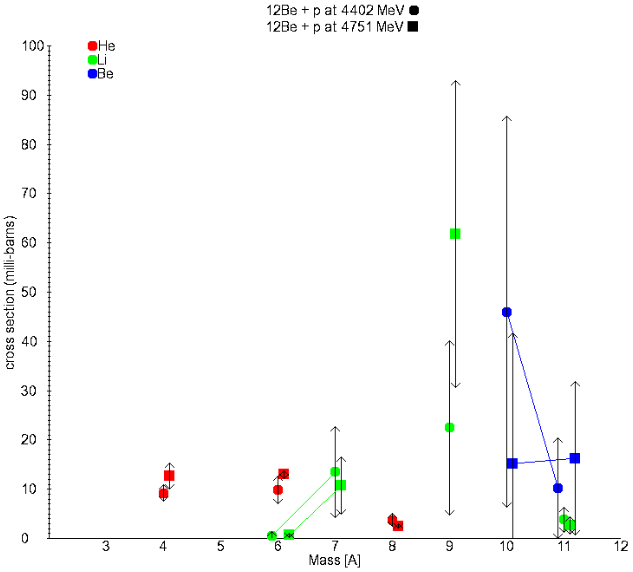

Figure 6.7: A comparison of cross sections for ^{12}Be+*p at 4402 and 4751 MeV.*

Figure 6.7 shows the energy comparison for ^{12}Be+p. Again all cross sections are within error, except ^{4}He, ^{6}He, ^{9}Li, which differ by less than 1.1 sigma.

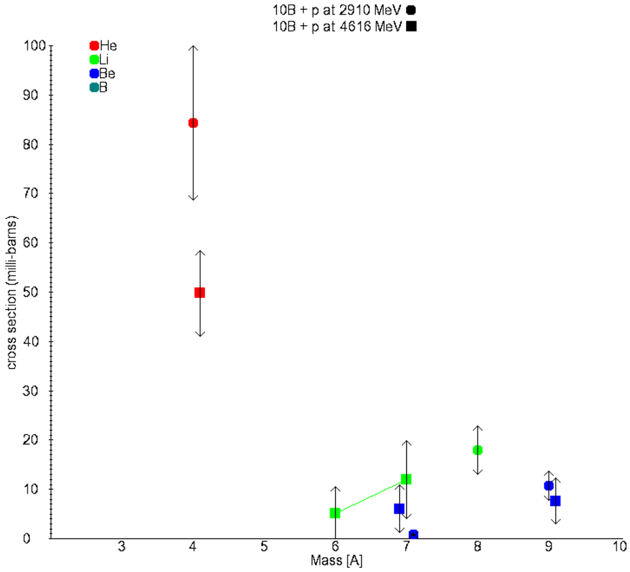

Figure 6.8: A comparison of cross sections for ^{10}B+*p at 2910 and 4616 MeV.*

Figure 6.8 shows the energy comparison for ^{10}B+p. Due to low statistics, cross sections were not measured for all reaction fragments at both energies meaning it is only possible to compare 3 of the 6 observed fragments. Of the comparable cross sections only the cross sections for single neutron knockout agree within error. The cross sections for ^{7}Be differ by about 1.1 sigma, and the cross sections for ^{4}He differ by about 1.9 sigma.

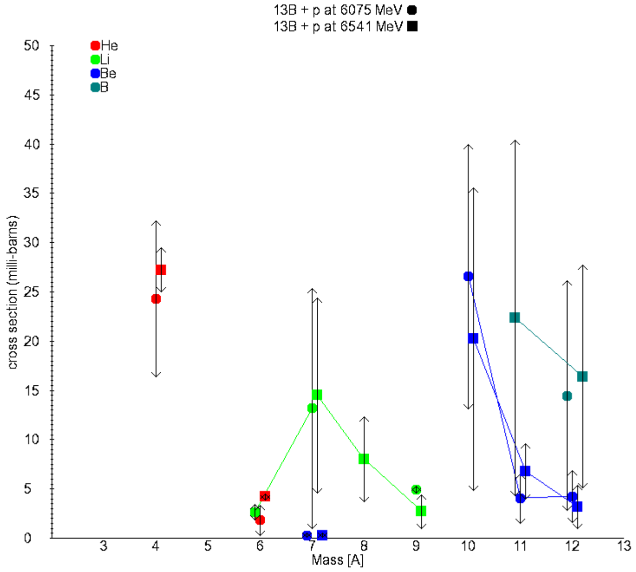

Figure 6.9: A comparison of cross sections for ^{13}B+*p at 6075 and 6541 MeV.*

Figure 6.9 shows the energy comparison for ^{13}B+p. Cross sections agree within error except ^{6}He and ^{9}Li which differ by roughly 1.5 and 1.3 sigma respectively.

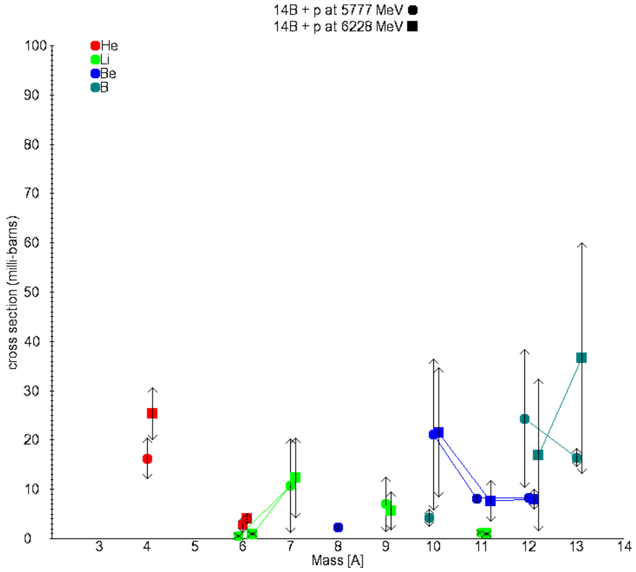

Figure 6.10: A comparison of cross sections for ^{14}B+*p at 5777 and 6228 MeV.*

Figure 6.10 shows the energy comparison for ^{14}B+p. All cross sections are within error of their counterpart at the other energy except ^{4}He and ^{6}Li which differ by less than 1.4 sigma and 1.2 sigma respectively.

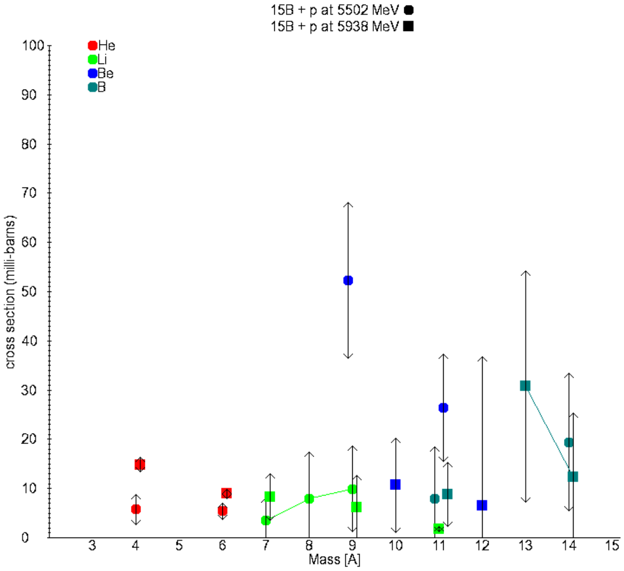

Figure 6.11: A comparison of cross sections for ^{15}B+*p at 5502 and 5938 MeV.*

Figure 6.11 shows the energy comparison for ^{15}B+p. Cross sections are in agreement, which the exception of ^{4}He and ^{6}He which disagree by 2.7 sigma and 1.75 sigma respectively.

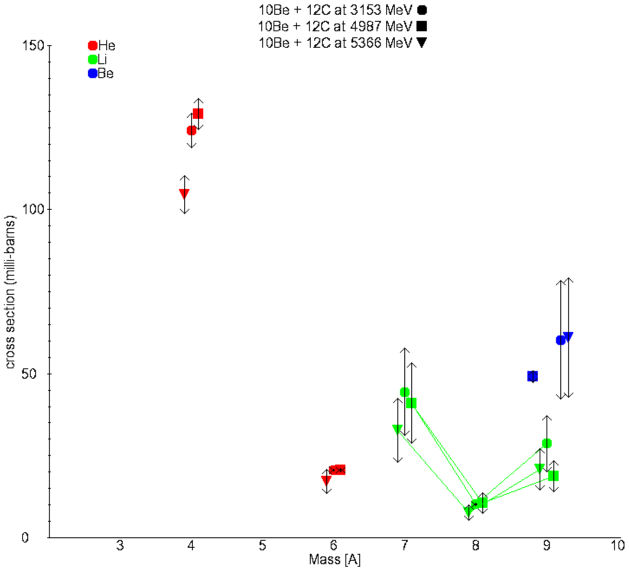

Figure 6.12: A comparison of cross sections for ^{10}Be+^{12}C *at 3152, 4987 and 5366 MeV.*

Figure 6.12 shows the energy comparison for ^{10}Be+^{12}C. All cross sections agree well within error, with the exception of ^{4}He at 5366 MeV, which disagrees with the values at the other energies by 2.5 sigma and 3.2 sigma.

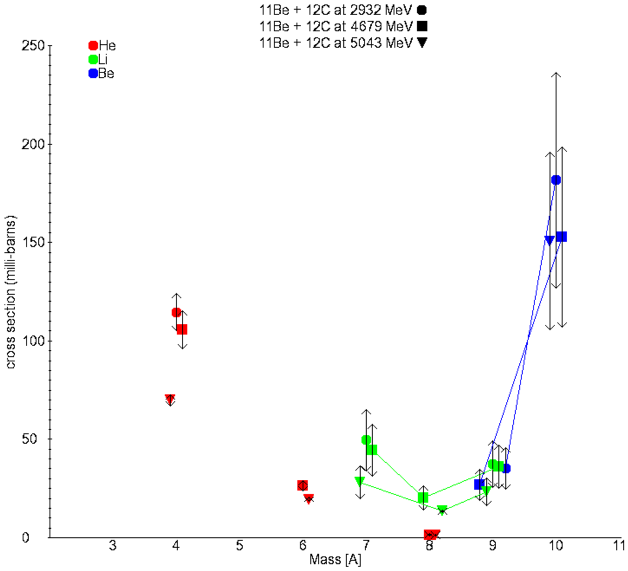

Figure 6.13: A comparison of cross sections for ^{11}Be+^{12}C *at 2931, 4679 and 5042 MeV.*

Figure 6.13 shows the energy comparison for ^{11}Be+^{12}C. The agreement is generally good, but as with the cross sections for ^{10}Be, there is a disagreement for ^{4}He at the highest beam energy, in this case of 4.6 and 3.51 sigma, while the other cross sections for ^{4}He agree well within error. There is also a disagreement by 2.5 sigma for the two measured cross sections for ^{6}He. Finally the cross sections for ^{8}Li differ by 1.1 sigma.

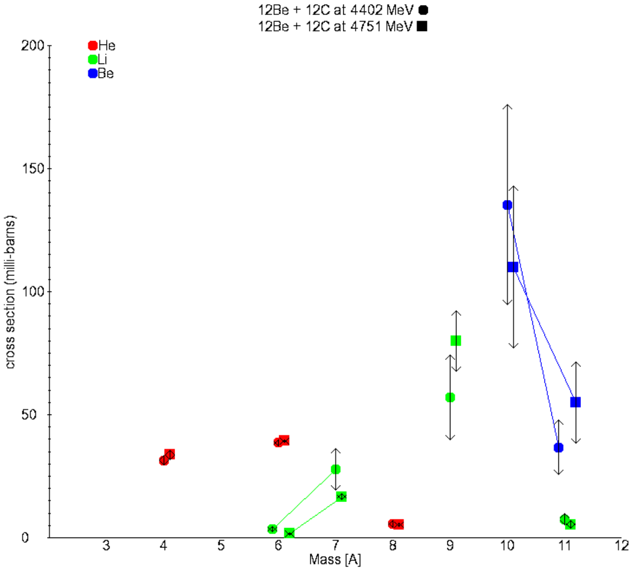

Figure 6.14: A comparison of cross sections for ^{12}Be+^{12}C *at 4401 and 4750 MeV.*

Figure 6.14 shows cross sections for ^{12}Be+^{12}C. Cross sections agree within error with the exceptions of ^{6}Li, ^{7}Li and ^{9}Li which differ by 1.5, 1.3 and 1.1 respectively.

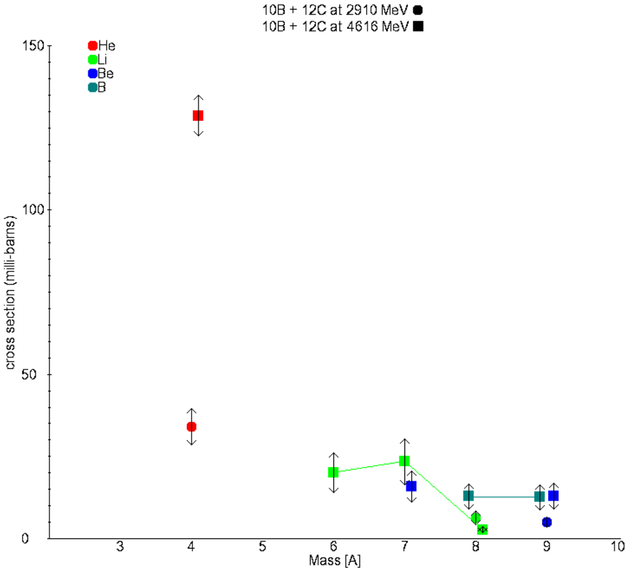

Figure 6.15: A comparison of cross sections for ^{10}B+^{12}C *at 2909 and 4615 MeV.*

Figure 6.15 shows cross sections for ^{10}B+^{12}C. Again few comparisons are possible due to low statistics. The cross sections for ^{8}Li and ^{9}Be disagree slightly, by 1.5 sigma and 1.9 sigma respectively. The cross sections for ^{4}He differ wildly by 11.5 sigma.

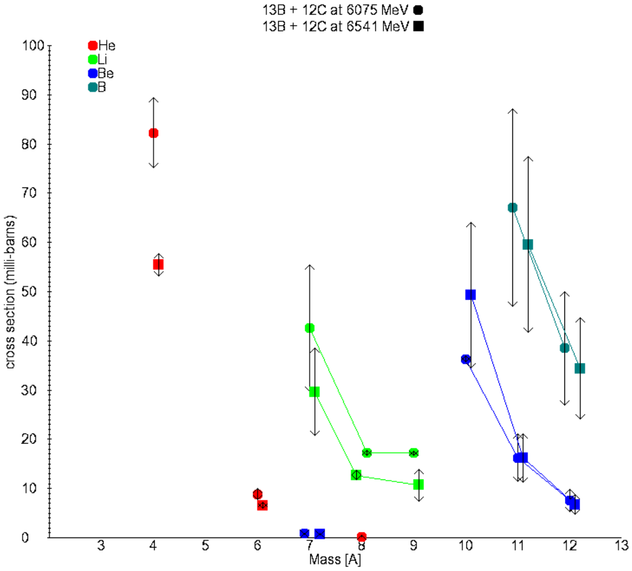

Figure 6.16: A comparison of cross sections for ^{13}B+^{12}C *at 6074 and 6541 MeV.*

Figure 6.16 shows cross sections for ^{13}B+^{12}C. Cross sections generally agree within error, but for ^{6}He differ by 1.8 sigma, for ^{9}Li differ by 2.0 sigma, for ^{4}He differ by 3.6 sigma and by ^{8}Li differ by 4.2 sigma.

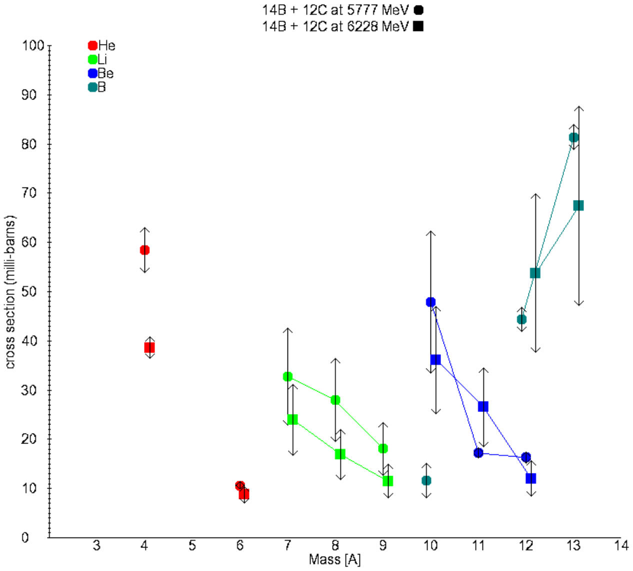

Figure 6.17: A comparison of cross sections for ^{14}B+^{12}C *at 5776 and 6227 MeV.*

Figure 6.17 shows cross sections for ^{14}B+^{12}C. Around half of the cross sections agree within error. Cross sections for ^{4}He differ by 3.9 sigma, for ^{8}Li by 1.1 sigma, for ^{11}Be by 1.2 sigma, for ^{12}be by 1.1 sigma.

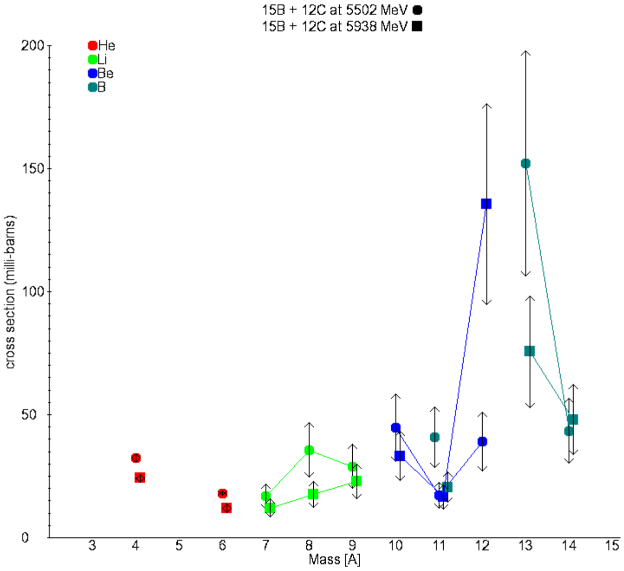

Figure 6.18: A comparison of cross sections for ^{15}B+^{12}C *at 5502 and 5938 MeV.*

Figure 6.18 shows cross sections for ^{15}B+^{12}C. Cross sections for ^{4}He and ^{6}He differ substantially, by 3.5 sigma and 3.1 sigma respectively. Cross sections for ^{8}Li, ^{11}B and ^{13}B all differ 1.5 sigma. Cross sections for ^{12}Be differ by 2.3 sigma.

There is strong evidence that the breakup cross sections have no systematic dependence on energy, in this energy region and over this energy range. Cross sections predominantly agree within error for the available energy comparisons and, where they do not agree, no obvious trend can be seen of the lower or higher energy consistently having the larger cross section. To confirm this an average ratio was calculated for cross section at high energy to cross section at low energy. The value was 1.096 ± 0.109; this is within error of 1, suggesting no relationship between energy and cross section.

6.4 Change with Neutron Number

Investigating how the breakup cross sections change with the neutron number of the projectile isotope can reveal how the structure of that element changes with changing neutron number. This can then be compared to AMD predictions, as discussed in Section 2.5. Cross sections have also been plotted against the Q-values for the reactions. This is a useful comparison to make as higher cross sections make reactions more likely, so deviations from this trend are noteworthy and may suggest changes in the structure of the projectile.

6.4.1 Single neutron knockout

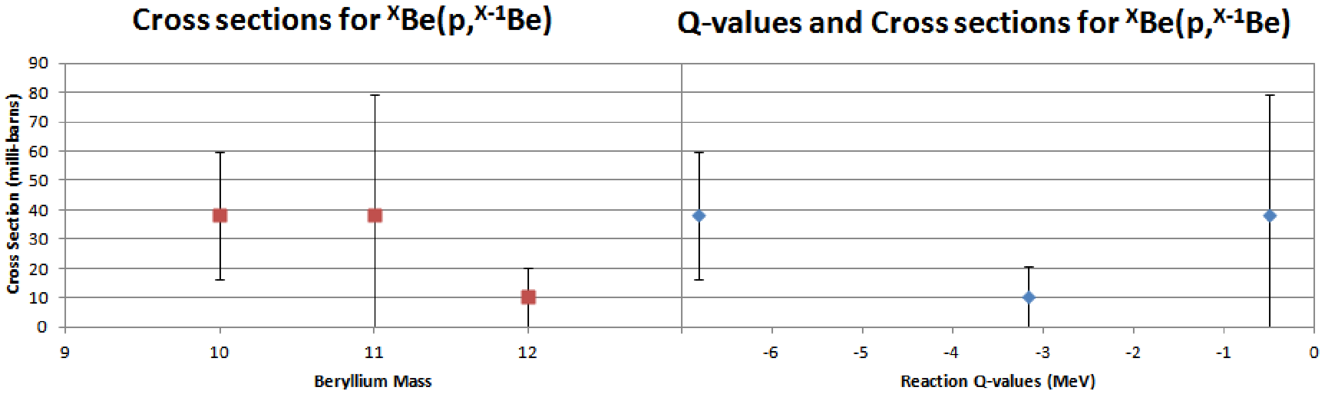

Figure 6.19: Cross sections and Q-values for single neutron knockout for $^{10-12}$Be *on a proton target.*

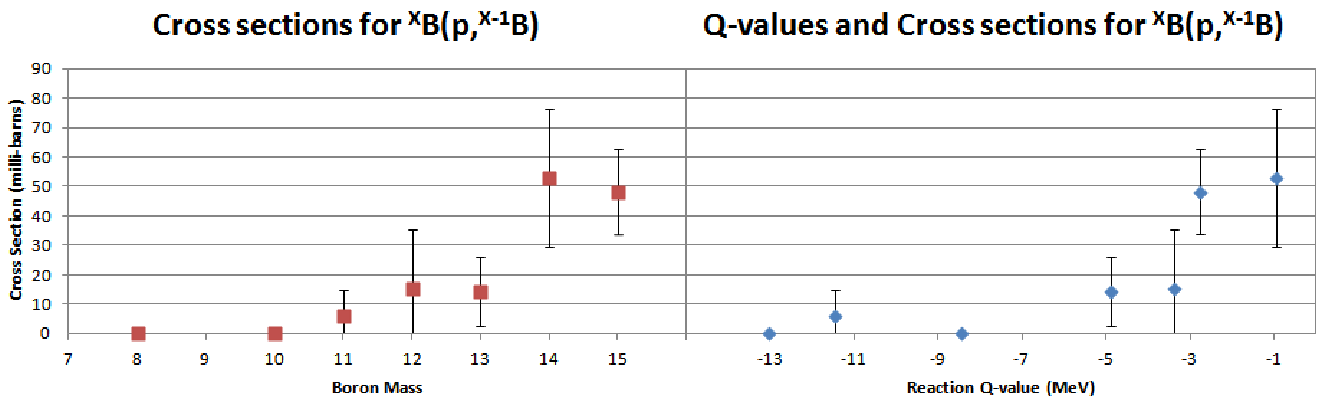

Figure 6.20: Cross sections and Q-values for single neutron knockout for $^{8,10-15}$B *on a proton target.*

Figures 6.19 and 6.20 show cross sections and reaction Q-values for single neutron knockout from isotopes of boron and beryllium. For boron there may be a positive correlation between mass and cross section, and between Q-value and cross section. This is not seen for beryllium.

6.4.2 Single proton knockout

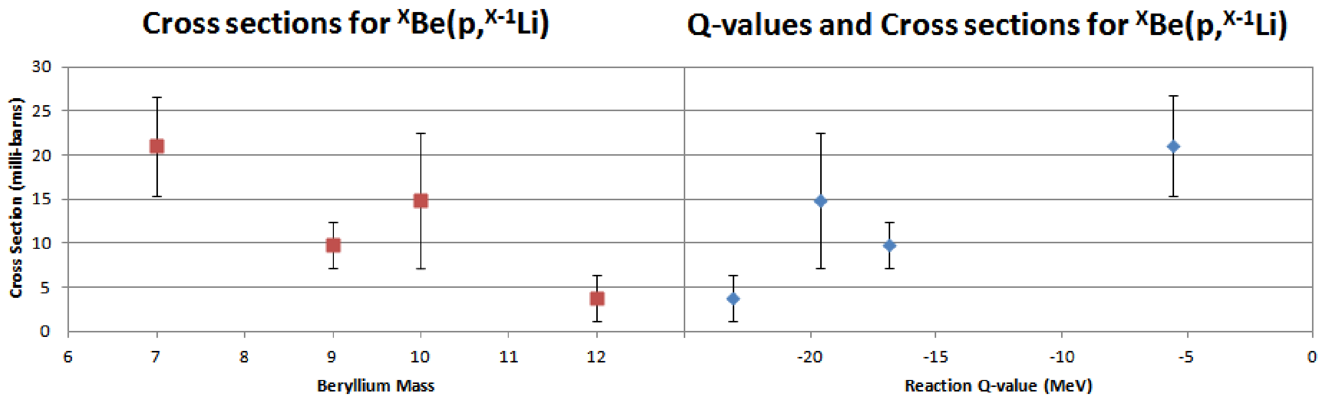

Figure 6.21: Cross sections and Q-values for single proton knockout for ^{7,9,10,12}Be *on a proton target.*

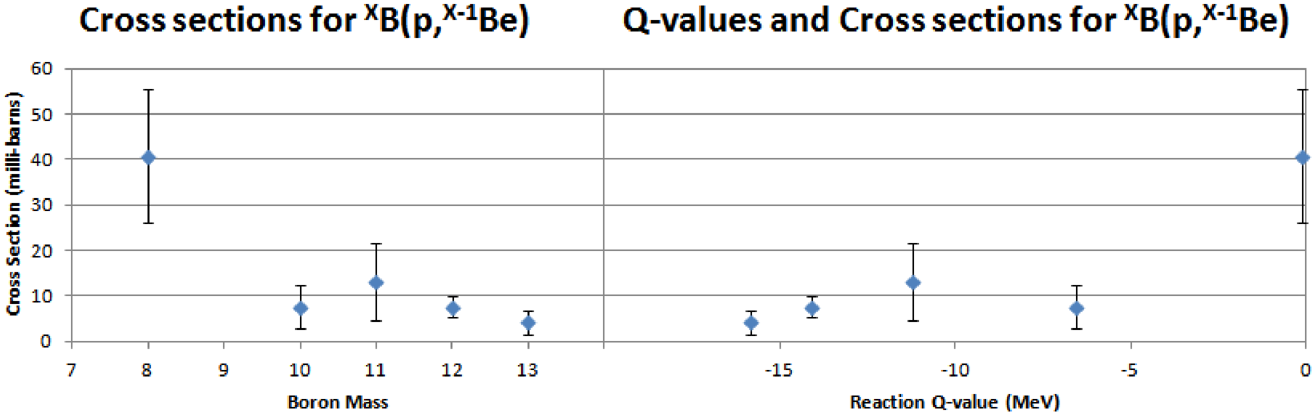

Figure 6.22: Cross sections and Q-values for single proton knockout for ^{8,10,11,13}B *on a proton target.*

Figures 6.21 and 6.22 show cross sections and reaction Q-values for proton knockout from isotopes of beryllium and boron. In both cases there appears to be a negative correlation between mass and cross section, and a positive correlation between Q-value and cross section.

Beam	Energy (MeV)	Cross Section (milli-barns)	Source
8B	640	130 ± 11	[77]
8B	1136	109 ± 1	[78]
8B	2280	89 ± 2	[78]
8B	7488	94 ± 9	[79]
8B	11520	96 ± 3	[80]
8B	3420	38 ± 12	This work
10B	14500	17 ± 2	[80]
10B	2910	11 ± 3	This work

Table 6.1: Cross sections for single proton knockout from ^{8}B *and* ^{10}B *on a* ^{12}C *target at a variety of energies.*

Table 6.1 shows a comparison between the results of this work and existing measurements for single proton knockout from ^{8}B and ^{10}B on a ^{12}C target. It should be noted that errors from [78] are statistical only. For ^{10}B the energy difference far exceeds the energy comparison investigated in Section 6.3; the values are within two sigma. The cross sections for ^{8}B are shown as a function of energy in Figure 6.23. The cross section of this work is substantially lower than the previously exising measurements. In this energy region, cross sections are expected to be almost completely energy independent. As such this discrepancy may indicate a systematic error in the current analysis, but the origin of this has not been identified, and, given the general agreement of results shown in Section 6.3, such a systematic error would not invalidate the present investigation of comparing cross sections with changing neutron number.

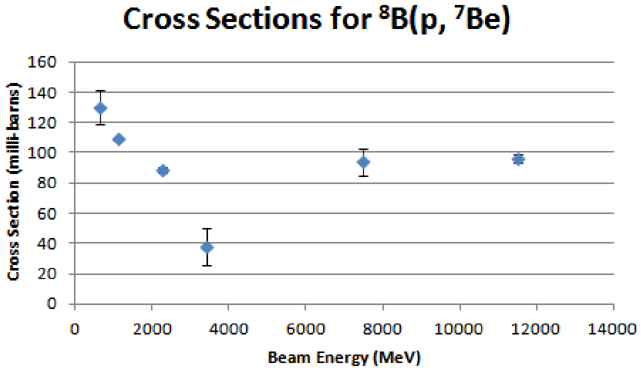

Figure 6.23: Cross sections for single proton knockout from ^{8}B on a ^{12}C target at a variety of energies.

6.4.3 α cluster knockout

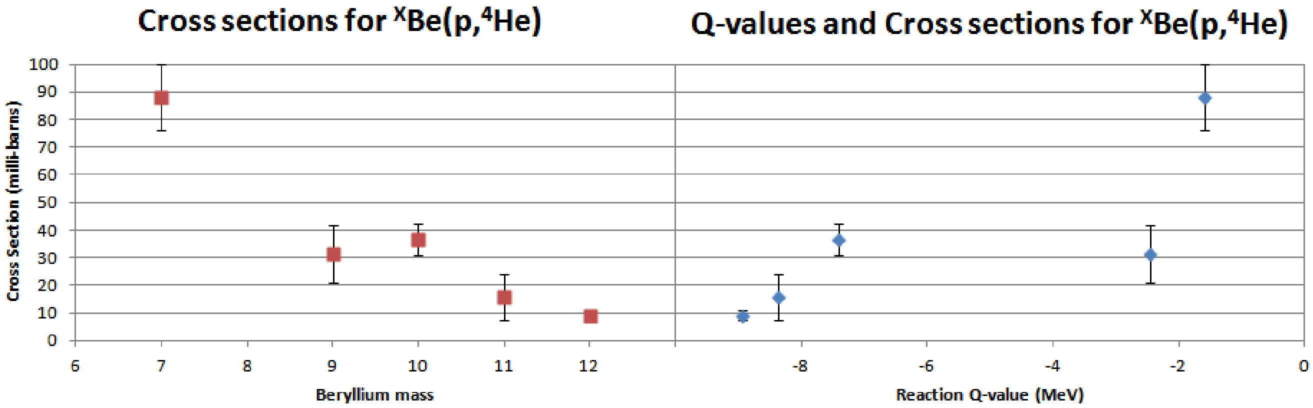

Figure 6.24: Cross sections and Q-values for α cluster knockout for $^{7,9-12}$Be on a proton target.

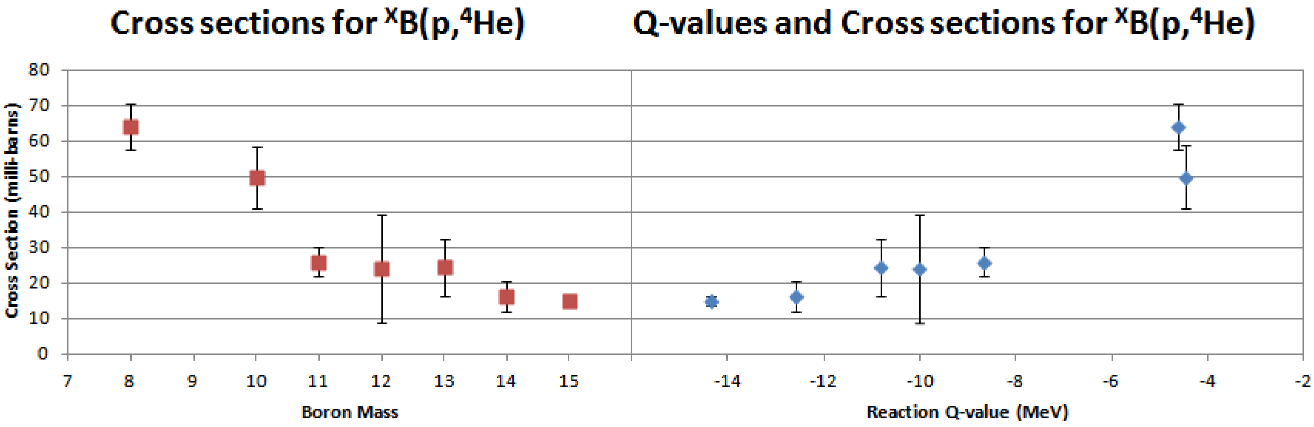

Figure 6.25: Cross sections and Q-values for α cluster knockout for $^{8,10-15}$B *on a proton target.*

Figures 6.24 and 6.25 show the relationship of cross section for alpha cluster knockout with both beam mass and reaction Q-value. For both beryllium and boron there appears to be a negative correlation between mass and cross section, and a positive correlation between Q-value and cross section. As discussed in Section 1.1, the Ikeda model of clustering proposes that clustering will occur with a prominence related to the proximity to the decay threshold for that channel. The positive correlation between Q-value and alpha cluster knockout cross section supports this, as the cluster decay cross sections are higher where less energy is required for the reaction i.e. the Q-value is smaller and so the decay threshold is closer.

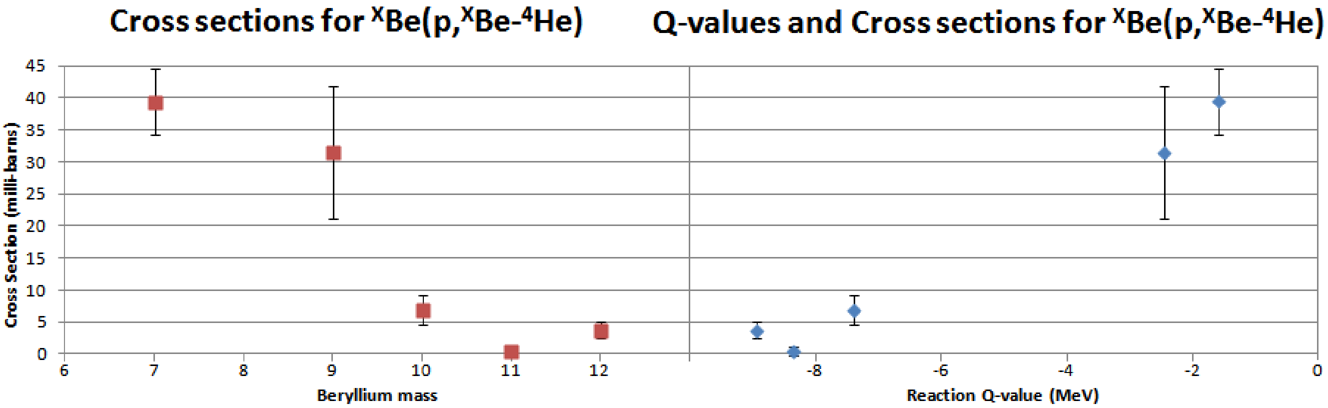

Figure 6.26: Cross sections and Q-values for the remaining fragments after α cluster knockout for $^{7,9-12}$Be *on a proton target.*

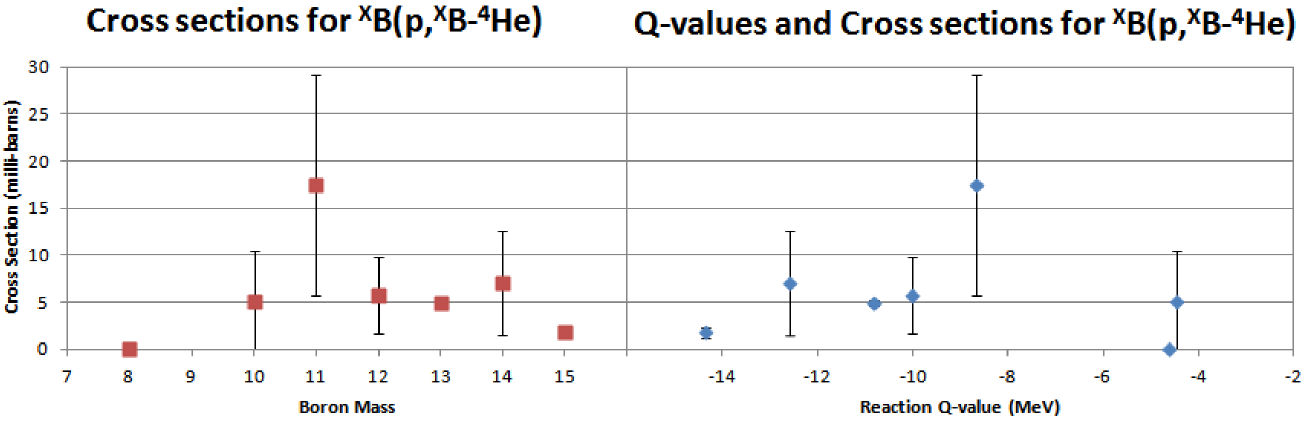

Figure 6.27: Cross sections and Q-values for the remaining fragments after α cluster knockout for $^{8,10,11,13-15}$B *on a proton target.*

Figures 6.26 and 6.27 show the cross sections for the case where the remaining fragment is knocked-out e.g. ^{6}He, where ^{4}He has been knocked-out of ^{10}Be. For beryllium a broadly similar pattern is seen. However, for boron a different pattern is seen with no obvious relation to the ^{4}He knockout.

The α cluster knockout cross sections in Figure 6.24 can be directly compared to the AMD predictions for cluster separation distance in beryllium isotopes, shown in Figure 2.10 since the cross sections and the AMD cluster separations are both measures of the extent of clustering (to clarify, this comparison is not meant to suggest that AMD makes predictions for the α cluster knockout cross sections). Figure 6.28 shows this comparison, with an approximately linear positive correlation, indicating good agreement between the results of this work and the predictions of AMD, with the exception of the cross section for ^{7}Be which is significantly greater than the others. This is a significant observation and a strong indication of clustering in beryllium. Unfortunately a similar graph cannot be plotted for boron. Kanada-En'yo and Horiuchi (in [5]) did not produce a graph similar to Figure 2.10 for boron, due to the more variable nature of their predictions for boron, for example they predicted a three-centre structure for ^{11}B, with a two-centre structure occurring more significantly for ^{17}B and ^{19}B, beyond the scope of this investigation.

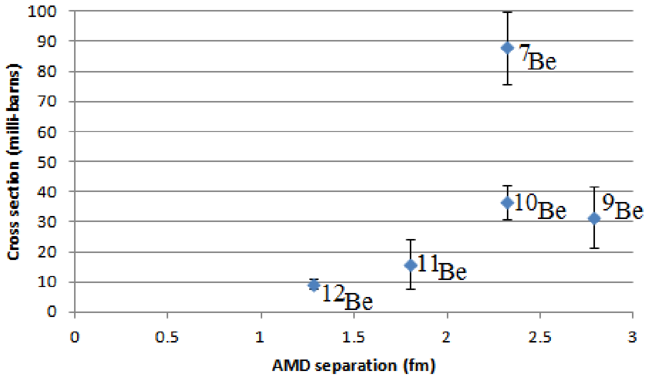

Figure 6.28: A comparison between the cluster separation distances predicted by AMD for beryllium and the extent of clustering estimated by this work via α cluster knockout cross sections.

6.4.4 ^{6}He knockout

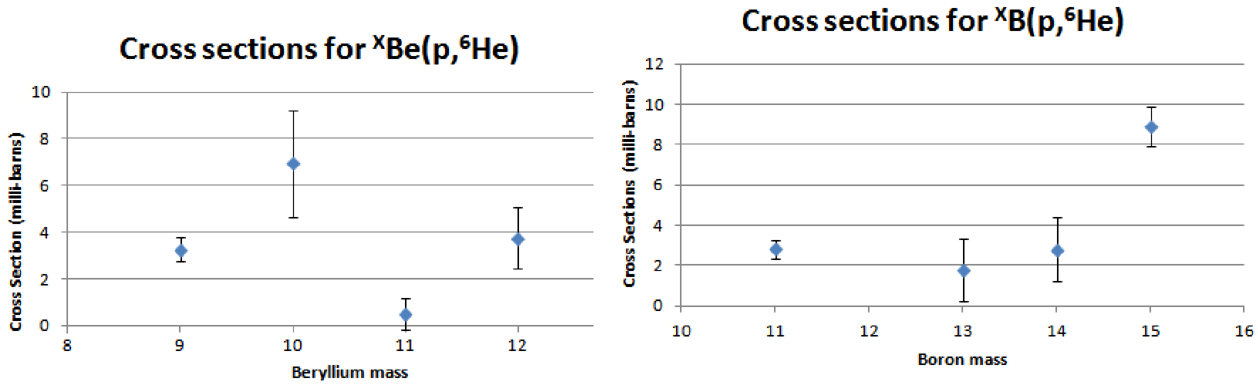

Figure 6.29: Cross sections for knockout of ^{6}He *from* $^{9-12}$Be *and* $^{8,13-15}$B *on a proton target.*

Figure 6.29 shows cross sections for ^{6}He knockout from beryllium and boron on a proton target as a function of projectile mass. In neither case is there a strong correlation.

6.4.5 Total reaction Cross Sections

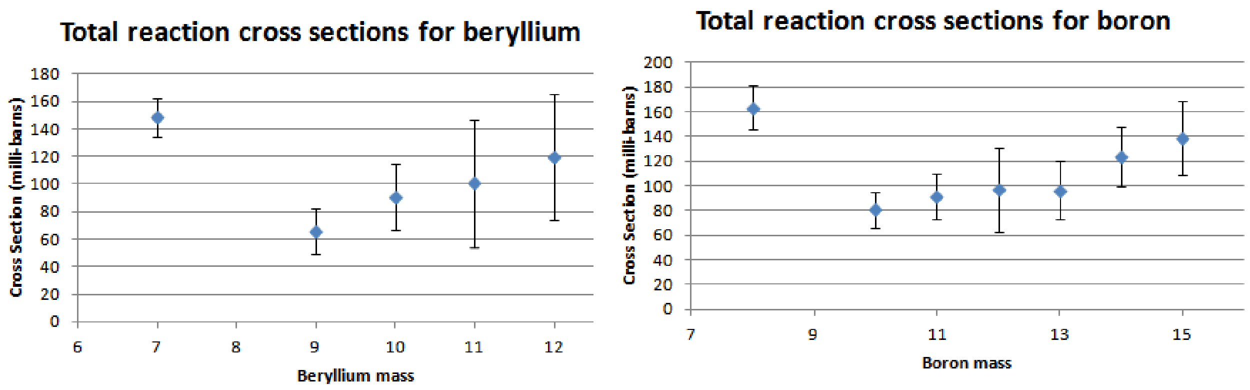

Figure 6.30: Total reaction cross sections for boron and beryllium beams.

Figure 6.30 shows total reaction cross sections for boron and beryllium. For beryllium there is a general positive correlation between mass and cross section, with ^{7}Be being a significant outlier. For boron a positive correlation is also seen, broken by ^{8}B.

6.5 TFW Peak Widths

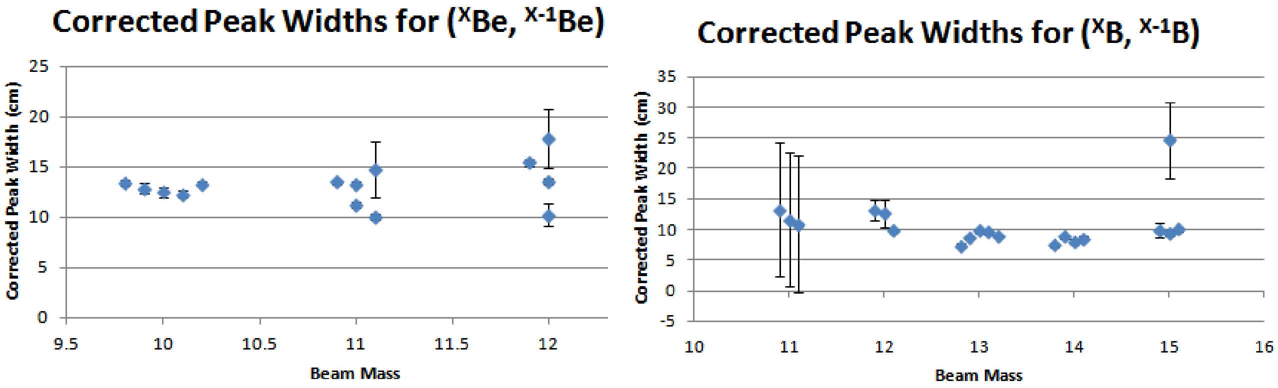

Figure 6.31: TFW peak widths for single neutron knockout from isotopes of boron and beryllium.

Figure 6.31 shows TFW peak widths for single neutron knockout for isotopes of boron and beryllium. In the case of boron there appears to be no correlation between mass and peak width. For beryllium the same may well be true, but there is greater deviation for individual widths.

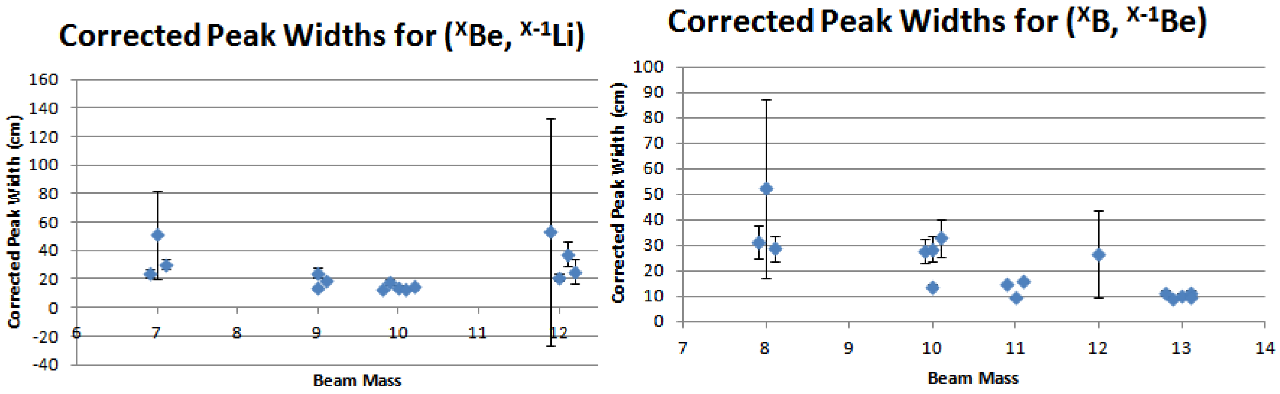

Figure 6.32: TFW peak widths for single proton knockout from isotopes of boron and beryllium.

Figure 6.32 shows TFW peak widths for single proton knockout for isotopes of boron and beryllium. There appears to be a negative correlation between width and mass for boron. An argument can be made for a similar trend in the beryllium data, with the exception of ^{12}Be.

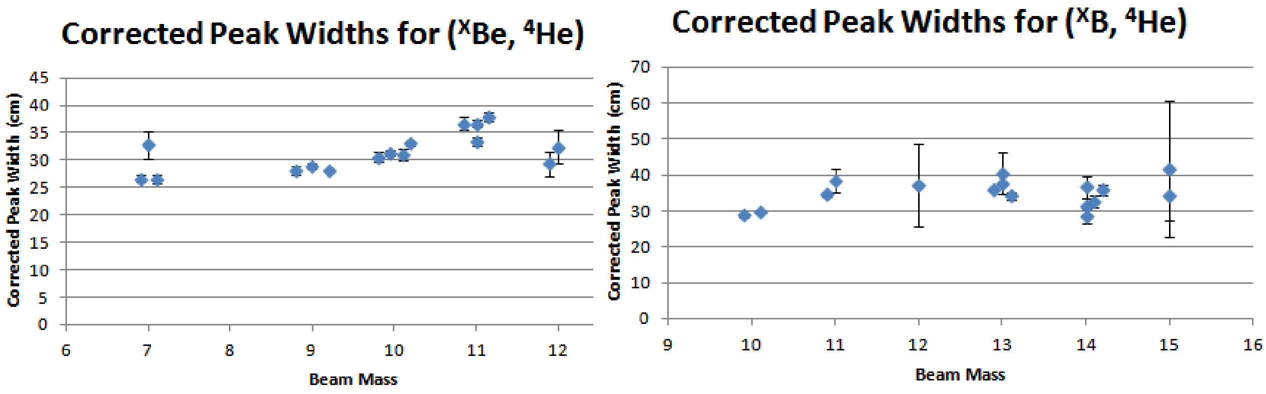

Figure 6.33: TFW peak widths for alpha cluster knockout from isotopes of boron and beryllium.

Figure 6.33 shows TFW peak widths for alpha cluster knockout for isotopes of boron and beryllium. In both cases there appears to be a slight positive correlation between width and mass.

Comparing the widths measured for single nucleon knockout and alpha cluster knockout, it is interesting to note that the widths for neutron knockout are mostly around 10-15 cm, whereas the widths for proton knockout vary mostly between 10 and 30 cm or 25 and 35 cm for alphas. Naively it would be expected that the peak widths for the alphas cluster knockout would be larger than for single nucleon knockout by a factor correlating to the mass difference. This is not the case, suggesting that the dominant mechanism affecting the peak widths is not simply the kinematics i.e. knocking out a heavier particle results in greater perturbation to the remaining fragment.

7 Summary & Future Work

Strong evidence has been presented for breakup cross sections having no energy dependence in the energy region of 260 and 540 MeV per nucleon, for energy differences between 30 and 220 MeV per nucleon.

A strong negative correlation has been found between projectile mass and cluster knockout cross section, and a strong positive correlation between cluster knockout cross section and Q-value for the reaction, for both beryllium and boron, in agreement with the Ikeda model.

A strong positive correlation has been found between alpha cluster knockout cross section and AMD cluster separation distances, with the exception of ^{7}Be, giving support to the AMD cluster model. This relationship is shown in Figure 6.28. With reference to Figure 2.10, a plot of the AMD cluster separation distances, it can be seen that it would be of great value to study the alpha cluster knockout cross sections for ^{13}Be and ^{14}Be; this would allow the relationship between cross section and the AMD cluster separation distances to be examined more closely, especially since ^{13}Be and ^{14}Be represent a change in the trend between AMD cluster separation distances and mass. Unfortunately ^{13}Be is unstable with a half-life of order 10^{-21} seconds, and so unattainable as a beam.

^{7}Be seems anomalous in that it goes against the trends between cross section for ^{4}He knockout and beam mass, in Figure 6.24; AMD cluster separation distances, in Figure 6.28; and total reaction cross section, in Figure 6.30. For all of these comparisons, the cross section in question for ^{7}Be is substantially higher than the trend for the other beam particles would suggest. It is worth noting that, as shown in Figure 6.24, the cross section for ^{4}He knockout is related to the Q-value for the reaction. The Q-value for ^{7}Be breaking into ^{4}He+^{3}He is -1.588 MeV. This is the smallest Q-value of the beryllium isotopes available and is substantially smaller than the nearest Q-value for the equivalent reaction in another isotope: -2.467 MeV for ^{9}Be. This weak binding may be a contributing factor to the high cross section for ^{4}He knockout from ^{7}Be and, since this is the largest component of the total cross section for ^{7}Be, this would also go some way to explaining the higher total cross section for ^{7}Be [81]. However, this is not a complete explanation and requires further investigation.

As discussed in Section 2.10, the experimental setup may allow for a more refined examination of the ground state. In order to ensure that QFS events could be examined, it would be necessary to use the box SSDs and the Crystal Ball to detect the recoiling proton target and knocked-out fragment. The statistics associated with this analysis are limited by the fact that several of the box SSDs were not functioning fully.

Looking forward, the beam production setup at GSI is to be developed into a new setup called the Facility for Antiproton and Ion Research (FAIR). The proposed beam production setup at FAIR, shown in Figure 7.1, offers higher beam intensities, higher beam energies and beam isotopes which are more neutron rich compared to the existing setup. In part these gains come from technical upgrades to the FRS, creating the Super-FRS; further energy increase comes from additional acceleration stages for which the existing stages will become pre-accelerators. The first beam from the Super-FRS at FAIR is expected in 2018.

The R^{3}B experiment will also be significantly upgraded, with a new superconducting dipole magnet, GLAD, and several new detectors designed based on the collaboration's over 20 years of experience using and refining the existing experimental setup. Figure 7.2 shows the proposed setup.

LAND will be replaced with a detector called NeuLAND. NeuLAND offers high resolution and efficiency and the ability to resolve 5 separate neutron events. The role fulfilled by Crystal Ball will be taken over by a detector called CALIFA. CALIFA is a calorimeter array consisting of 1952 Caesium iodide crystals in two sections: a cylindrical barrel (shown in Figure 7.3) and a cap at the forward end. Simulations

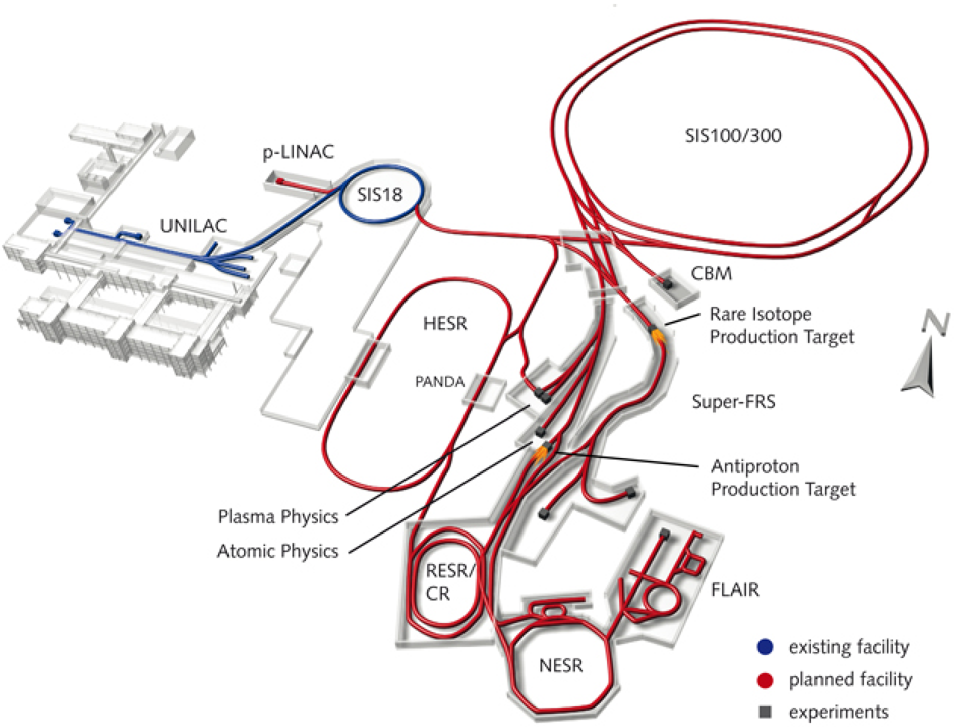

Figure 7.1: The existing and proposed acceleration setup for FAIR at GSI, from [72].

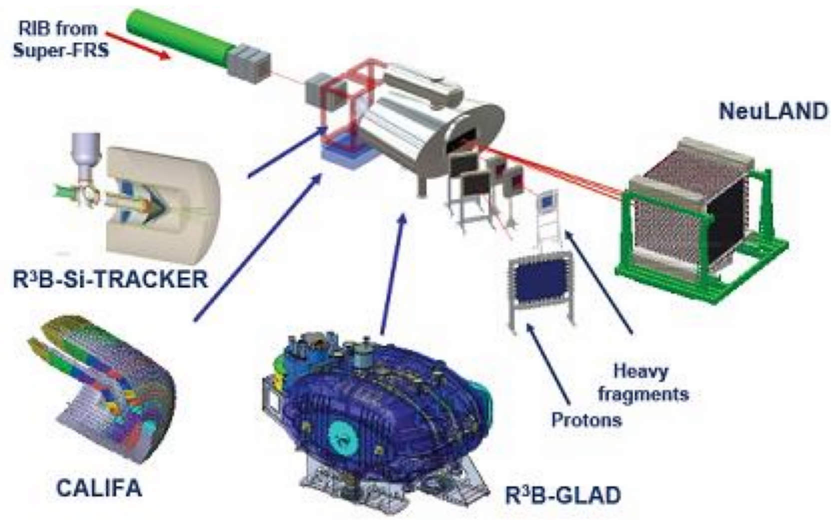

Figure 7.2: The proposed R^3B setup at FAIR, from [74].

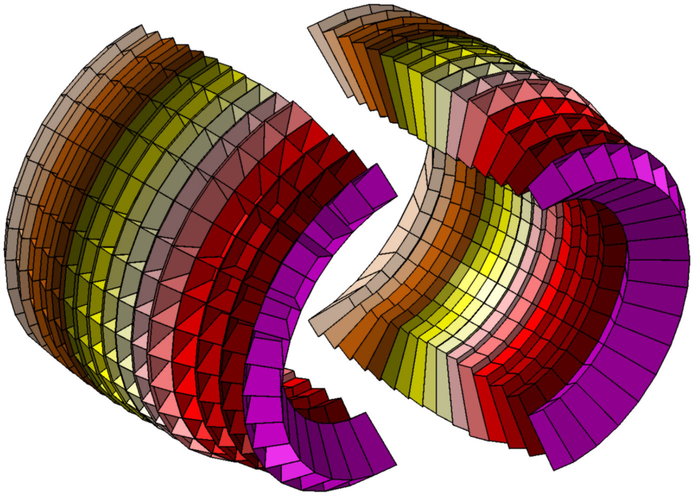

Figure 7.3: The barrel section of CALIFA, from [76]

were performed to optimise the granularity for both energy and angular resolution. Each scintillator crystal will be read out by an Avalanche Photo Diode (APD); APDs have the disadvantage of greater temperature sensitivity when compared to PMTs, but advantages of insensitivity to magnetic fields[6], compact geometry and large dynamic range of light acceptance. This large range is required in order to simultaneously measure low and high energy γ-rays and charged particles[7]. Compared to the Crystal Ball, CALIFA offers improved efficiency, angular resolution and energy resolution.

The SSDs will be replaced with an array of double sided silicon strip detectors called the Silicon Tracker. As shown in Figure 7.4, the Silicon Tracker consists of three concentric cones of detectors. The outer 2 cones form their shape from 12 trapezoidal detectors each, the inner cone uses 6 smaller trapezoids.

The Silicon Tracker will be positioned inside CALIFA and surrounding the target. Figure 7.5 shows the Silicon Tracker in situ.

The cone shape allows the detector surface to be focused at forward angles. The

---

[6] This insensitivity is useful as CALIFA will sit in the fringe of the GLAD's magnetic field.

[7] Crystals have a length such that they can fully stop protons from quasi-free knockout with a beam energy of 700 MeV per nucleon.

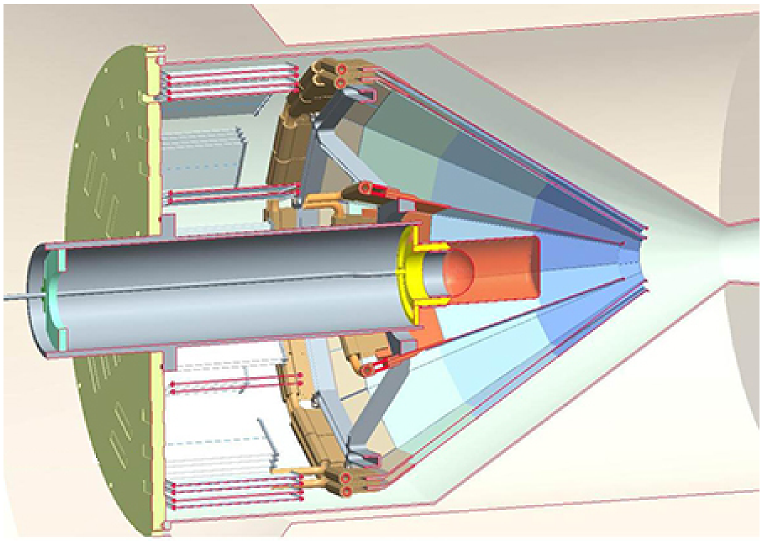

Figure 7.4: A schematic of the Silicon Tracker, from [73].

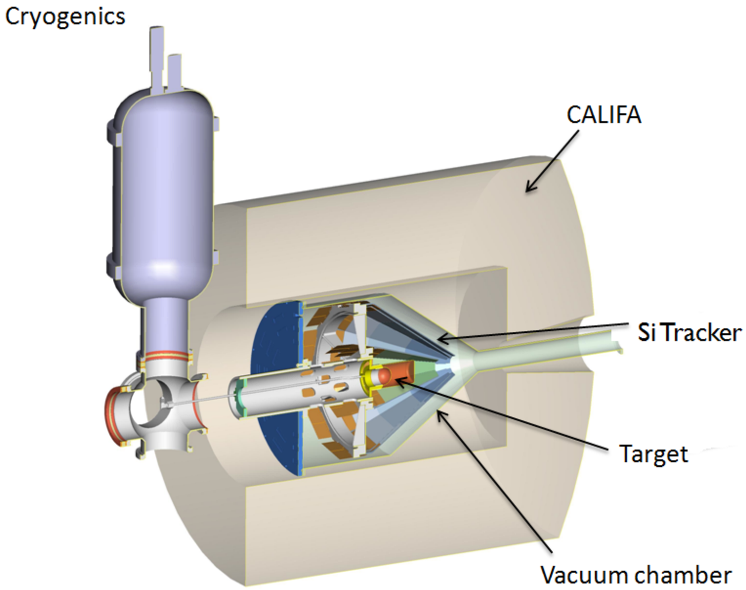

Figure 7.5: A schematic of the Silicon tracker in with CALIFA, adapted from [75].

inner cone is positioned as close as possible to the target, and the distance to the outer rings is maximised - this improves the resolution of the measurement of outgoing angle. The 3 layer design also provides redundancy, as a guard against strip failure. The inner layer has been designed to be as thin as possible to allow for an energy loss measurement with a minimum of energy and angular straggling, and a low minimum energy for charged particles not being stopped i.e. continuing to the outer layer to allow an angular measurement.

The features of this new setup will be ideal for conducting further experiments to build on the results of this work. The Silicon Tracker and CALIFA will allow a more precise examination of ground state clustering, using the method described in Section 2.10. This approach will also be aided by the higher beam intensity as greater statistics may well be required. Higher beam intensities will also make it possible to make measurements at a greater variety of energies by reducing the required beam time for a given measurement; this will allow for a more thorough investigation into the effects of energy on cross section, and also a clearer comparison of cross sections for cluster knockout between isotopes of varying neutron number.

Appendices

A Deformed Harmonic Oscillator & Two Centre Harmonic Oscillator code

The following code was used to calculate the density distributions for the Deformed Harmonic Oscillator (DHO) and Two Centre Harmonic Oscillator (TCHO) discussed in Sections 2.1 and 2.2. In this form the output will be the DHO density for ^{9}Be with a (010) neutron, as shown in Figure 2.2. This can be easily adjusted by changing the sum in the output line to the desired configuration. For example, to calculate the Hückel method density distribution of ^{10}Be with two neutrons in the σ-type configuration, the line must be changed to "A000_A000 + 2 * Huckel_N001u". The required calculations for these contributions must also be uncommented since those not required have been commented out for speed of calculation.

```cpp
#include <iostream>
#include <fstream>
#include <cmath>
using namespace std;

// 3D and 1D SHO and Huckel Wavefunctions
double SHO_wvfn3D(const double x, const double y, const double z, const int n_x, const int n_y, const int n_z, const double mu);
double SHO_wvfn1D(const double r, const int n, const double mu);
double Huckel_wvfn3D(const double x, const double y, const double z, const int n_x, const int n_y, const int n_z);
double Huckel_wvfn1D(const double r, const int n);

// Supporting functions.
double  H(const int n, const double r); // Hermite Polynomials. (Note: hard coded, n<6).
int     factorial(const int num);       // Calculates factorials.

// Constants. Some set to 1 for simplicity.
const double hbar = 1;//1.055 * pow(10., -34);
const double pi = 3.141592;
const double m_p = 1;//1.672621637 * pow(10., -27);
const double m_n = 1;//1.67492729 * pow(10., -27);
const double omega = 1;//2.24 * pow(10., 22);
const double R1 = 0.8163 ;//* pow(10., -15);
const double R2 = -R1;

// Range and increment of calculation.
const double min_range = -5 ;//* pow(10., -15);
const double max_range = -min_range;
const int steps = 500;
const double step = (max_range - min_range) / steps;

int main()
{
    double y, z, x = min_range;

    double A000_A001, SHO_N002, SHO_N010;
    double A000_A000, Huckel_N001g, Huckel_N001u, Huckel_N002g, Huckel_N002u, Huckel_N010g, Huckel_N010u;

    ofstream out;
    out.open("density_out.txt");

    for (int i=0; i < steps; i++)
    {
        y = min_range + (i * step);

        for (int j=0; j < steps; j++)
        {
            z = min_range + (j * step);

            // SHO general calculations (wavefunctions squared to get density distributions)
            A000_A001 = 2 * pow(fabs(SHO_wvfn3D(x,y,z,0,0,0, m_p)), 2) + 2 * pow(fabs(SHO_wvfn3D(x,y,z,0,0,0, m_n)), 2)
                        + 2 * pow(fabs(SHO_wvfn3D(x,y,z,0,0,1, m_p)), 2) + 2 * pow(fabs(SHO_wvfn3D(x,y,z,0,0,1, m_n)), 2);
```

```
            //SHO_N002 = pow(fabs(SHO_wvfn3D(x, y, z, 0, 0, 2, m_n)), 2);
            SHO_N010 = pow(fabs(SHO_wvfn3D(x, y, z, 0, 1, 0, m_n)), 2);

            // Huckel Calculations (wavefunctions squared to get density distributions)
            //A000_A000 = 4 * pow(fabs(SHO_wvfn3D(x,y,(z-R1),0,0,0, m_p)), 2)
            //          + 4 * pow(fabs(SHO_wvfn3D(x,y,(z-R2),0,0,0, m_n)), 2);
            //Huckel_N001g = pow(fabs(Huckel_wvfn3D(x, y, (z-R1), 0, 0, 1) + Huckel_wvfn3D(x, y, (z-R2), 0, 0, 1)), 2);
            //Huckel_N001u = pow(fabs(Huckel_wvfn3D(x, y, (z-R1), 0, 0, 1) - Huckel_wvfn3D(x, y, (z-R2), 0, 0, 1)), 2);
            //Huckel_N002g = pow(fabs(Huckel_wvfn3D(x, y, (z-R1), 0, 0, 2) + Huckel_wvfn3D(x, y, (z-R2), 0, 0, 2)), 2);
            //Huckel_N002u = pow(fabs(Huckel_wvfn3D(x, y, (z-R1), 0, 0, 2) - Huckel_wvfn3D(x, y, (z-R2), 0, 0, 2)), 2);
            //Huckel_N010g = pow(fabs(Huckel_wvfn3D(x, y, (z-R1), 0, 1, 0) + Huckel_wvfn3D(x, y, (z-R2), 0, 1, 0)), 2);
            //Huckel_N010u = pow(fabs(Huckel_wvfn3D(x, y, (z-R1), 0, 1, 0) - Huckel_wvfn3D(x, y, (z-R2), 0, 1, 0)), 2);

            // Output calculated value.
            out << A000_A001 + SHO_N010;
            out << endl;
        }
    }

    out.close();
    out.clear();
}
// End of main.

double SHO_wvfn3D(const double x, const double y, const double z, const int n_x, const int n_y, const int n_z, const double mu)
{
    return SHO_wvfn1D(x, n_x, mu) * SHO_wvfn1D(y, n_y, mu) * SHO_wvfn1D(z, n_z, mu);
}

double SHO_wvfn1D(const double r, const int n, const double mu)
{
    // Initial prefactor, function only of n.
    double ans = sqrt(1 / (pow(2., n) * factorial(n)));

    // Second prefactor, based only on constants.
    ans = ans * pow((mu * omega / (pi * hbar)), 0.25);

    // Hermite Polynomial
    ans = ans * H(n, (sqrt(mu * omega / hbar) * r));

    // Exponential.
    ans = ans * exp(- mu * omega * pow(r, 2) / (2 * hbar));

    return ans;
}

double Huckel_wvfn3D(const double x, const double y, const double z, const int n_x, const int n_y, const int n_z)
{
    return Huckel_wvfn1D(x, n_x) * Huckel_wvfn1D(y, n_y) * Huckel_wvfn1D(z, n_z);
}
```

```
double Huckel_wvfn1D(const double r, const int n)
{
    double pf, ans;

    // Initial prefactor, function only of n.
    pf = sqrt(1/2.0) * sqrt(1 / (pi * pow(2., n) * factorial(n)));

    ans = pf * H(n, (sqrt(m_n * omega / hbar) * r)) * exp(-omega * pow(r, 2) / 2);

    return ans;
}

double  H(const int n, const double r)
{
    double h;

    if ((n < 0) || n > 5)
    {
        printf("Error in function H, n (%d) must be between 0 and 5.\n", n);
    }

    if (n == 0)
        h = 1;

    if (n == 1)
        h = 2 * r;

    if (n == 2)
        h = (4 * pow(r, 2)) - 2;

    if (n == 3)
        h = (8 * pow(r, 3)) - (12 * r);

    if (n == 4)
        h = (16 * pow(r, 4)) - (48 * pow(r, 2)) + 12;

    if (n == 5)
        h = (32 * pow(r, 5)) - (160 * pow(r, 3)) + (120 * r);

    return h;
}

int     factorial(const int num)
{
    int ans = 1;

    for (int i=0; i < (num - 1); i++)
        ans = ans * (i + 2);

    return ans;
}
```

B Deformed Harmonic Oscillator Plots for beryllium isotopes

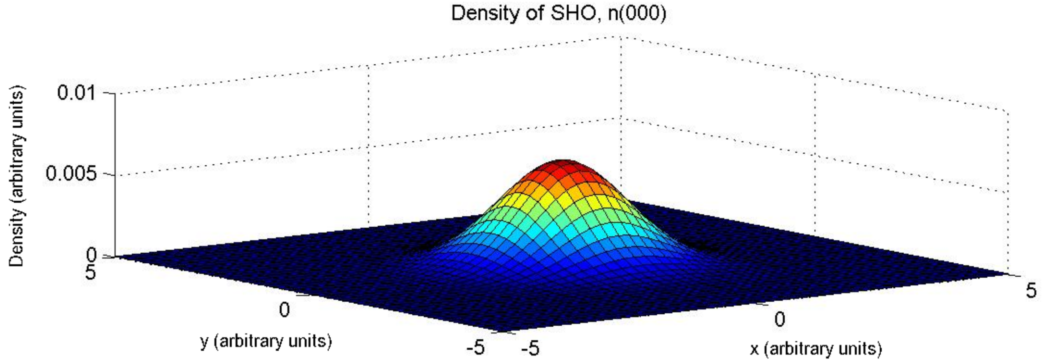

Figure B.1: The density distribution of a (000) neutron, calculated using the DHO.

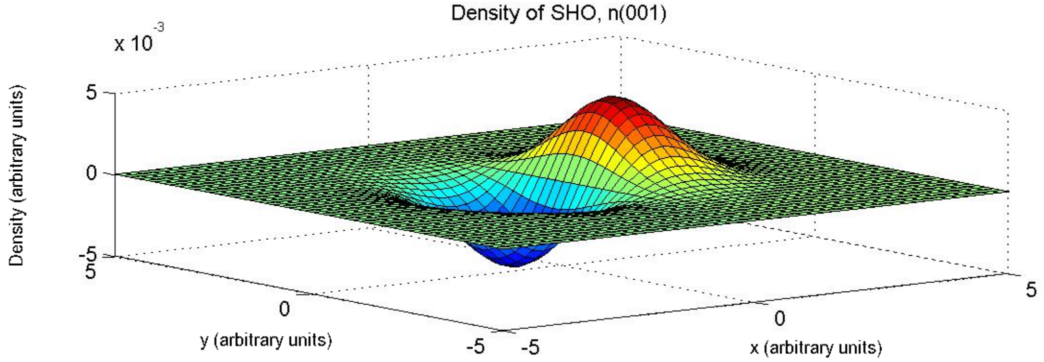

Figure B.2: The density distribution of a (001) neutron, calculated using the DHO.

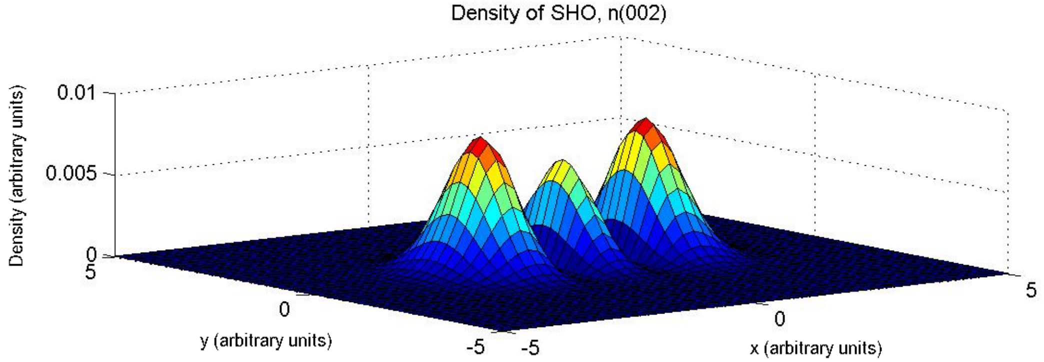

Figure B.3: The density distribution of a (002) neutron, calculated using the DHO.

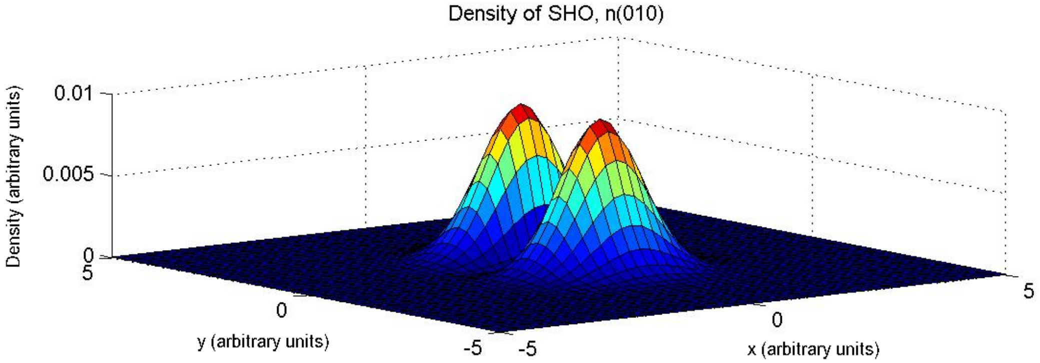

Figure B.4: The density distribution of a (010) neutron, calculated using the DHO.

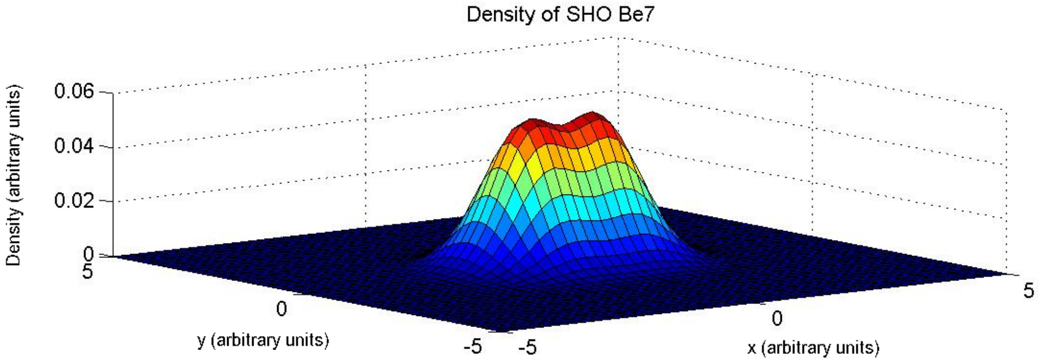

Figure B.5: The density distribution of ^{7}Be*, calculated using the DHO.*

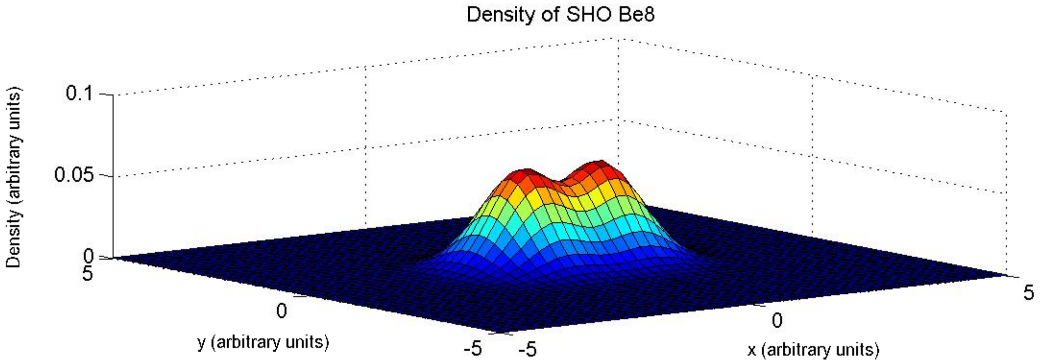

Figure B.6: The density distribution of ^{8}Be*, calculated using the DHO.*

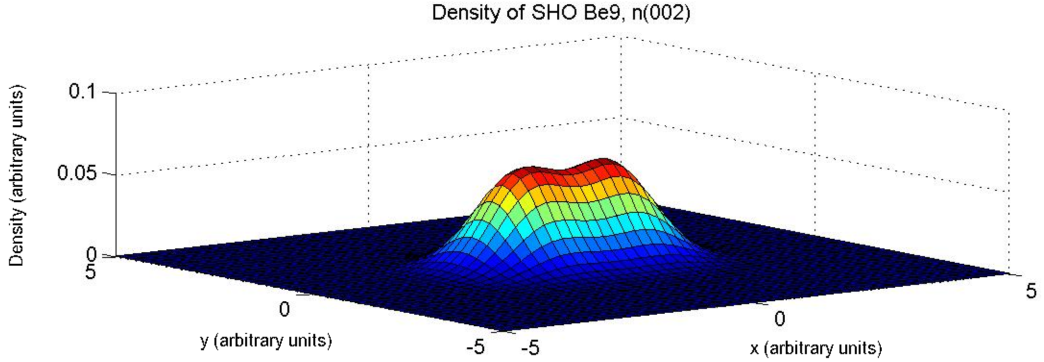

Figure B.7: The density distribution of $^{9}\mathrm{Be}$ *with a (002) neutron, calculated using the DHO.*

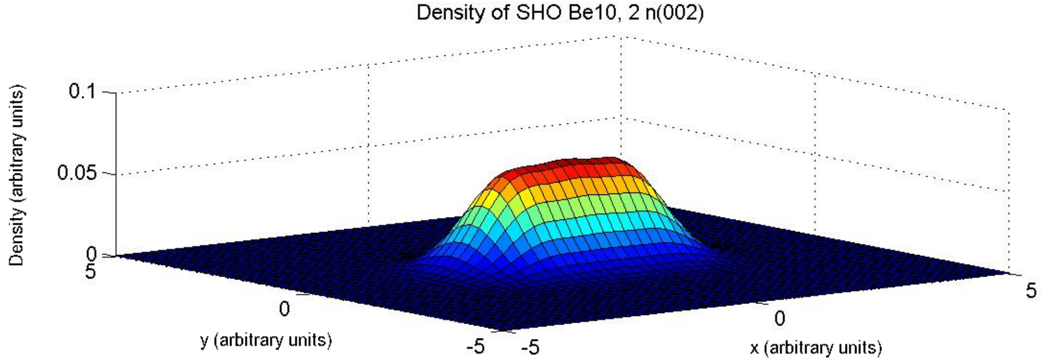

Figure B.8: The density distribution of $^{10}\mathrm{Be}$ *with two (002) neutrons, calculated using the DHO.*

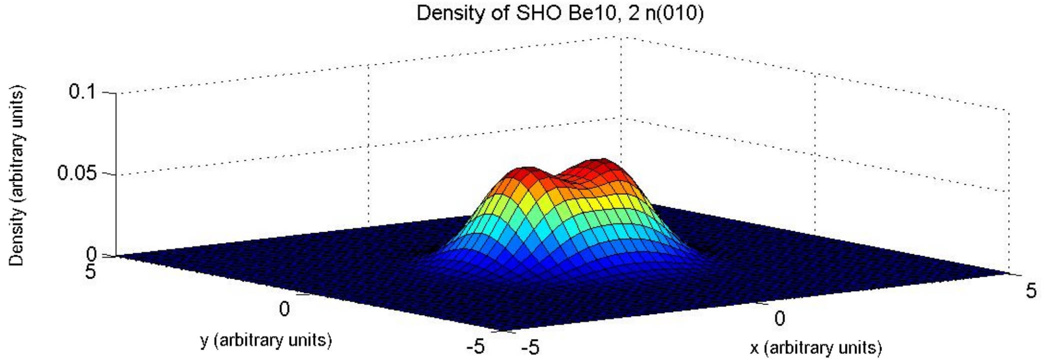

Figure B.9: The density distribution of $^{10}\mathrm{Be}$ *with two (010) neutrons, calculated using the DHO.*

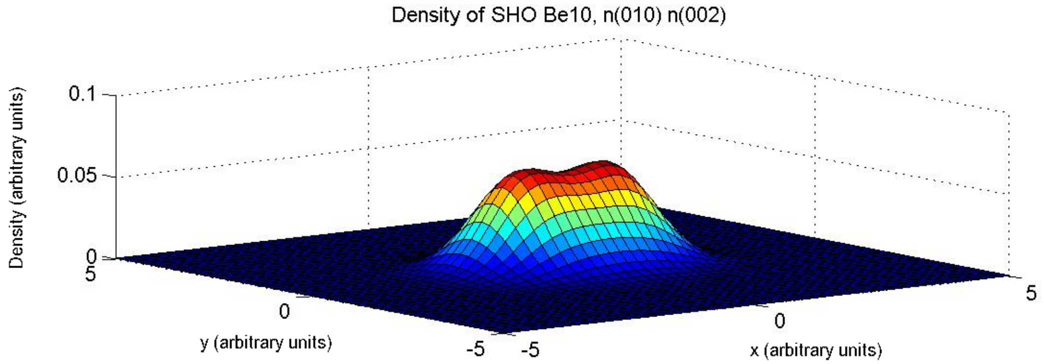

Figure B.10: The density distribution of ^{10}Be *with a (010) neutron and a (002) neutron, calculated using the DHO.*

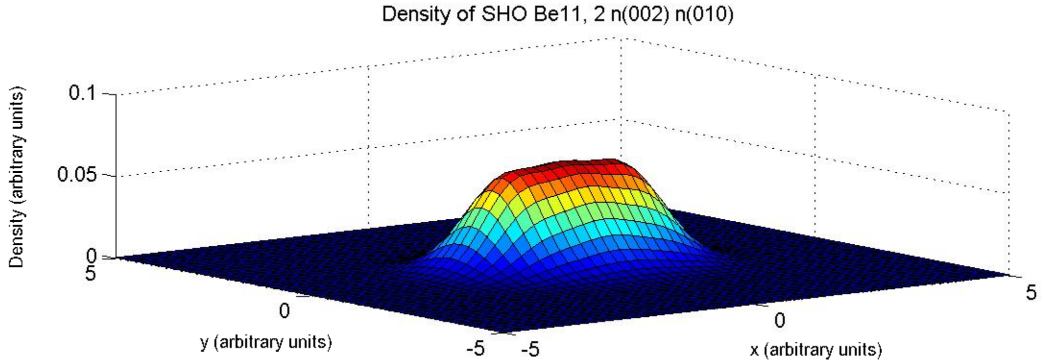

Figure B.11: The density distribution of ^{11}Be *with two (002) neutrons and a (001) neutron, calculated using the DHO.*

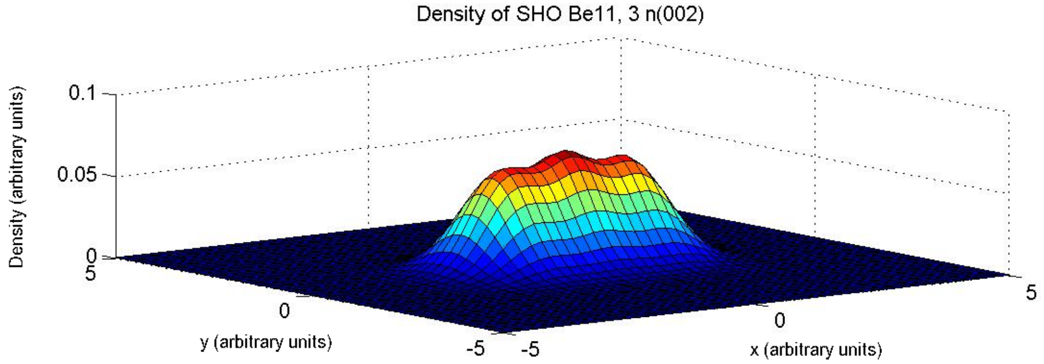

Figure B.12: The density distribution of ^{11}Be *with three (002) neutrons, calculated using the DHO.*

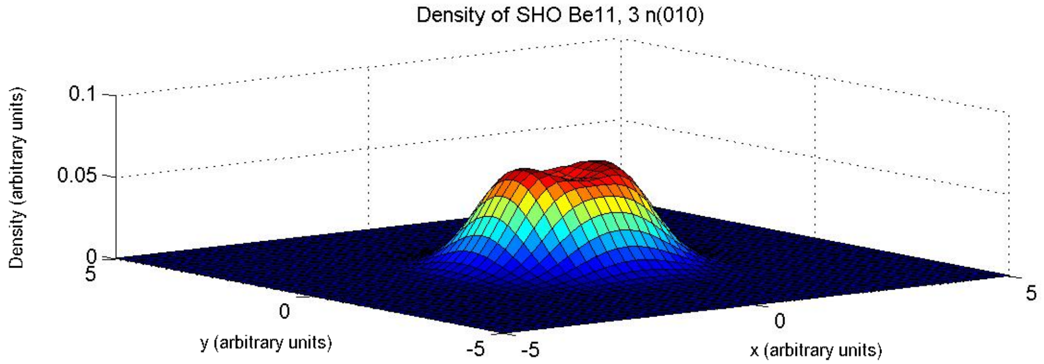

Figure B.13: The density distribution of ^{11}Be *with three (010) neutrons, calculated using the DHO.*

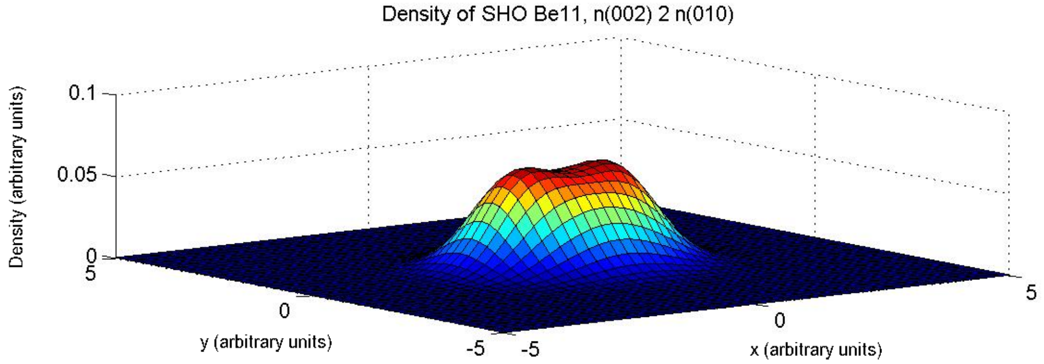

Figure B.14: The density distribution of ^{11}Be *with a (002) neutron and two (010) neutrons, calculated using the DHO.*

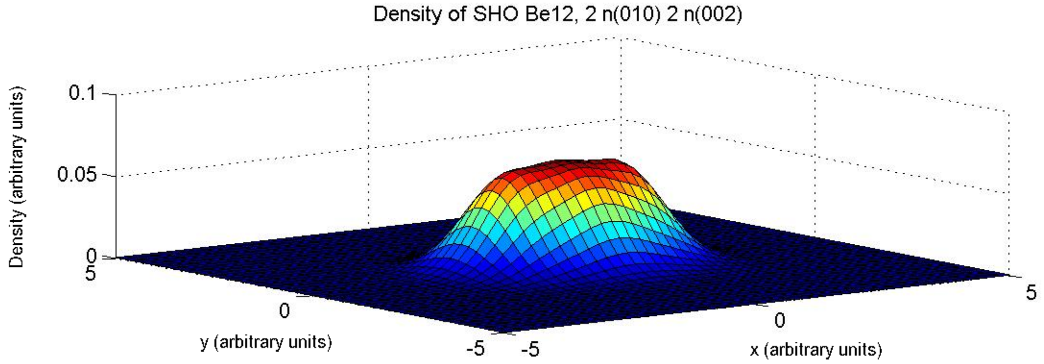

Figure B.15: The density distribution of ^{12}Be *with two (010) neutrons and two (002) neutrons, calculated using the DHO.*

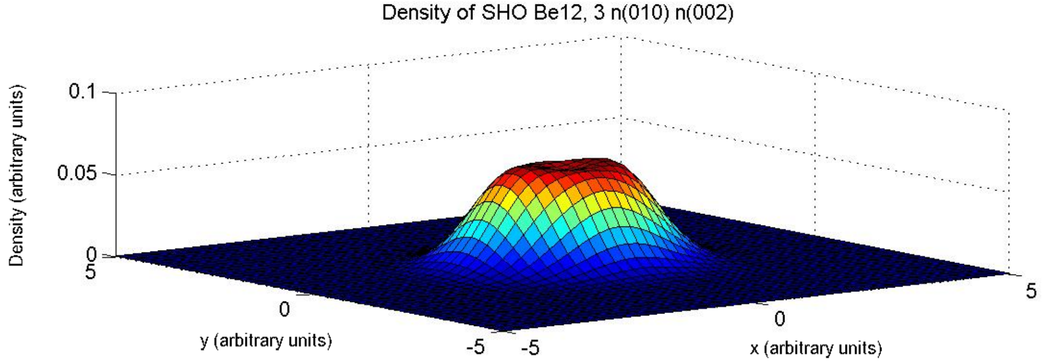

Figure B.16: The density distribution of ^{12}Be *with three (010) neutrons and a (002) neutron, calculated using the DHO.*

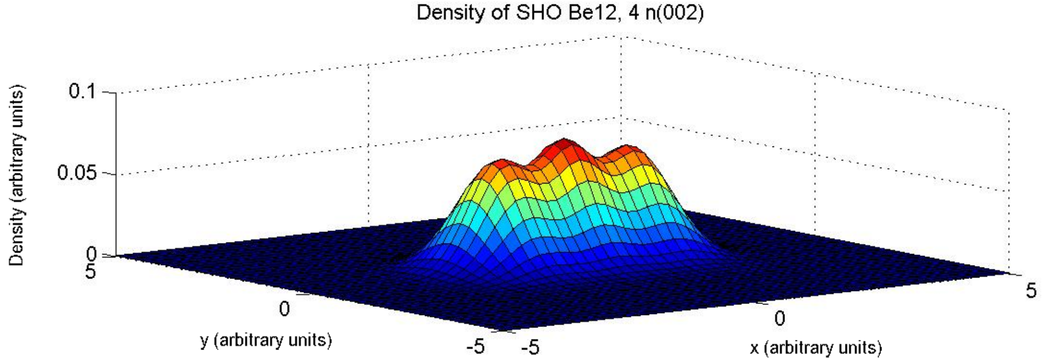

Figure B.17: The density distribution of ^{12}Be *with four (002) neutrons, calculated using the DHO.*

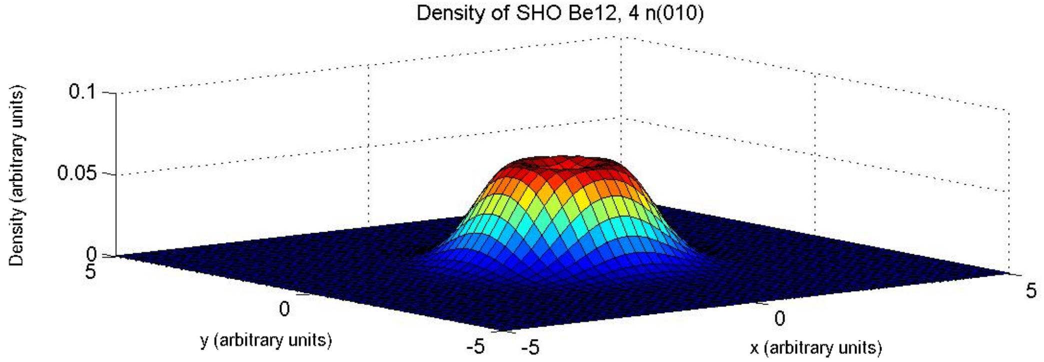

Figure B.18: The density distribution of ^{12}Be *with four (010) neutrons, calculated using the DHO.*

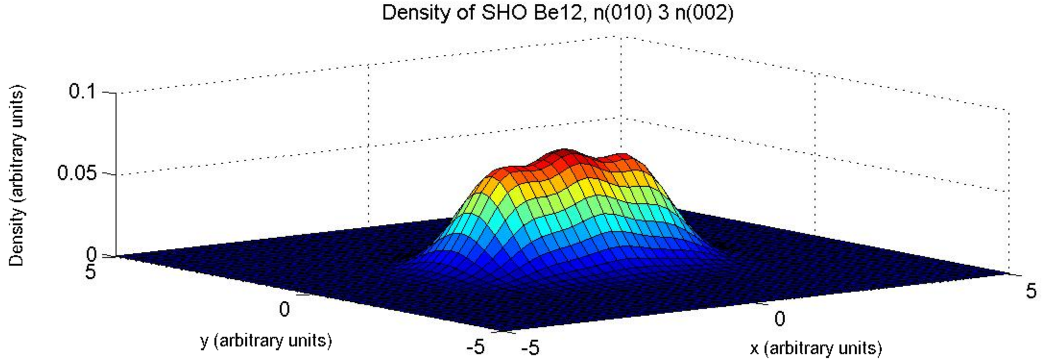

Figure B.19: The density distribution of ^{12}Be *with a (010) neutron and three (002) neutrons, calculated using the DHO.*

C Two Centre Harmonic Oscillator Plots for beryllium isotopes

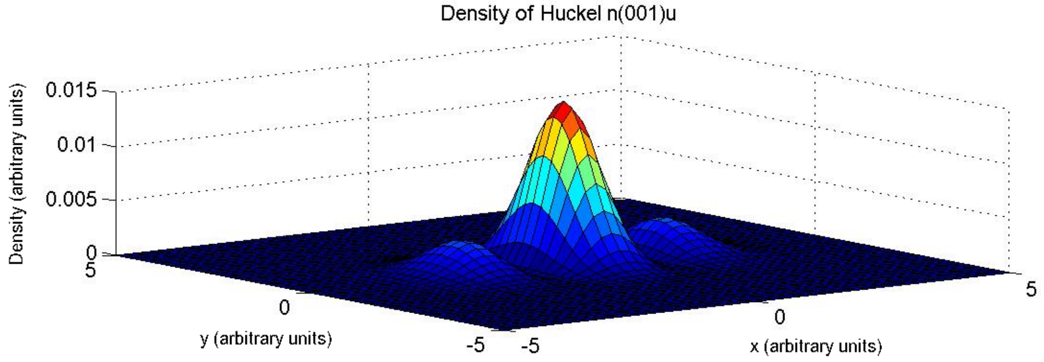

Figure C.1: The Hückel method density distribution of a neutron in the σ-type configuration

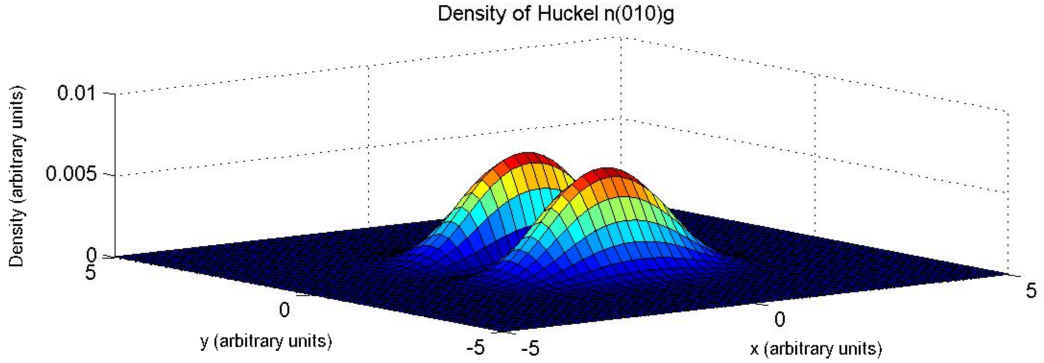

Figure C.2: The Hückel method density distribution of a neutron in the π-type configuration

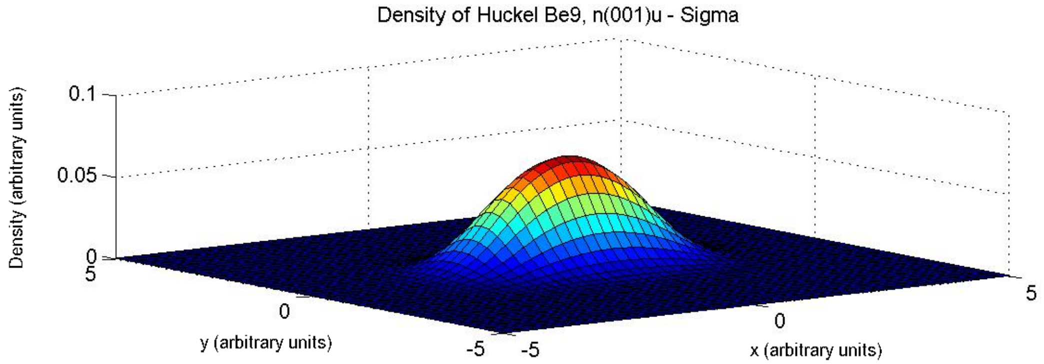

Figure C.3: The Hückel method density distribution of ^{9}Be *with a neutron in the* σ*-type configuration*

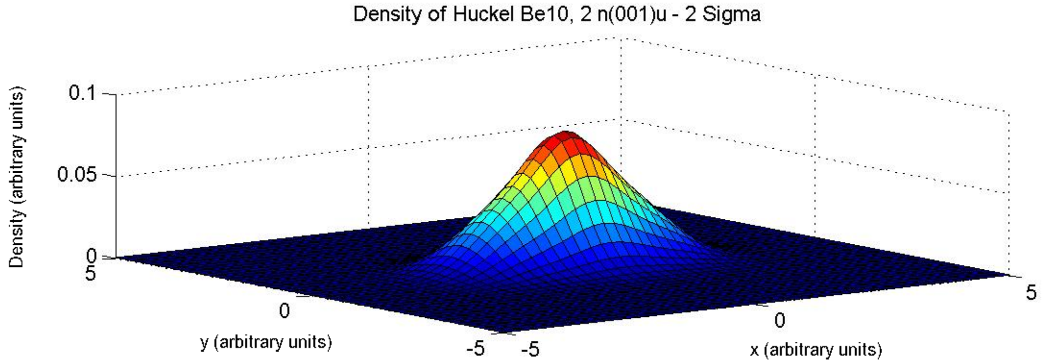

Figure C.4: The Hückel method density distribution of ^{10}Be *with two neutrons in the* σ*-type configuration.*

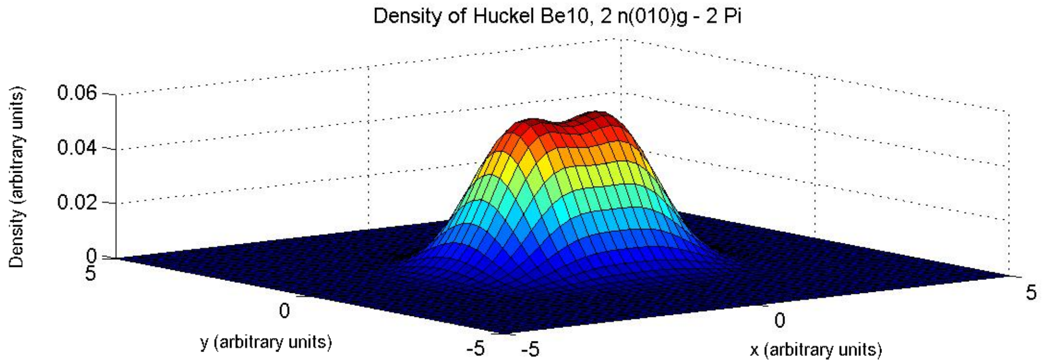

Figure C.5: The Hückel method density distribution of ^{10}Be *with two neutrons in the* π*-type configuration.*

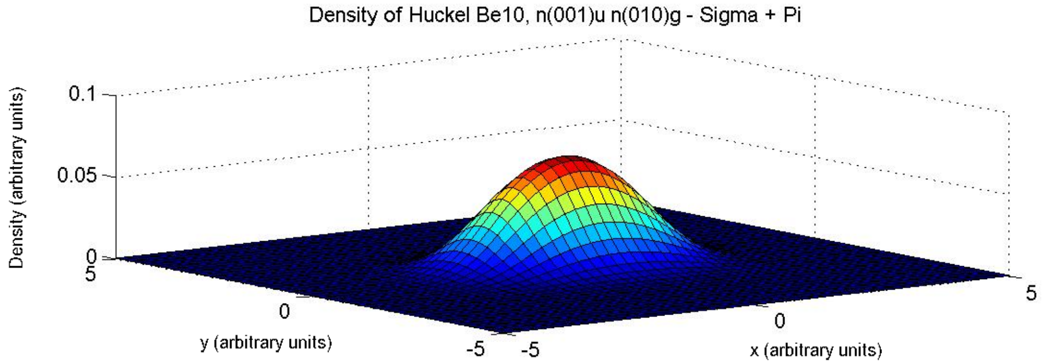

Figure C.6: The Hückel method density distribution of ^{10}Be *with a neutron in the* π*-type configuration and a neutron in the* σ*-type configuration*

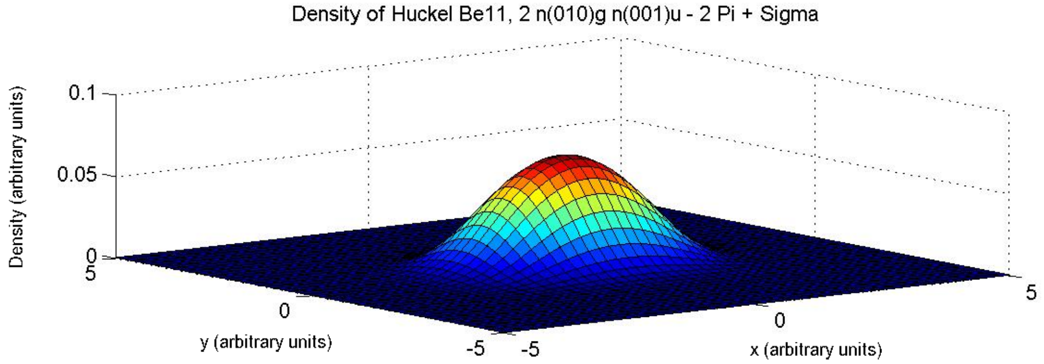

Figure C.7: The Hückel method density distribution of ^{11}Be *with two neutrons in the* π*-type configuration and a neutron in the* σ*-type configuration.*

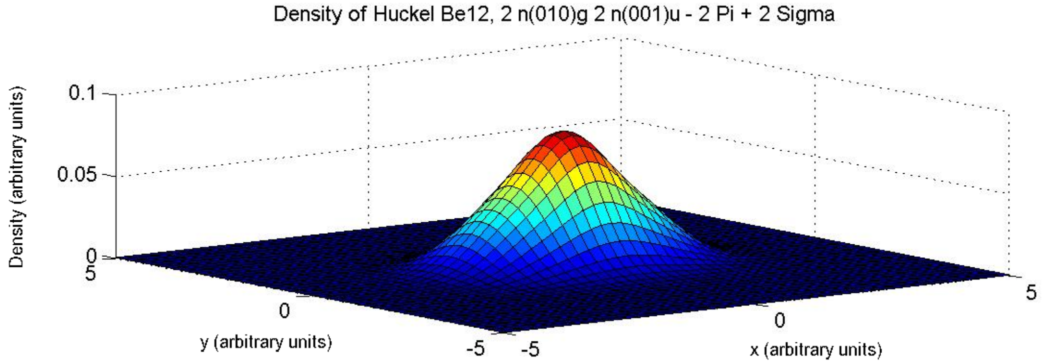

Figure C.8: The Hückel method density distribution of ^{12}Be *with two neutrons in the* π*-type configuration and two neutrons in the* σ*-type configuration*

D Efficiency values

Run	Energy (MeV)	Target	Beam	Efficiency for fragment charge		
				2	3	4
500	2569	Carbon	^{7}Be	0.7173 ± 0.0409	0.8912 ± 0.1071	0.9981 ± 0.0133
497	2569	Polyethylene	^{7}Be	0.7529 ± 0.0676	0.9183 ± 0.0559	0.9976 ± 0.0081
499	2569	Polyethylene	^{7}Be	0.7390 ± 0.0620	0.9452 ± 0.0635	0.9972 ± 0.0088
452	2932	Carbon	^{11}Be	0.5421 ± 0.0376	0.9412 ± 0.0946	0.9926 ± 0.0286
452	3153	Carbon	^{10}Be	0.7271 ± 0.0010	0.9650 ± 0.0078	0.9934 ± 0.0023
450	3404	Carbon	^{9}Be	0.7044 ± 0.0091	0.8041 ± 0.0301	0.8875 ± 0.0091
452	3404	Carbon	^{9}Be	0.7676 ± 0.0018	0.9749 ± 0.0176	0.9931 ± 0.0049
451	3404	Polyethylene	^{9}Be	0.6978 ± 0.0014	0.8236 ± 0.0194	0.9281 ± 0.0067
426	4402	Carbon	^{12}Be	0.6415 ± 0.0130	0.9787 ± 0.0443	0.9966 ± 0.0183
427	4402	Polyethylene	^{12}Be	0.5934 ± 0.0108	0.9794 ± 0.0324	0.9950 ± 0.0154
426	4679	Carbon	^{11}Be	0.6591 ± 0.0043	0.9744 ± 0.0185	0.9943 ± 0.0067
427	4679	Polyethylene	^{11}Be	0.6451 ± 0.0047	0.9763 ± 0.0137	0.9942 ± 0.0058
390	4751	Carbon	^{12}Be	0.7390 ± 0.0078	0.9853 ± 0.0126	0.9984 ± 0.0030
386	4751	Polyethylene	^{12}Be	0.7191 ± 0.0012	0.9851 ± 0.0132	0.9983 ± 0.0034
426	4987	Carbon	^{10}Be	0.7233 ± 0.0034	0.9773 ± 0.0212	0.9936 ± 0.0075
427	4987	Polyethylene	^{10}Be	0.6584 ± 0.0221	0.9791 ± 0.0152	0.9941 ± 0.0066
390	5043	Carbon	^{11}Be	0.6917 ± 0.0035	0.9827 ± 0.0126	0.9983 ± 0.0017
386	5043	Polyethylene	^{11}Be	0.7100 ± 0.0007	0.9880 ± 0.0112	0.9984 ± 0.0019
390	5366	Carbon	^{10}Be	0.6550 ± 0.0228	0.9784 ± 0.0332	0.9984 ± 0.0045
386	5366	Polyethylene	^{10}Be	0.6285 ± 0.0093	0.9923 ± 0.0309	0.9984 ± 0.0053

Table D.1: Efficiency values for beryllium beams.

Run	Energy (MeV)	Target	Beam	Efficiency for fragment charge			
				2	3	4	5
500	2910	Carbon	^{10}B	0.4518 ± 0.0518	0.1209 ± 0.0210	0.5314 ± 0.0682	0.9986 ± 0.0102
497	2910	Polyethylene	^{10}B	0.4477 ± 0.0832	0.1254 ± 0.0123	0.5576 ± 0.0402	0.9982 ± 0.0067
499	2910	Polyethylene	^{10}B	0.4112 ± 0.0400	0.0833 ± 0.0109	0.5508 ± 0.0425	0.9980 ± 0.0073
500	3420	Carbon	^{8}B	0.6476 ± 0.0798	0.4138 ± 0.1420	0.8182 ± 0.0950	1.0000 ± 0.0293
497	3420	Polyethylene	^{8}B	0.6878 ± 0.0470	0.4867 ± 0.0800	0.9388 ± 0.0787	0.9988 ± 0.0174
499	3420	Polyethylene	^{8}B	0.7269 ± 0.0342	0.6341 ± 0.1124	0.9010 ± 0.0765	0.9992 ± 0.0194
450	4324	Carbon	^{11}B	0.5483 ± 0.0041	0.4764 ± 0.0096	0.8098 ± 0.0161	0.9001 ± 0.0039
452	4324	Carbon	^{11}B	0.5280 ± 0.0256	0.8918 ± 0.0303	0.9876 ± 0.0272	0.9966 ± 0.0079
451	4324	Polyethylene	^{11}B	0.6005 ± 0.0036	0.5001 ± 0.0066	0.8696 ± 0.0110	0.9356 ± 0.0028
450	4616	Carbon	^{10}B	0.5561 ± 0.0119	0.5634 ± 0.0251	0.7181 ± 0.0358	0.9012 ± 0.0078
451	4616	Polyethylene	^{10}B	0.6059 ± 0.0260	0.6424 ± 0.0185	0.7677 ± 0.0246	0.9325 ± 0.0058
426	5502	Carbon	^{15}B	0.3701 ± 0.0102	0.6932 ± 0.0567	0.9959 ± 0.0641	0.9962 ± 0.0241
427	5502	Polyethylene	^{15}B	0.3968 ± 0.0184	0.7253 ± 0.0426	0.9906 ± 0.0430	0.9975 ± 0.0196
426	5777	Carbon	^{14}B	0.5495 ± 0.0072	0.7973 ± 0.0158	0.9912 ± 0.0170	0.9972 ± 0.0058
427	5777	Polyethylene	^{14}B	0.4749 ± 0.0157	0.8063 ± 0.0121	0.9915 ± 0.0122	0.9974 ± 0.0050
390	5938	Carbon	^{15}B	0.5097 ± 0.0258	0.8187 ± 0.0392	0.9832 ± 0.0236	0.9988 ± 0.0054
386	5938	Polyethylene	^{15}B	0.5007 ± 0.0101	0.8155 ± 0.0331	0.9888 ± 0.0241	0.9988 ± 0.0058
426	6075	Carbon	^{13}B	0.6144 ± 0.0039	0.8688 ± 0.0070	0.9900 ± 0.0073	0.9975 ± 0.0025
427	6075	Polyethylene	^{13}B	0.5908 ± 0.0156	0.8740 ± 0.0053	0.9915 ± 0.0052	0.9976 ± 0.0021
390	6228	Carbon	^{14}B	0.5028 ± 0.0180	0.8558 ± 0.0200	0.9904 ± 0.0181	0.9991 ± 0.0026
386	6228	Polyethylene	^{14}B	0.5087 ± 0.0079	0.8736 ± 0.0173	0.9907 ± 0.0151	0.9988 ± 0.0029
426	6400	Carbon	^{12}B	0.4433 ± 0.0359	0.8884 ± 0.0849	0.9873 ± 0.0910	0.9962 ± 0.0290
427	6400	Polyethylene	^{12}B	0.4300 ± 0.0671	0.9236 ± 0.0641	0.9933 ± 0.0665	0.9972 ± 0.0250
390	6541	Carbon	^{13}B	0.5451 ± 0.0055	0.9060 ± 0.0209	0.9933 ± 0.0182	0.9991 ± 0.0027
386	6541	Polyethylene	^{13}B	0.5543 ± 0.0013	0.9107 ± 0.0184	0.9910 ± 0.0165	0.9989 ± 0.0030

Table D.2: Efficiency values for boron beams.

E Breakup cross sections on proton target

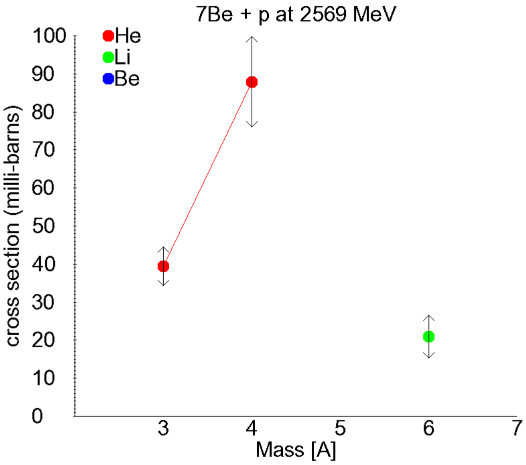

Figure E.1: Cross sections for reaction fragments of ^{7}Be+p at 2569 MeV.

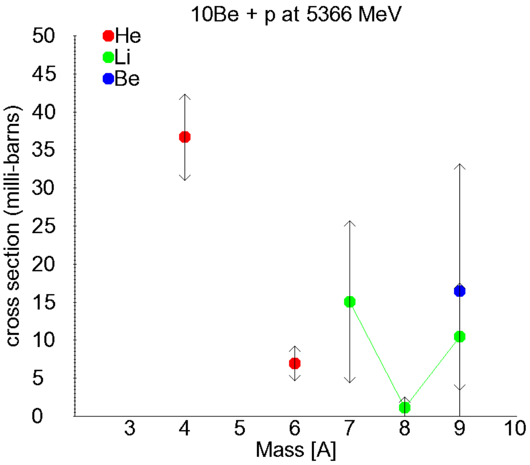

Figure E.3: Cross sections for reaction fragments of ^{10}Be+p at 5366 MeV.

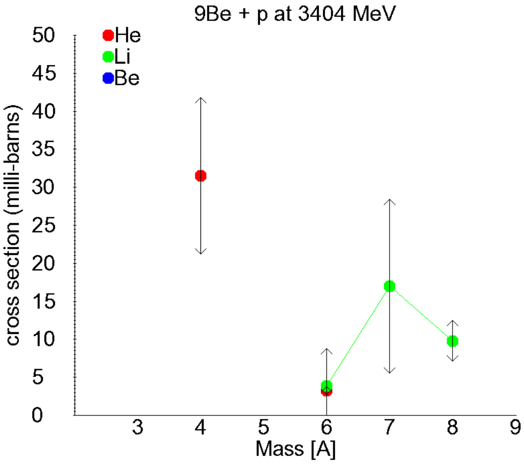

Figure E.2: Cross sections for reaction fragments of ^{9}Be+p at 3404 MeV.

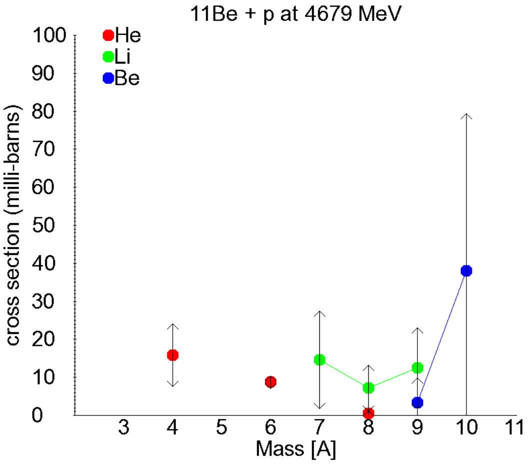

Figure E.4: Cross sections for reaction fragments of ^{11}Be+p at 4679 MeV.

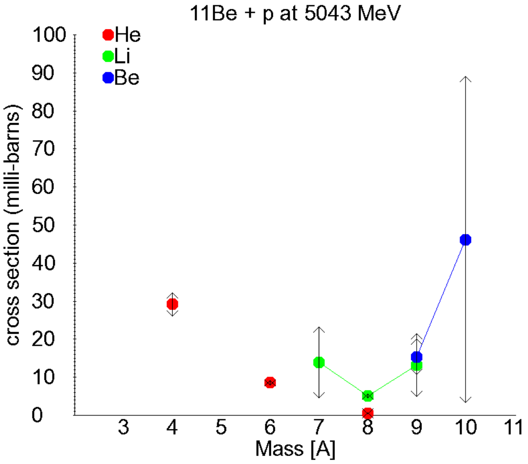

Figure E.5: Cross sections for reaction fragments of ^{11}Be+p *at 5043 MeV.*

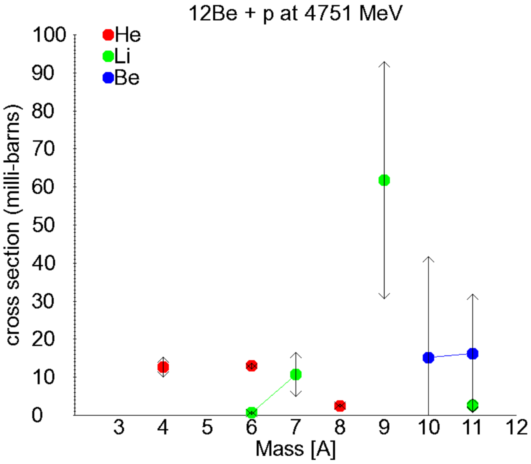

Figure E.7: Cross sections for reaction fragments of ^{12}Be+p *at 4751 MeV.*

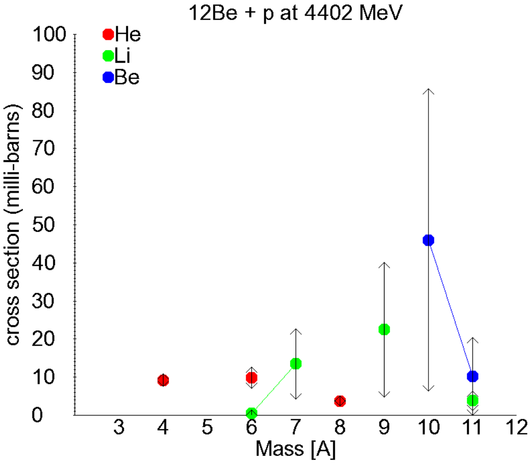

Figure E.6: Cross sections for reaction fragments of ^{12}Be+p *at 4402 MeV.*

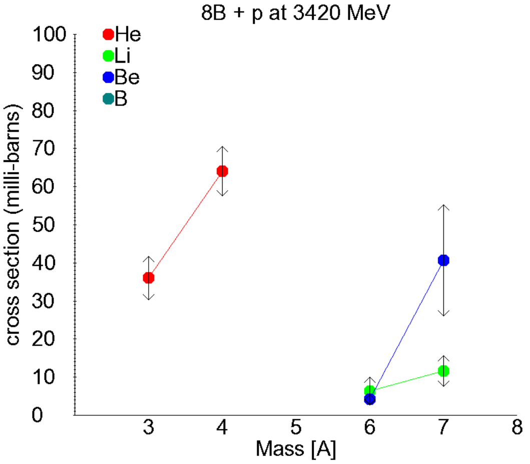

Figure E.8: Cross sections for reaction fragments of ^{8}B+p *at 3420 MeV.*

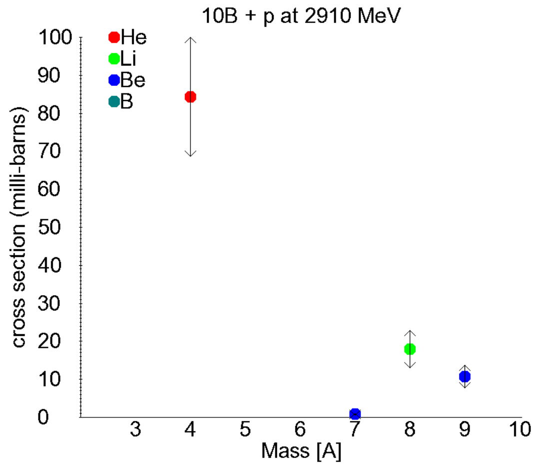

Figure E.9: Cross sections for reaction fragments of ^{10}B+*p at 2910 MeV.*

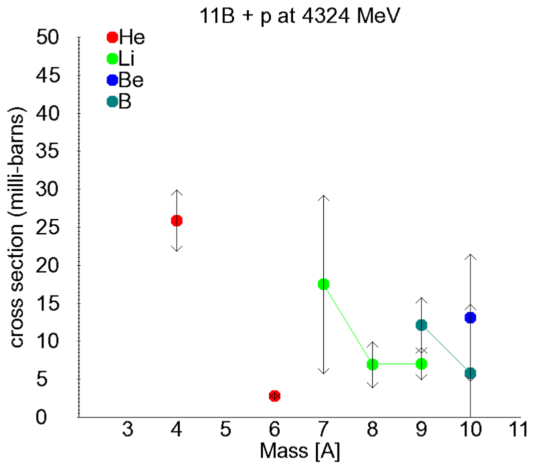

Figure E.11: Cross sections for reaction fragments of ^{11}B+*p at 4324 MeV.*

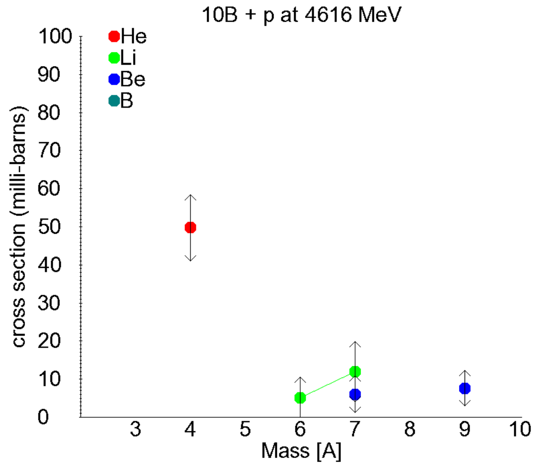

Figure E.10: Cross sections for reaction fragments of ^{10}B+*p at 4616 MeV.*

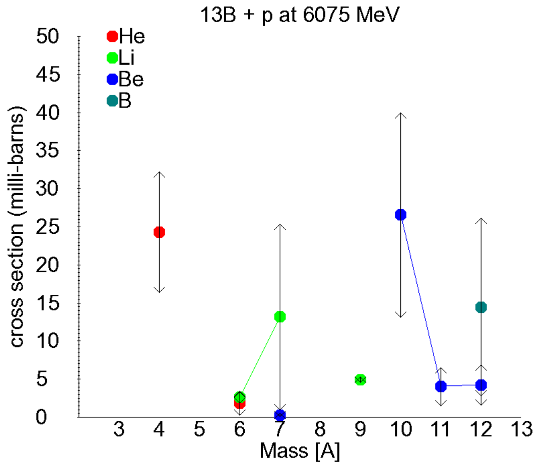

Figure E.12: Cross sections for reaction fragments of ^{13}B+*p at 6075 MeV.*

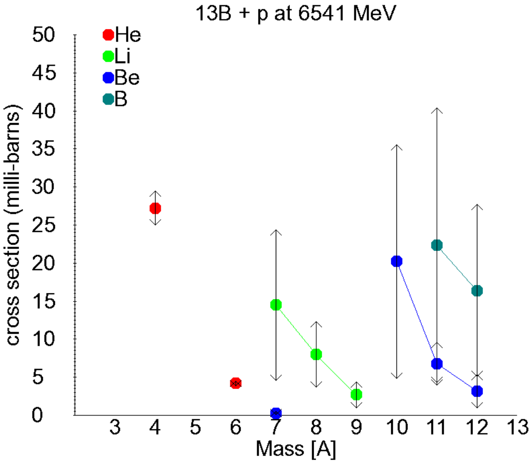

Figure E.13: Cross sections for reaction fragments of ^{13}B+*p at 6541 MeV.*

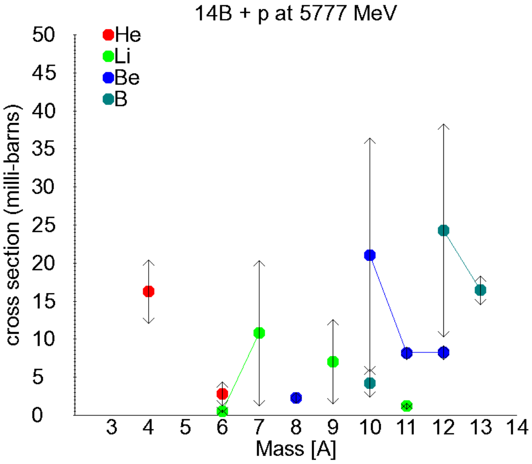

Figure E.14: Cross sections for reaction fragments of ^{14}B+*p at 5777 MeV.*

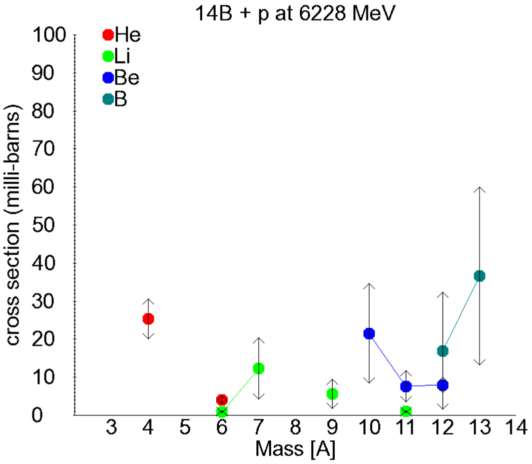

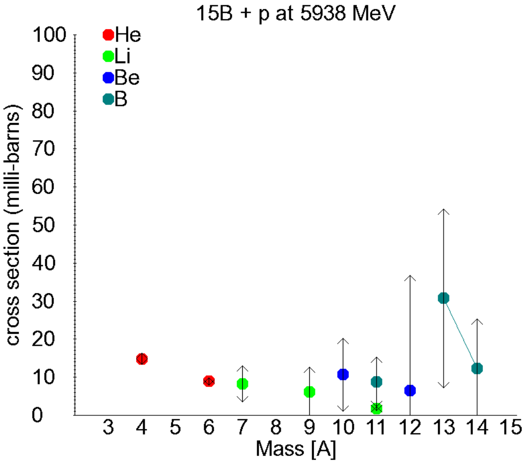

Figure E.15: Cross sections for reaction fragments of ^{14}B+*p at 6228 MeV.*

Figure E.17: Cross sections for reaction fragments of ^{15}B+*p at 5938 MeV.*

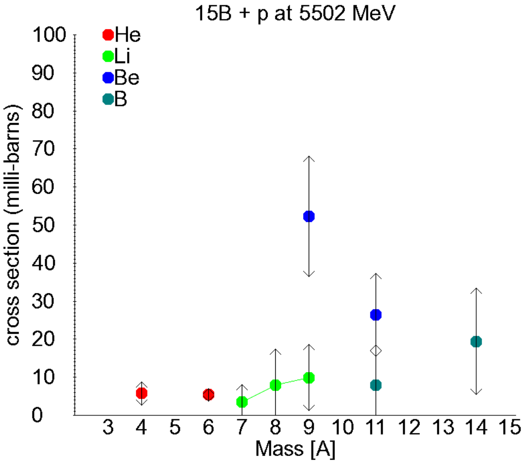

Figure E.16: Cross sections for reaction fragments of ^{15}B+*p at 5502 MeV.*

F Data tables for breakup cross sections on proton target

Fragment	Cross Section (milli-barns)
^{4}He	26.50 ± 11.21
^{6}He	6.91 ± 3.35
^{7}Li	16.84 ± 12.81
^{8}Li	4.21 ± 3.25
^{9}Li	14.82 ± 7.66
^{9}Be	21.71 ± 13.93
Total	90.99 ± 23.75

Table F.1: Cross sections for reaction fragments of ^{10}Be+p *at 4987 MeV.*

Fragment	Cross Section (milli-barns)
^{4}He	36.70 ± 5.67
^{6}He	6.93 ± 2.30
^{7}Li	15.05 ± 10.69
^{8}Li	1.14 ± 1.44
^{9}Li	10.45 ± 7.03
^{9}Be	16.42 ± 16.78
Total	86.68 ± 22.02

Table F.2: Cross sections for reaction fragments of ^{10}Be+p *at 5366 MeV.*

Fragment	Cross Section (milli-barns)
^{4}He	15.84 ± 8.32
^{6}He	8.73 ± 1.70
^{8}He	0.50 ± 0.66
^{7}Li	14.59 ± 12.91
^{8}Li	7.19 ± 6.06
^{9}Li	12.42 ± 10.65
^{9}Be	3.36 ± 6.44
^{10}Be	38.08 ± 41.26
Total	100.72 ± 46.19

Table F.3: Cross sections for reaction fragments of ^{11}Be+p *at 4679 MeV.*

Fragment	Cross Section (milli-barns)
^{4}He	29.19 ± 3.10
^{6}He	8.54 ± 0.59
^{8}He	0.58 ± 0.20
^{7}Li	13.87 ± 9.37
^{8}Li	5.10 ± 0.56
^{9}Li	13.22 ± 8.25
^{9}Be	15.39 ± 4.62
^{10}Be	46.19 ± 42.89
Total	132.08 ± 45.03

Table F.4: Cross sections for reaction fragments of ^{11}Be+p *at 5043 MeV.*

Fragment	Cross Section (milli-barns)
^{4}He	9.20 ± 1.71
^{6}He	9.85 ± 2.81
^{8}He	3.76 ± 1.29
^{6}Li	0.59 ± 0.86
^{7}Li	13.50 ± 9.30
^{9}Li	22.45 ± 17.65
^{11}Li	3.81 ± 2.54
^{10}Be	46.03 ± 39.77
^{11}Be	10.22 ± 10.21
Total	119.40 ± 45.86

Table F.5: Cross sections for reaction fragments of ^{12}Be+p *at 4402 MeV.*

Fragment	Cross Section (milli-barns)
^{4}He	12.67 ± 2.65
^{6}He	12.95 ± 0.83
^{8}He	2.55 ± 0.36
^{6}Li	0.64 ± 0.42
^{7}Li	10.71 ± 5.76
^{9}Li	61.77 ± 31.16
^{11}Li	2.60 ± 1.77
^{10}Be	15.09 ± 26.72
^{11}Be	16.28 ± 15.52
Total	135.26 ± 44.39

Table F.6: Cross sections for reaction fragments of ^{12}Be+p *at 4751 MeV.*

Fragment	Cross Section (milli-barns)
^{3}He	39.39 ± 5.10
^{4}He	87.91 ± 11.92
^{6}Li	21.02 ± 5.65
Total	148.32 ± 14.14

Table F.7: Cross sections for reaction fragments of ^{7}Be+p *at 2569 MeV.*

Fragment	Cross Section (milli-barns)
^{4}He	31.49 ± 10.28
^{6}He	3.27 ± 0.50
^{6}Li	3.84 ± 5.01
^{7}Li	16.98 ± 11.47
^{8}Li	9.81 ± 2.67
Total	65.39 ± 16.42

Table F.8: Cross sections for reaction fragments of ^{9}Be+p *at 3404 MeV.*

Fragment	Cross Section (milli-barns)
^{4}He	84.28 ± 15.66
^{8}Li	18.01 ± 4.93
^{7}Be	0.79 ± 0.18
^{9}Be	10.72 ± 3.00
Total	113.80 ± 16.69

Table F.9: Cross sections for reaction fragments of ^{10}B+p *at 2910 MeV.*

Fragment	Cross Section (milli-barns)
^{4}He	49.80 ± 8.73
^{6}Li	5.06 ± 5.47
^{7}Li	12.00 ± 7.97
^{7}Be	6.07 ± 4.87
^{9}Be	7.63 ± 4.70
Total	80.56 ± 14.68

Table F.10: Cross sections for reaction fragments of ^{10}B+p *at 4616 MeV.*

Fragment	Cross Section (milli-barns)
^{4}He	25.86 ± 4.03
^{6}He	2.83 ± 0.46
^{7}Li	17.50 ± 11.76
^{8}Li	6.92 ± 3.05
^{9}Li	7.03 ± 2.11
^{10}Be	13.14 ± 8.38
^{9}B	12.11 ± 3.63
^{10}B	5.84 ± 9.03
Total	91.23 ± 18.26

Table F.11: Cross sections for reaction fragments of $^{11}\mathrm{B}+p$ *at 4324 MeV.*

Fragment	Cross Section (milli-barns)
^{4}He	24.12 ± 15.19
^{6}Li	3.66 ± 3.37
^{7}Li	13.77 ± 13.01
^{8}Li	5.69 ± 4.07
^{9}Be	4.61 ± 5.55
^{10}Be	15.14 ± 14.42
^{11}Be	7.60 ± 2.34
^{10}B	6.77 ± 6.81
^{11}B	15.28 ± 20.24
Total	96.64 ± 33.59

Table F.12: Cross sections for reaction fragments of $^{12}\mathrm{B}+p$ *at 6400 MeV.*

Fragment	Cross Section (milli-barns)
^{4}He	24.29 ± 7.94
^{6}He	1.81 ± 1.56
^{6}Li	2.64 ± 0.79
^{7}Li	13.17 ± 12.16
^{9}Li	4.95 ± 0.36
^{7}Be	0.31 ± 0.22
^{10}Be	26.58 ± 13.43
^{11}Be	4.02 ± 2.48
^{12}Be	4.23 ± 2.65
^{12}B	14.45 ± 11.65
Total	96.44 ± 23.31

Table F.13: Cross sections for reaction fragments of $^{13}\mathrm{B}+p$ *at 6075 MeV.*

Fragment	Cross Section (milli-barns)
^{4}He	27.23 ± 2.27
^{6}He	4.20 ± 0.31
^{7}Li	14.48 ± 9.88
^{8}Li	7.99 ± 4.34
^{9}Li	2.69 ± 1.74
^{7}Be	0.31 ± 0.23
^{10}Be	20.21 ± 15.39
^{11}Be	6.79 ± 2.79
^{12}Be	3.16 ± 2.21
^{11}B	22.38 ± 18.02
^{12}B	16.41 ± 11.32
Total	125.84 ± 28.76

Table F.14: Cross sections for reaction fragments of ^{13}B+p *at 6541 MeV.*

Fragment	Cross Section (milli-barns)
^{4}He	16.25 ± 4.18
^{6}He	2.79 ± 1.57
^{6}Li	0.55 ± 0.17
^{7}Li	10.80 ± 9.53
^{9}Li	7.02 ± 5.53
^{11}Li	1.19 ± 0.36
^{8}Be	2.29 ± 0.69
^{10}Be	21.08 ± 15.32
^{11}Be	8.15 ± 0.85
^{12}Be	8.24 ± 0.95
^{10}B	4.24 ± 1.83
^{12}B	24.31 ± 14.00
^{13}B	16.44 ± 1.91
Total	123.34 ± 24.11

Table F.15: Cross sections for reaction fragments of ^{14}B+p *at 5777 MeV.*

Fragment	Cross Section (milli-barns)
^{4}He	25.38 ± 5.34
^{6}He	4.06 ± 1.03
^{6}Li	0.94 ± 0.28
^{7}Li	12.35 ± 8.14
^{9}Li	5.66 ± 3.85
^{11}Li	0.98 ± 0.30
^{10}Be	21.54 ± 13.07
^{11}Be	7.61 ± 4.10
^{12}Be	7.94 ± 2.03
^{12}B	16.97 ± 15.42
^{13}B	36.58 ± 23.39
Total	140.01 ± 32.98

Table F.16: Cross sections for reaction fragments of $^{14}\mathrm{B}+p$ *at 6228 MeV.*

Fragment	Cross Section (milli-barns)
^{4}He	5.75 ± 3.05
^{6}He	5.41 ± 1.71
^{7}Li	3.55 ± 4.49
^{8}Li	7.89 ± 9.62
^{9}Li	9.94 ± 8.73
^{9}Be	52.32 ± 15.87
^{11}Be	26.43 ± 10.96
^{11}B	7.97 ± 10.52
^{14}B	19.40 ± 14.00
Total	138.67 ± 29.66

Table F.17: Cross sections for reaction fragments of $^{15}\mathrm{B}+p$ *at 5502 MeV.*

Fragment	Cross Section (milli-barns)
^{4}He	14.87 ± 1.42
^{6}He	8.90 ± 1.02
^{7}Li	8.29 ± 4.72
^{9}Li	6.25 ± 6.39
^{11}Li	1.82 ± 0.55
^{10}Be	10.65 ± 9.61
^{12}Be	6.54 ± 30.26
^{11}B	8.78 ± 6.48
^{13}B	30.73 ± 23.48
^{14}B	12.26 ± 13.06
Total	109.10 ± 42.88

Table F.18: Cross sections for reaction fragments of ^{15}B+p *at 5938 MeV.*

Fragment	Cross Section (milli-barns)
^{3}He	36.01 ± 5.71
^{4}He	64.09 ± 6.47
^{6}Li	6.39 ± 3.71
^{7}Li	11.62 ± 3.98
^{6}Be	4.16 ± 1.30
^{7}Be	40.70 ± 14.64
Total	162.97 ± 17.89

Table F.19: Cross sections for reaction fragments of ^{8}B+p *at 3420 MeV.*

G Breakup cross sections on ^{12}C target

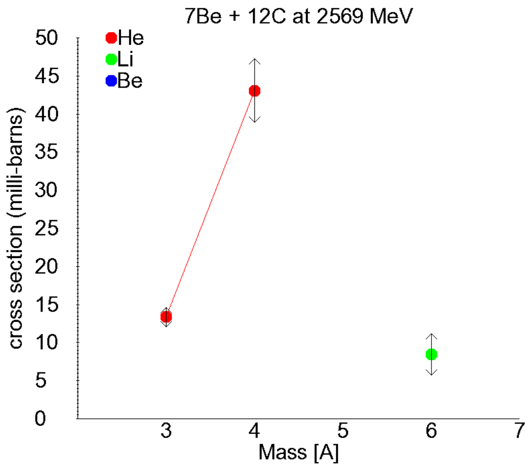

Figure G.1: Cross sections for reaction fragments of ^{7}Be+^{12}C *at 2569 MeV.*

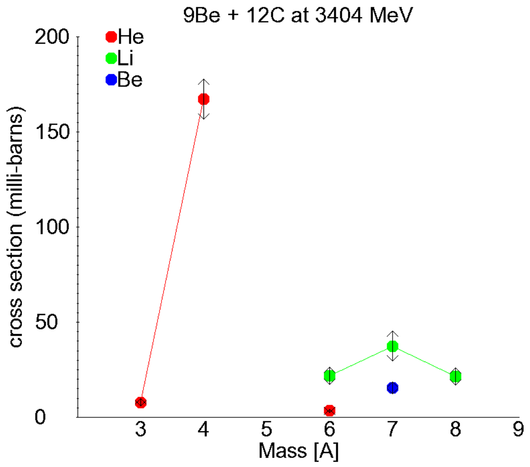

Figure G.2: Cross sections for reaction fragments of ^{9}Be+^{12}C *at 3404 MeV.*

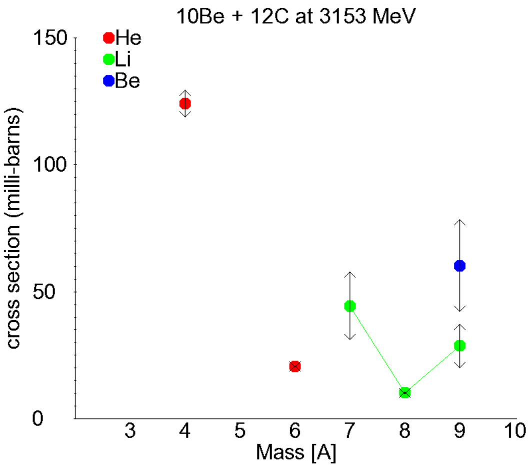

Figure G.3: Cross sections for reaction fragments of ^{10}Be+^{12}C *at 3153 MeV.*

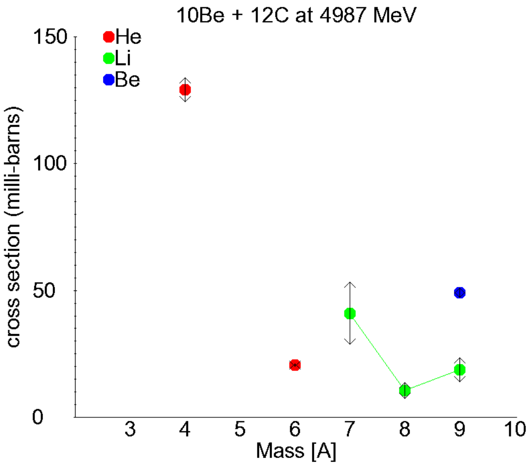

Figure G.4: Cross sections for reaction fragments of ^{10}Be+^{12}C *at 4987 MeV.*

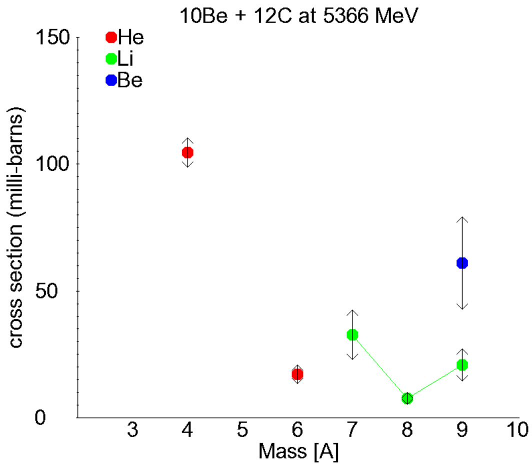

Figure G.5: Cross sections for reaction fragments of ^{10}Be+^{12}C *at 5366 MeV.*

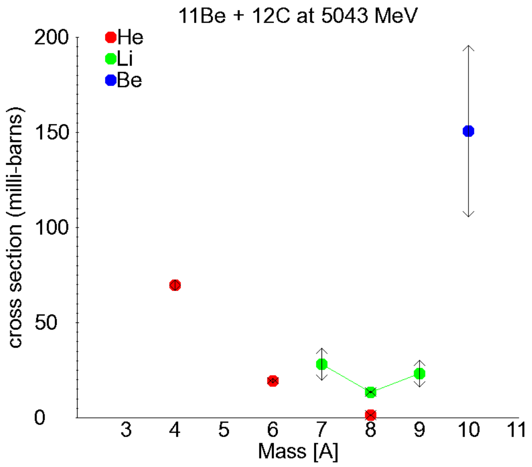

Figure G.7: Cross sections for reaction fragments of ^{11}Be+^{12}C *at 5043 MeV.*

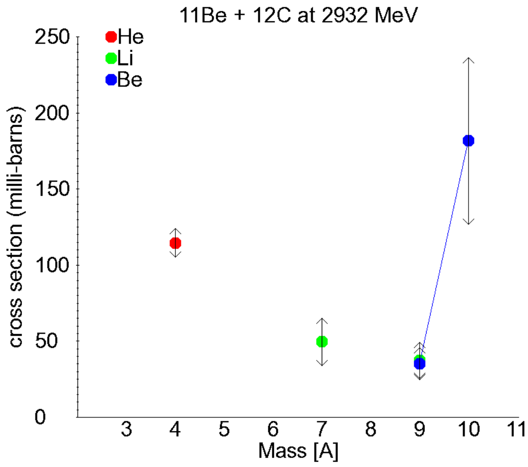

Figure G.6: Cross sections for reaction fragments of ^{11}Be+^{12}C *at 2932 MeV.*

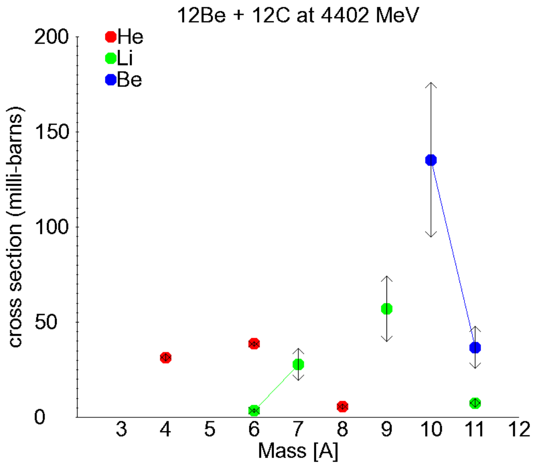

Figure G.8: Cross sections for reaction fragments of ^{12}Be+^{12}C *at 4402 MeV.*

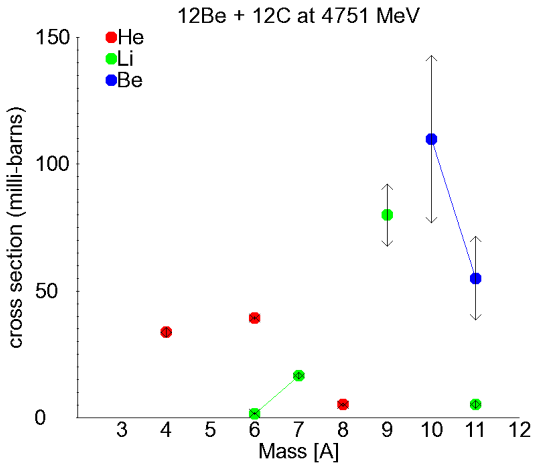

Figure G.9: Cross sections for reaction fragments of ^{12}Be+^{12}C *at 4751 MeV.*

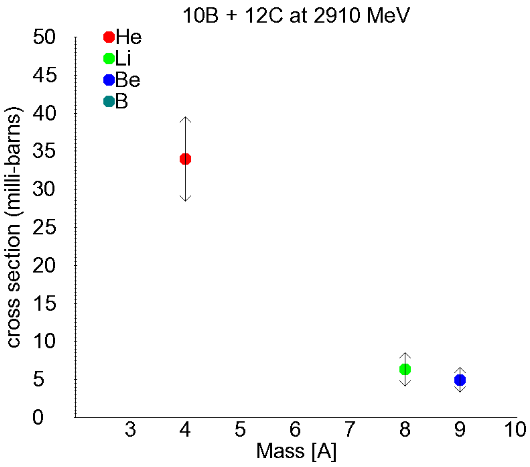

Figure G.11: Cross sections for reaction fragments of ^{10}B+^{12}C *at 2910 MeV.*

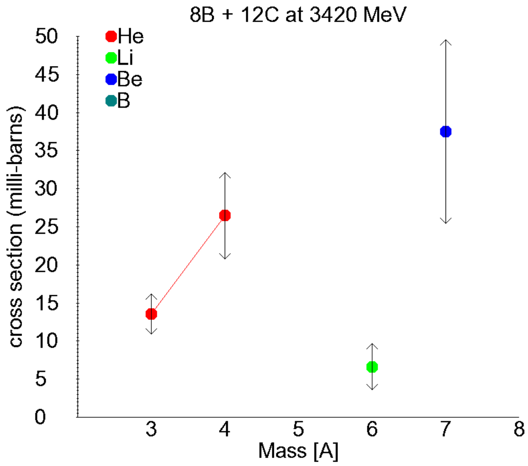

Figure G.10: Cross sections for reaction fragments of ^{8}B+^{12}C *at 3420 MeV.*

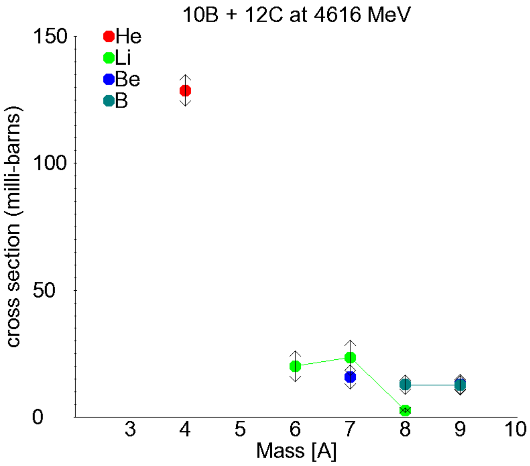

Figure G.12: Cross sections for reaction fragments of ^{10}B+^{12}C *at 4616 MeV.*

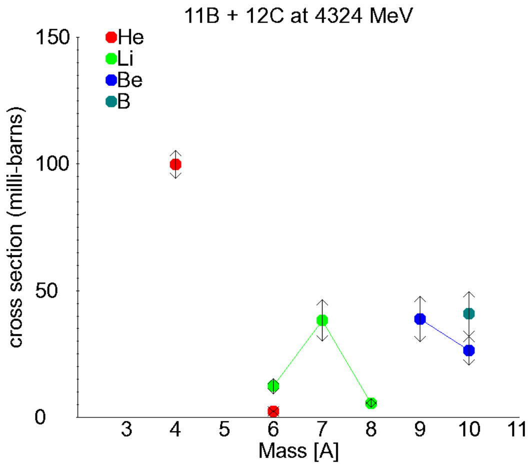

Figure G.13: Cross sections for reaction fragments of ^{11}B+^{12}C *at 4324 MeV.*

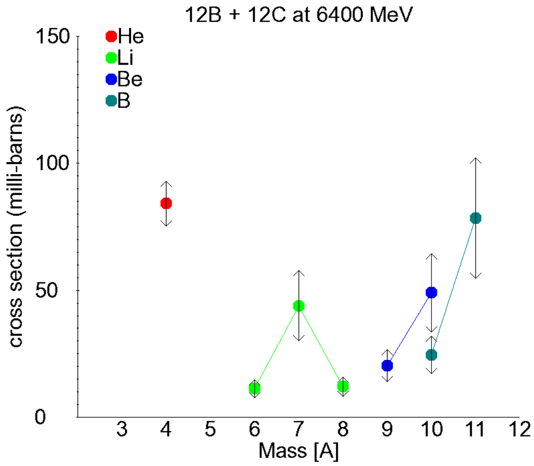

Figure G.14: Cross sections for reaction fragments of ^{12}B+^{12}C *at 6400 MeV.*

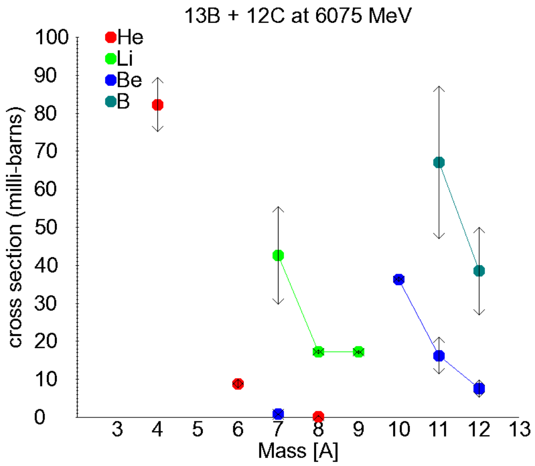

Figure G.15: Cross sections for reaction fragments of ^{13}B+^{12}C *at 6075 MeV.*

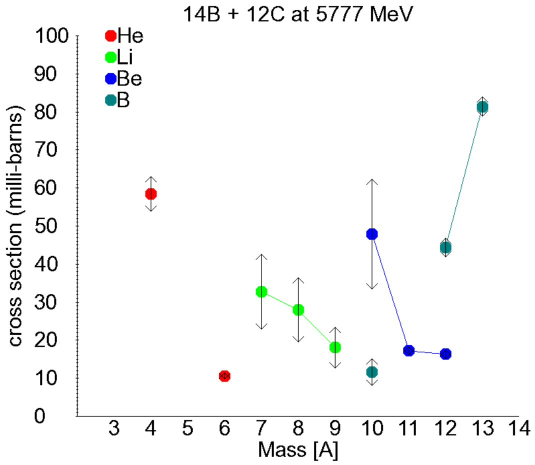

Figure G.16: Cross sections for reaction fragments of ^{14}B+^{12}C *at 5777 MeV.*

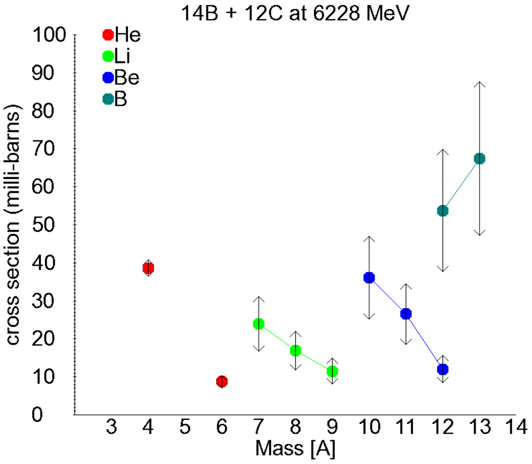

Figure G.17: Cross sections for reaction fragments of ^{14}B+^{12}C *at 6228 MeV.*

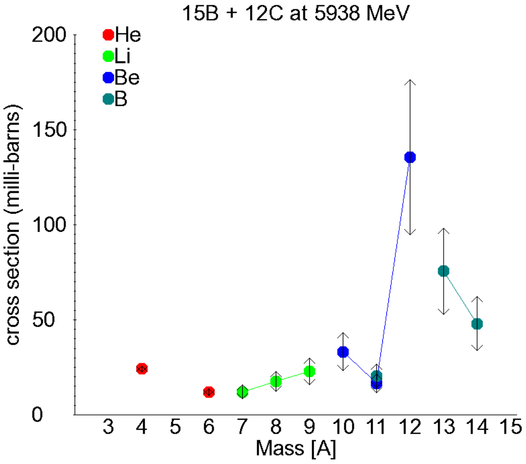

Figure G.19: Cross sections for reaction fragments of ^{15}B+^{12}C *at 5938 MeV.*

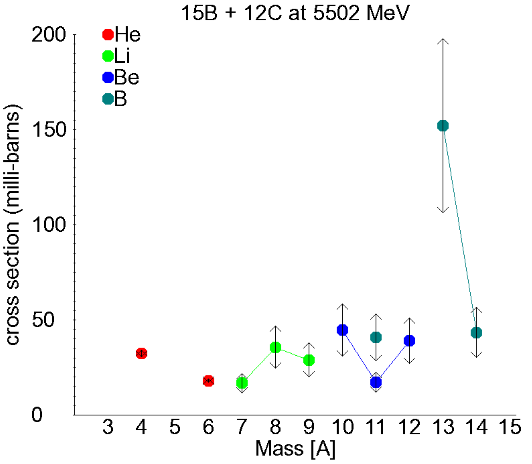

Figure G.18: Cross sections for reaction fragments of ^{15}B+^{12}C *at 5502 MeV.*

H Data tables for breakup cross sections on ^{12}C target

Fragment	Cross Section (milli-barns)
^{4}He	124.11 ± 5.18
^{6}He	20.57 ± 0.17
^{7}Li	44.39 ± 13.32
^{8}Li	10.18 ± 0.46
^{9}Li	28.68 ± 8.61
^{9}Be	60.33 ± 18.10
Total	288.26 ± 24.62

Table H.1: Cross sections for reaction fragments of ^{10}Be+^{12}C *at 3153 MeV.*

Fragment	Cross Section (milli-barns)
^{4}He	129.05 ± 4.78
^{6}He	20.70 ± 0.54
^{7}Li	41.03 ± 12.34
^{8}Li	10.48 ± 3.15
^{9}Li	18.71 ± 4.85
^{9}Be	49.18 ± 1.85
Total	269.15 ± 14.57

Table H.2: Cross sections for reaction fragments of ^{10}Be+^{12}C *at 4987 MeV.*

Fragment	Cross Section (milli-barns)
^{4}He	104.61 ± 5.79
^{6}He	17.11 ± 3.71
^{7}Li	32.74 ± 9.88
^{8}Li	7.71 ± 2.33
^{9}Li	20.82 ± 6.29
^{9}Be	60.95 ± 18.29
Total	243.93 ± 22.90

Table H.3: Cross sections for reaction fragments of ^{10}Be+^{12}C *at 5366 MeV.*

Fragment	Cross Section (milli-barns)
^{4}He	114.64 ± 9.36
^{7}Li	49.63 ± 15.72
^{9}Li	37.51 ± 11.88
^{9}Be	35.02 ± 10.57
^{10}Be	181.66 ± 54.82
Total	418.45 ± 59.94

Table H.4: Cross sections for reaction fragments of ^{11}Be+^{12}C *at 2932 MeV.*

Fragment	Cross Section (milli-barns)
^{4}He	105.49 ± 9.76
^{6}He	26.49 ± 2.60
^{8}He	1.45 ± 0.68
^{7}Li	44.42 ± 13.35
^{8}Li	20.44 ± 6.14
^{9}Li	36.16 ± 10.87
^{9}Be	26.82 ± 8.05
^{10}Be	152.62 ± 45.80
Total	413.87 ± 50.98

Table H.5: Cross sections for reaction fragments of ^{11}Be+^{12}C *at 4679 MeV.*

Fragment	Cross Section (milli-barns)
^{4}He	69.82 ± 2.75
^{6}He	19.52 ± 1.14
^{8}He	1.31 ± 0.38
^{7}Li	28.04 ± 8.42
^{8}Li	13.52 ± 0.53
^{9}Li	23.32 ± 7.00
^{10}Be	150.66 ± 45.20
Total	306.20 ± 46.61

Table H.6: Cross sections for reaction fragments of ^{11}Be+^{12}C *at 5043 MeV.*

Fragment	Cross Section (milli-barns)
^{4}He	31.46 ± 2.06
^{6}He	38.60 ± 1.13
^{8}He	5.62 ± 1.49
^{6}Li	3.40 ± 1.03
^{7}Li	27.85 ± 8.45
^{9}Li	57.01 ± 17.31
^{11}Li	7.45 ± 2.26
^{10}Be	135.34 ± 40.70
^{11}Be	36.73 ± 11.04
Total	343.47 ± 46.51

Table H.7: Cross sections for reaction fragments of ^{12}Be+^{12}C *at 4402 MeV.*

Fragment	Cross Section (milli-barns)
^{4}He	33.68 ± 1.96
^{6}He	39.32 ± 0.50
^{8}He	5.23 ± 0.70
^{6}Li	1.71 ± 0.51
^{7}Li	16.69 ± 1.27
^{9}Li	79.93 ± 12.27
^{11}Li	5.33 ± 1.60
^{10}Be	109.94 ± 32.98
^{11}Be	55.04 ± 16.51
Total	346.87 ± 38.99

Table H.8: Cross sections for reaction fragments of ^{12}Be+^{12}C *at 4751 MeV.*

Fragment	Cross Section (milli-barns)
^{3}He	13.35 ± 1.30
^{4}He	43.06 ± 4.17
^{6}Li	8.45 ± 2.73
Total	64.86 ± 5.15

Table H.9: Cross sections for reaction fragments of ^{7}Be+^{12}C *at 2569 MeV.*

Fragment	Cross Section (milli-barns)
^{3}He	7.79 ± 1.91
^{4}He	167.22 ± 10.59
^{6}He	3.36 ± 0.89
^{6}Li	21.76 ± 4.66
^{7}Li	37.46 ± 7.99
^{8}Li	21.52 ± 4.60
^{7}Be	15.51 ± 3.30
Total	274.62 ± 15.30

Table H.10: Cross sections for reaction fragments of ^{9}Be+^{12}C *at 3404 MeV.*

Fragment	Cross Section (milli-barns)
^{4}He	33.96 ± 5.55
^{8}Li	6.31 ± 2.19
^{9}Be	4.96 ± 1.62
Total	45.23 ± 6.18

Table H.11: Cross sections for reaction fragments of ^{10}B+^{12}C *at 2910 MeV.*

Fragment	Cross Section (milli-barns)
^{4}He	128.73 ± 6.09
^{6}Li	20.06 ± 6.09
^{7}Li	23.40 ± 7.10
^{8}Li	2.77 ± 0.84
^{7}Be	15.89 ± 4.83
^{9}Be	12.98 ± 3.95
^{8}B	12.90 ± 3.87
^{9}B	12.58 ± 3.78
Total	229.30 ± 13.90

Table H.12: Cross sections for reaction fragments of ^{10}B+^{12}C *at 4616 MeV.*

Fragment	Cross Section (milli-barns)
^{4}He	99.84 ± 5.56
^{6}He	2.45 ± 0.30
^{6}Li	12.31 ± 2.95
^{7}Li	38.40 ± 8.18
^{8}Li	5.66 ± 1.70
^{9}Be	38.82 ± 9.04
^{10}Be	26.31 ± 5.61
^{10}B	40.83 ± 8.82
Total	264.62 ± 17.34

Table H.13: Cross sections for reaction fragments of ^{11}B+^{12}C *at 4324 MeV.*

Fragment	Cross Section (milli-barns)
^{4}He	84.13 ± 8.81
^{6}Li	11.27 ± 3.55
^{7}Li	43.96 ± 13.86
^{8}Li	12.02 ± 3.79
^{9}Be	20.29 ± 6.37
^{10}Be	49.03 ± 15.40
^{10}B	24.46 ± 7.38
^{11}B	78.41 ± 23.66
Total	323.57 ± 34.48

Table H.14: Cross sections for reaction fragments of ^{12}B+^{12}C *at 6400 MeV.*

Fragment	Cross Section (milli-barns)
^{4}He	82.28 ± 7.17
^{6}He	8.84 ± 1.13
^{8}He	0.13 ± 0.49
^{7}Li	42.63 ± 12.79
^{8}Li	17.29 ± 0.48
^{9}Li	17.19 ± 0.48
^{7}Be	0.81 ± 0.09
^{10}Be	36.33 ± 0.64
^{11}Be	16.27 ± 4.88
^{12}Be	7.53 ± 2.26
^{11}B	67.05 ± 20.12
^{12}B	38.51 ± 11.55
Total	334.86 ± 28.01

Table H.15: Cross sections for reaction fragments of ^{13}B+^{12}C *at 6075 MeV.*

Fragment	Cross Section (milli-barns)
^{4}He	55.43 ± 2.26
^{6}He	6.57 ± 0.61
^{7}Li	29.64 ± 8.92
^{8}Li	12.69 ± 0.96
^{9}Li	10.66 ± 3.21
^{7}Be	0.71 ± 0.21
^{10}Be	49.33 ± 14.83
^{11}Be	16.23 ± 4.88
^{12}Be	6.77 ± 2.04
^{11}B	59.57 ± 17.87
^{12}B	34.35 ± 10.31
Total	281.94 ± 27.74

Table H.16: Cross sections for reaction fragments of ^{13}B+^{12}C *at 6541 MeV.*

Fragment	Cross Section (milli-barns)
^{4}He	58.49 ± 4.58
^{6}He	10.64 ± 0.78
^{7}Li	32.76 ± 9.85
^{8}Li	28.04 ± 8.43
^{9}Li	18.07 ± 5.43
^{10}Be	47.94 ± 14.41
^{11}Be	17.23 ± 0.99
^{12}Be	16.32 ± 1.14
^{10}B	11.65 ± 3.50
^{12}B	44.32 ± 2.47
^{13}B	81.37 ± 2.53
Total	366.84 ± 21.30

Table H.17: Cross sections for reaction fragments of ^{14}B+^{12}C *at 5777 MeV.*

Fragment	Cross Section (milli-barns)
^{4}He	38.64 ± 2.21
^{6}He	8.73 ± 1.64
^{7}Li	23.90 ± 7.19
^{8}Li	16.98 ± 5.11
^{9}Li	11.51 ± 3.46
^{10}Be	36.10 ± 10.85
^{11}Be	26.54 ± 7.98
^{12}Be	12.01 ± 3.61
^{12}B	53.72 ± 16.12
^{13}B	67.45 ± 20.24
Total	295.58 ± 31.00

Table H.18: Cross sections for reaction fragments of ^{14}B+^{12}C *at 6228 MeV.*

Fragment	Cross Section (milli-barns)
^{4}He	32.48 ± 1.74
^{6}He	18.10 ± 0.83
^{7}Li	16.76 ± 5.21
^{8}Li	35.61 ± 11.08
^{9}Li	28.98 ± 9.02
^{10}Be	44.71 ± 13.73
^{11}Be	17.25 ± 5.30
^{12}Be	39.13 ± 12.01
^{11}B	40.81 ± 12.29
^{13}B	152.07 ± 45.81
^{14}B	43.48 ± 13.10
Total	469.39 ± 54.92

Table H.19: Cross sections for reaction fragments of ^{15}B+^{12}C *at 5502 MeV.*

Fragment	Cross Section (milli-barns)
^{4}He	24.27 ± 1.58
^{6}He	12.05 ± 1.75
^{7}Li	12.11 ± 3.68
^{8}Li	17.55 ± 5.33
^{9}Li	22.91 ± 6.96
^{10}Be	33.22 ± 10.00
^{11}Be	16.52 ± 4.97
^{12}Be	135.50 ± 40.78
^{11}B	20.49 ± 6.15
^{13}B	75.57 ± 22.67
^{14}B	48.06 ± 14.42
Total	418.25 ± 51.42

Table H.20: Cross sections for reaction fragments of $^{15}\mathrm{B}+^{12}\mathrm{C}$ *at 5938 MeV.*

Fragment	Cross Section (milli-barns)
^{3}He	13.59 ± 2.63
^{4}He	26.49 ± 5.68
^{6}Li	6.64 ± 3.03
^{7}Be	37.51 ± 12.08
Total	84.23 ± 13.94

Table H.21: Cross sections for reaction fragments of $^{8}\mathrm{B}+^{12}\mathrm{C}$ *at 3420 MeV.*

References

[1] E. Rutherford, Phil. Mag. **21**, 669 (1911)

[2] H.Horiuchi and K. Ikeda, Prog. Theor. Phys. **40**, 277 (1968)

[3] W. Von Oertzen et al., Phy. Rep. **432**, 43 (2006)

[4] B. Buck, C. B. Dover and J. P. Vary, Phys. Rev. C **11**, 1803-1821 (1975)

[5] Y. Kanada-En'yo and H. Horiuchi, Prog. Theo. Phys. **142**, 205 (2001)

[6] W. von Oertzen, Eur. Phys. J. A **11**, 403 (2001)

[7] B. Buck et al., Phys. Rev. C **52**, 1840 (1995)

[8] L. R. Hafstad and E. Teller, Phys. Rev. **54**, 681 (1938)

[9] W. Bauhoff, H. Schultheis and R. Schultheis, Phys. Rev. C **29**, 1046 (1984)

[10] M. Freer et al., Phys. Rev. C **70**, 064311 (2004)

[11] D. M. Brink, Nucl. Phys. A **91**, 1 (1967)

[12] Y.-Z. Qian, Prog. Part. Nucl. Phys. **50**, 153 (2003)

[13] M. Freer et al., Phys. Rev. Lett. **96**, 042501 (2006)

[14] N. I. Ashwood et al., Phys. Rev. C **70**, 024608 (2004)

[15] N. I. Ashwood et al., Phys. Rev. C **70**, 064607 (2004)

[16] N. I. Ashwood et al., Phys. Lett. B **580**, 129 (2004)

[17] N. Curtis et al., to be submitted to Phys. Rev. C. (2013)

[18] B. R. Mottleson and S.G. Nilsson, Phys. Rev. **99**, 1615 (1955)

[19] P. McEwan and M. Freer, J Phys. G **30**, 447-463 (2004)

[20] T. Munoz-Britton, private communication

[21] M. Freer, Rep. Prog. Phys. **70**, 21492210 (2007)

[22] http://www.grandinetti.org/Teaching/Chem121/Lectures/MOTheory/ (accessed 16/10/2012)

[23] M. Freer and A.C. Merchant, J. Phys. G **23**, 261 (1997)

[24] M. Freer, R.R. Betts, A.H. Wousmaa, Nucl. Phys. A **587**, 36 (1995)

[25] H. Horiuchi and Y. Kanada-En'yo, Nucl. Phys. A **588**, 121 (1995)

[26] B. S. Pudliner, V.R. Pandharipande, J. Carlson, S.C. Pieper, and R.B. Wiringa, Phys. Rev. C **56**, 1720 (1997)

[27] R. B. Wiringa, S.C. Pieper, J. Carlson and V.R. Pandharipande, Phys. Rev. C **62**, 014001 (2000)

[28] G. Krein, Th.A.J. Maris, B.B. Rodrigues, E.A. Veit, Phys. Rev. C **51**, 2646 (1995)

[29] L. V. Chulkov et al., Nuc. Phys. A **759**, 4363 (2005)

[30] A. A. Cowley et al., Phys. Rev. C **44**, 329 (1991)

[31] K. S. Krane, Introductory Nuclear Physics, John Wiley & Sons (1988) Ch. 3

[32] GSI website http://www.gsi.de/forschung/kp/kp2/collaborations/R3B/QFS.html (accessed 12/10/2012)

[33] M. Leuschner et al., Phys. Rev. C **49**, 955 (1994)

[34] A. Gade and T. Glasmacher, Prog. Part. Nucl. Phys. **60**, 161 (2008)

[35] Y. Kanada-En'yo et al., Prog. Theor. Exp. Phys. **01** (2012)

[36] M. Kimura and H. Horiuchi, Nucl. Phys. A **767**, 58 (2006)

[37] GSI website http://www.gsi.de/en/research/accelerator_facility.htm (accessed 01/11/2012)

[38] N. Curtis, private communication.

[39] GSI website http://www-inj.gsi.de/index.php (accessed 25/10/2012)

[40] H. Geissel et al., Nucl. Instrum. Meth. B **70**, 286 (1992)

[41] Land02 website http://www-linux.gsi.de/~rplag/land02/ (accessed 26/10/2012)

[42] K. S. Krane, Introductory Nuclear Physics, John Wiley & Sons (1988) p. 203

[43] G. F. Knoll, Radiation Detection and Measurement, 4th Edition, John Wiley & Sons (2010) p.329

[44] G. F. Knoll, Radiation Detection and Measurement, 4th Edition, John Wiley & Sons (2010) p.32

[45] G. F. Knoll, Radiation Detection and Measurement, 4th Edition, John Wiley & Sons (2010) p.235

[46] G. F. Knoll, Radiation Detection and Measurement, 4th Edition, John Wiley & Sons (2010) p.368

[47] Land02 website http://web-docs.gsi.de/~rplag/land02/index.php?page=detectors/pos/pos (accessed 30/10/2012)

[48] J. Lilley, Nuclear Physics, John Wiley & Sons (2001) p. 130

[49] Land02 website http://web-docs.gsi.de/~rplag/land02/index.php?page=detectors/psp/psp (accessed 30/10/2012)

[50] Land02 website http://web-docs.gsi.de/~rplag/land02/index.php?page=detectors/rolu/rolu (accessed 30/10/2012)

[51] C. Caesar, private communication.

[52] V. Metag et al., The Darmstadt-Heidelberg-Crystal-Ball, Proc. Geiger Memorial Meeting, October 1982

[53] Land02 website http://web-docs.gsi.de/~rplag/land02/index.php?page=detectors/cb/CB_doc (accessed 30/10/2012)

[54] Land02 website http://web-docs.gsi.de/~rplag/land02/index.php?page=detectors/ssd/sst_dets_runs (accessed 30/10/2012)

[55] J. Cub et al., Nucl. Intrum. Meth. A **402**, 67 (1998)

[56] Land02 website http://web-docs.gsi.de/~rplag/land02/index.php?page=detectors/ntf/ntf (accessed 30/10/2012)

[57] S393 ELog https://elog.gsi.de/S393/687 (accessed 10/01/2013)

[58] Land02 website http://web-docs.gsi.de/~rplag/land02/workshop_0509/ntf.pdf (accessed 15/02/2013)

[59] Investigation of the Dipole Response of Nickel Isotopes in the Presence of a High-Frequency Electromagnetic Field by D. Rossi, Ph. D. Thesis, Johannes Gutenberg-Universität (2009)

[60] K. S. Krane, Introductory Nuclear Physics, John Wiley & Sons (1988) p. 202

[61] Land02 website http://web-docs.gsi.de/~rplag/land02/workshop_0509/land02_may09_pos_psp.pdf (accessed 15/02/2013)

[62] National Nuclear Data Center website www.nndc.bnl.gov/ (accessed 15/02/2013)

[63] Land02 website http://web-docs.gsi.de/~rplag/land02/workshop_0509/XB_overview_land2workshop.ppt (accessed 15/02/2013)

[64] LISE++ website http://lise.nscl.msu.edu/lise.html (accessed 19/02/2013)

[65] The DAQ always runs by H. T. Johansson, Tekn. Lic., Chalmers University of Technology, ISSN 1653-7521 (2006)

[66] Land02 website http://web-docs.gsi.de/~rplag/land02/index.php?howto=sw/HowTo_eta_pos_corr (accessed 21/02/2013)

[67] Ronja Theis, private communication.

[68] Land02 website http://web-docs.gsi.de/~rplag/land02/index.php?howto=sw/HowTo_XB_gainmatch_with_muons (accessed 26/02/2013)

[69] http://root.cern.ch

[70] R. Plag, GSI Helmholtzzentrum für Schwerionenforschung, Planckstraße 1, 64291 Darmstadt, Germany

[71] E. Sauvan etal., Phys. Lett. B **491**, 1 (2000)

[72] https://www.gsi.de/en/start/fair/aufbau_der_fair_beschleunigeranlage.htm (accessed 12/08/2013)

[73] http://www.liv.ac.uk/physics/news/articles/liverpool-physicists-join-worlds-premier-nuclear-physi
(accessed 15/08/2013)

[74] http://www.gsi.de/r3b (accessed 19/08/2013)

[75] N. Ashwood, private communication.

[76] Technical Report for the Design, Construction and Commissioning of The CALIFA Barrel, Project Leader: Thomas Aumann, http://igfae.usc.es/~r3b/documentos/califa_talks/CALIFA_BARREL_TDR_web.pdf (accessed 20/08/2013)

[77] J. Enders et al., Phys. Rev. C. **67**, 064301 (2003)

[78] B. Blank et al., Nucl. Phys. A **624**, 242 (1997)

[79] D. Cortina-Gil et al., Phys. Lett. B **529**, 36 (2002)

[80] D. Cortina-Gil et al., Eur. Phys. J. A **10**, 49 (2001)

[81] M. Freer, private communication.